

Carnegie Mellon University

CARNEGIE INSTITUTE OF TECHNOLOGY

THESIS

SUBMITTED IN PARTIAL FULFILLMENT OF THE REQUIREMENTS

FOR THE DEGREE OF Doctor of Philosophy

TITLE A Microfluidic Platform for the Control and Analysis
of Phase Transitions in Concentrating Droplets

PRESENTED BY Sharon Vuong

ACCEPTED BY THE DEPARTMENT OF
Chemical Engineering

SHELLEY ANNA 6/30/14
SHELLEY ANNA, ADVISOR DATE

LORENZ BIEGLER 6/30/14
LORENZ BIEGLER, DEPARTMENT HEAD DATE

APPROVED BY THE COLLEGE COUNCIL

VIJAYAKUMAR BHAGAVATULA 6/30/14
DEAN DATE

**A microfluidic platform for the control and analysis of phase transitions in
concentrating droplets**

Submitted in partial fulfillment of the requirements for

the degree of

Doctor of Philosophy

in

Chemical Engineering

Sharon M. Vuong

B.S., Chemical Engineering, Rensselaer Polytechnic Institute

Carnegie Mellon University
Pittsburgh, PA

August, 2014

Acknowledgements

The work presented in this thesis would not have been possible without the tremendous amount of support I received during my time here at Carnegie Mellon. I would first like to thank my advisor, Professor Shelley Anna, for all the guidance she has provided over the years. Her unwavering dedication and patience have helped me become a better researcher and better professional all around. I would also like to thank my thesis committee, Professors Lynn Walker (especially for being my unofficial advisor on the Dow project), Bob Tilton, and Steve Garoff, for their expertise and enthusiasm regarding various aspects of my research. Additional gratitude goes to Ben Freireich, Karl Jacob, Adam Grzesiak, and the rest of the group from the Dow Chemical Company for their insights and continuous support of this work. Funding for the research presented in this thesis was provided by the National Science Foundation Graduate Research Fellowship, the Dow Chemical Company University Partnership Initiative, and the Department of Chemical Engineering.

I would also like to thank the past and present members of the Anna group for all their help: Wingki Lee, Nick Alvarez, and Sourav Chatterjee for showing me how to fabricate microfluidic devices and for helping me get oriented in the lab; Anthony Kotula and Chris Nelson for our coffee/tea breaks, informal discussions of research, and their friendship in general; Ying Zhang, Todd Moyle, Stephanie Kirby, Blake Bleier and the rest of the Complex Fluids Engineering office for all their help and for making the office such a great place to work. I also appreciate all the help I received from Melissa Dao with the bulk rheology

experiments; Alex Hallenbeck and Steve Illes with the Raman spectrometer, with an extra thank you to Professor John Kitchin for allowing me to use it; and Jason Wolf for his help with x-ray diffraction. Additional thanks goes to Melissa Day for helping me explore Pittsburgh and for all the fun discussions that had nothing to do with research most days; and to all the friends I have made over the years as a result of my involvement with the Society of Women Engineers at CMU.

I am also very grateful for my family and friends who are scattered across the country for their constant encouragement. A special thanks goes to my parents, who have never stopped believing in me and have always encouraged me to pursue my interests. I would also like to thank my sister Jen for inspiring me and for being an awesome big sister. Additional thanks goes to Mandy Chun, Nathan Chun, Kelly Copenhaver, Corinne Disenhof, Julia Killey, and Alicia Murai for not only helping me edit this thesis, but for always making sure I stayed sane and for being the best friends a person could ask for. Finally, I would like to thank my (significantly) better half, Mike Miller, for an extensive list of reasons, but most simply put, for always being there for me.

Abstract

This work describes the development of a microfluidic platform that can be used to study suspension stability and crystallization within droplets as a function of time and concentration. Techniques for monodisperse droplet formation, droplet trapping and storage, and droplet dehydration are developed and used to design a microfluidic platform that can be adapted for the applications of interest. A geometric model is developed to predict the droplet shape and emulsion structure generated by microfluidic nozzles. However, droplet volume and structure spacing cannot be independently controlled using microfluidic nozzles, and a design consisting of an array of traps is considered to achieve the desired structure for stable, extended droplet observation. The dehydration of aqueous droplets stored in the array is characterized as a function of relative humidity, and is shown to be reasonably estimated as a species diffusing from a sphere into an infinite medium. The microfluidic platform for droplet dehydration is combined with particle tracking to show that the stability of particle suspensions can be probed as a function of salt concentration. The flocculation behavior observed in the trapped droplets agrees well with corresponding macroscale measurements as well as with previously published studies. The platform is also used to generate substantial sample sizes to measure nucleation statistics and crystal growth rates of glycine as a function of initial concentration, environmental conditions, and the presence of additives. These applications show proof of concept that the microfluidic platform is a useful tool for the analysis of the behavior observed during particle aggregation and crystallization.

Table of Contents

Acknowledgements.....	ii
Abstract.....	iv
Table of Contents.....	v
List of Tables.....	vii
List of Figures.....	viii
Chapter 1: Introduction.....	1
Chapter 2: Background.....	5
Chapter 3: Materials and Methods.....	13
3.1. Microfluidic Device Fabrication.....	13
3.2. Materials.....	17
3.3. Data Acquisition and Data Analysis.....	17
3.4. References.....	19
Chapter 4: Tuning Bubbly Structures in Microchannels.....	20
4.1. Introduction.....	20
4.2. Geometric Model for Foam Structure.....	26
4.3. Materials and Methods.....	37
4.4. Results.....	40
4.5. Discussion.....	51
4.6. Conclusions.....	58
4.7. References.....	60
Chapter 5: Controlled Dehydration of Nanoliter Droplets Stored in a Microfluidic Device.....	62
5.1. Introduction.....	62

5.2.	Materials and Methods.....	68
5.3.	Results and Discussion	75
5.4.	Conclusions.....	91
5.5.	References.....	93
Chapter 6: Microfluidic Platform for the Characterization of Concentrating Electrostatically Stabilized Nanoparticle Suspensions		96
6.1.	Introduction.....	96
6.2.	Materials and Methods.....	101
6.3.	Results.....	106
6.4.	Discussion.....	132
6.5.	Conclusions.....	136
6.6.	References.....	138
Chapter 7: Nucleation and Growth Studies in a Microfluidic Device		141
7.1.	Introduction.....	141
7.2.	Materials and Methods.....	147
7.3.	Results.....	150
7.4.	Discussion.....	169
7.5.	Conclusions.....	174
7.6.	References.....	175
Chapter 8: Conclusions and Future Work.....		178

List of Tables

Table 3.1. SU-3050 thickness as a function of spin cycle speed.	14
Table 3.2. Pixel to micron conversion factors used to determine droplet volumes.	18
Table 5.1. Initial sucrose concentrations used in the volume verification experiments given the average initial droplet volume (7.6 nL) and the desired droplet volumes: confined: 6.0 nL, transition to pancake: 5.4 nL, pancake: 3.0 nL, transition to sphere: 0.3 nL, sphere: 0.2 nL. The oil index of refraction and corresponding match concentration C_{match} of the sucrose are used to calculate the initial concentration needed to attain C_{match} at the desired volume in the five columns on the right.....	82
Table 7.1. Expected wavenumbers (cm^{-1}) of glycine peaks from Raman spectroscopy. Many peaks above 500 cm^{-1} are similar for both polymorphs and cannot be used to definitively distinguish between the two polymorphs. ^{35,36}	150
Table 7.2. Expected values of 2θ ($^\circ$) for glycine from x-ray diffraction. The major peaks (those with relative intensities above 70%) are bolded and italicized. There are a significant number of minor peaks in both of these spectra, but only a few are listed that are used to identify the polymorph from XRD spectra. ^{6,37}	150
Table 7.3. Initial and final concentrations prior to crystallization of glycine and additives for systems studied at 5-10% relative humidity. The glycine supersaturation $[\text{Gly}]_f / [\text{Gly}]_s$ is also listed, where the saturation concentration of glycine at 20°C $[\text{Gly}]_s = 2.6 \text{ M}$	152
Table 7.4. Average time and standard deviation to crystallization once a glycine droplet has reached saturation concentration; time required for the entire droplet array to crystallize at 10% relative humidity; and number of drops sampled in each array.....	156
Table 7.5. Radius of the droplet immediately prior to crystallization and the total time required for the entire drop to be crystallized at 10% relative humidity.	163
Table 7.6. Fraction of crystals out of 50 crystals sampled that had a particular type of morphology shown in Fig. 7.7. All experiments are performed with an initial glycine concentration $C_i = 1.0 \text{ M}$. Relative humidity is 5%, unless otherwise stated.....	164

List of Figures

Figure 4.1. Typical images of bubble shapes and structure qualitatively organized in terms of gas volume fraction and bubble size.....	22
Figure 4.2. Schematic diagrams of (a) top and (b) side views of a pancake bubble in a microchannel where $w > h$	22
Figure 4.3. Schematic diagrams of (a) top and (b) side views of a slug bubble in a microchannel where $w > h$	23
Figure 4.4. Schematic diagram depicting the arrangement of bubbles occupying multiple rows in a two-dimensional hexagonal close packed pattern in a microchannel of width w	33
Figure 4.5. Predicted regime map of bubble shapes and structures in a rectangular microchannel with $\Lambda = 0.2$	42
Figure 4.6. Regime map of observed and predicted dispersed phase shapes and structures in a rectangular microchannel ($\Lambda = 0.2$). Symbol fill indicates the nozzle type: filled symbols – flow-focusing, open symbols - T-junction, and x-filled symbols - co-flow. Symbol shapes indicate structure: (\diamond) dripping, (\square) slugs, (\circ) alternating foam, (Δ) packed foam, and (∇) bamboo foam.....	45
Figure 4.7. Regime map of observed and predicted dispersed phase shapes and structures in a rectangular microchannel ($\Lambda = 0.1$). Symbol fill indicates the nozzle type: filled symbols – flow-focusing, open symbols - T-junction, and x-filled symbols - co-flow. Symbol shapes indicate structure: (\diamond) dripping, (\square) slugs, (\circ) alternating foam, (Δ) packed foam, and (∇) bamboo foam.....	48
Figure 4.8. Regime map of observed and predicted dispersed phase shapes and structures in a rectangular microchannel ($\Lambda = 1$). Symbol fill indicates the nozzle type: filled symbols – flow-focusing, open symbols - T-junction, and x-filled symbols - co-flow. Symbol shapes indicate structure: (\diamond) dripping, (\square) slugs, (\circ) alternating foam, (Δ) packed foam, and (∇) bamboo foam.....	50
Figure 5.9. Schematic diagram of a microfluidic trap unit that consists of a 300 μm trap and 200 μm bypass channel. The uniform depth of the channel is $h = 100 \mu\text{m}$	64
Figure 5.10. Formation and storage of a single drop inside a trap and bypass unit. (a) The trap and bypass are filled with mineral oil. (b) A slug of the droplet phase enters the trap and bypass simultaneously. The trap fills first until it reaches the restriction, and then the rest of the slug enters the bypass. (c) The tail end of the slug reaches the junction of the trap and bypass and pinches off a droplet that is	

held stationary within the trap. The remainder of the slug repeats the process with the next trap and bypass unit. Scale bar is 100 μm65

Figure 5.11. A side view of the microfluidic trap with the oil phase represented in gray, and the PDMS channel walls with crosshatching. Water will diffuse from the droplet through the oil and PDMS, and evaporate into the air surrounding the device.67

Figure 5.12. An example section of a 10x25 microfluidic trap array. The same trap shown in Fig. 5.1 is patterned in a square array. Droplets are spaced 1.4 mm apart (center-to-center).....72

Figure 5.13. Evolution of droplet shape as droplet volume decreases with time. The aqueous phase is represented in white, the oil phase in gray, and the PDMS channel walls with crosshatching.....74

Figure 5.14. A typical image progression of the dehydration of a trapped droplet over 10 hours at 5% relative humidity. Mineral oil is used for the continuous phase fluid. Two hours have elapsed between each image from left to right. Scale bar is 100 μm76

Figure 5.15. Average droplet volume measured in three different devices at 5% relative humidity. Each filled symbol shape represents a separate device. The solid line is a fit to the spherical model Eq. (5.1). Mineral oil is used for the continuous phase fluid. Error bars indicate the standard deviation of the droplet volumes in the array.....77

Figure 5.16. Refractive index varies linearly with sucrose concentration with the relationship $n_{\text{solution}} = 0.048C_{\text{sucrose}} + n_{\text{solvent}}$, where n_{solvent} is equal to the refractive index of water, $n_w = 1.33$. The refractive indices of silicone oil ($n = 1.40$), octanol ($n = 1.43$), and mineral oil ($n = 1.46$) with 5% (w/w) Span 80 are marked by the horizontal lines. Data from Ref. 35.....80

Figure 5.17. An example of a droplet of sucrose undergoing refractive index changes as the droplet volume decreases and solute concentration increases. a) Initial trapped sucrose droplet. b) Some water has diffused out of the droplet and has achieved the concentration where $n_{\text{droplet}} = n_{\text{oil}}$. c & d) The droplet has continued to dehydrate and has reappeared. Scale bar is 100 μm81

Figure 5.18. Refractive index verification of droplet volumes in mineral oil. Predicted scaled volumes for each droplet shape or transition using equation for the volume of a slug (—), slug to pancake transition (·—), pancake (- - -), sphere to pancake transition (· · —), and sphere (····) are shown as horizontal lines.83

Figure 5.19. Scaled droplet volume versus initial concentration of sucrose for all droplet volumes in mineral oil, octanol, and silicone oil.....85

Figure 5.20. Time for 75% of the droplets sampled within an array to reach the final state (water – complete dehydration of droplet, NaCl – crystallization or constant droplet volume). All concentrations given refer to the initial concentration in the droplet.87

Figure 5.21. Final droplet volumes corresponding to the experiments shown in Fig. 5.12. The triangles represent $[\text{NaCl}]_i = 100 \text{ mM}$, which at higher humidities did not crystallize and remained at a constant final volume.89

Figure 6.22. Comparison of microrheological measurements conducted in trapped nanoliter droplets with those measured in a thin film of and predicted in the literature³⁴ for glycerol-water solutions of varying concentration.104

Figure 6.23. Time for 75% of the droplets sampled within an array to reach the final state (water – complete dehydration of droplet, NaCl – crystallization, silica – no volume change). All concentrations given refer to the initial concentration of the droplet.107

Figure 6.24. Final silica concentration as a function of relative humidity. The initial silica concentration for all experiments is $\phi_i = 0.02$109

Figure 6.25. Final silica concentration as a function of initial silica concentration and added NaCl, including cases that exhibited formation of a dark mass at higher salt concentrations. All experiments are carried out at 5-10% humidity.110

Figure 6.26. Dehydration of a trapped droplet containing a silica suspension ($2a = 22\text{nm}$, $\phi_i = 0.02$) over 10 hours. Two hours have elapsed between each image from a) to f). Scale bar is $100 \mu\text{m}$111

Figure 6.27. A "front" is observed to move radially from the outer edge of the droplet to the center in highly concentrated silica suspensions ($\phi_i = 0.02$). Approximately 20 minutes have elapsed between a) to e). Scale bar is $100 \mu\text{m}$112

Figure 6.28. Decrease in radius of the "front" observed in the second stage of drying for a silica suspension. The initial silica concentration is $\phi_i = 0.02$ and the front appears at 9.8 hours, corresponding to a silica concentration of $\phi_f = 0.60$113

Figure 6.29. Concentration of silica and Na^+ as functions of time within a single droplet with a) $\phi_i = 0.02$ and $[\text{Na}^+]_i = 3 \text{ mM}$, and b) $\phi_i = 0.02$ and $[\text{Na}^+]_i = 102 \text{ mM}$. The front appears at approximately 12 hours for this particular drop. The dehydration occurs at 5% relative humidity.116

Figure 6.30. Similar to the case with no salt, a "front" is observed in highly concentrated silica and NaCl suspensions, but a second phase appears soon after the front appears. In this particular set of images, $\phi_i = 0.021$ and $[\text{NaCl}]_i = 100$ mM. Approximately 8 minutes have elapsed between each image. Scale bar is 100 μm117

Figure 6.31. Final structures of dehydrated droplets containing silica and NaCl: a) encased, b) extruded, c) exploded. The final composition just prior to the appearance of the second phase is $\phi \sim 0.3$ and $[\text{NaCl}] \sim 2$ M. Scale bar is 100 μm118

Figure 6.32. Long term storage of droplets containing a silica suspension that was submerged in a water bath at $t = 2$ hours. In these images, $\phi_i = 0.02$ and $[\text{NaCl}]_i = 100$ mM, and $\phi_f = 0.03$ and $[\text{NaCl}]_f = 170$ mM.118

Figure 6.33. Turbidity is observed in bulk samples of silica suspensions containing salt at concentrations $[\text{NaCl}] = 170, 320, 430,$ and 630 mM from left to right.119

Figure 6.34. MSD for silica suspensions with concentrations of a) $\phi = 0.037$ and 170 mM NaCl, b) $\phi = 0.035$ and 320 mM NaCl, and c) $\phi = 0.033$ and 630 mM NaCl. Open symbols represent droplets that are dehydrating; filled symbols represent measurements taken after the device is submerged. The solid line is the effective viscosity of a dilute suspension of rigid spheres predicted by Einstein's formula. Time increases from top to bottom for each set of curves; the time elapsed is a) 286 hours, b) 117 hours and c) 10 hours.121

Figure 6.35. Effective viscosity of silica suspensions over time for varying salt concentrations of 170 mM (\bullet), 320 mM (\blacksquare), 430 mM (\blacktriangle), and 630 mM (\blacklozenge) NaCl. The dashed line indicates the maximum effective viscosity $\eta_{max} = 0.95$ Pa·s that can be probed with the current setup.122

Figure 6.36. Effective viscosity of salted silica suspensions over time for several drops in different microfluidic devices at a single silica and NaCl concentration. The symbols correspond to the following systems: $\phi = 0.032 \pm 0.003$ and $[\text{NaCl}] = 310 \pm 30$ mM (\bullet); $\phi = 0.035 \pm 0.003$ and $[\text{NaCl}] = 330 \pm 30$ mM (\blacksquare); $\phi = 0.033 \pm 0.003$ and $[\text{NaCl}] = 310 \pm 30$ mM (\circ); $\phi = 0.032 \pm 0.003$ and $[\text{NaCl}] = 300 \pm 30$ mM (\square); and $\phi = 0.032 \pm 0.003$ and $[\text{NaCl}] = 310 \pm 30$ mM (Δ).124

Figure 6.37. Complex modulus of the bulks samples of silica suspensions with added salt at an angular frequency of 1 rad/s. The silica concentration is equal to $\phi = 0.03$, and the salt concentrations are equal to 170 mM (\circ), 320 mM (\square), 430 mM (Δ), and 630 mM (\diamond).125

- Figure 6.38.** Effect of added salt concentration on flocculation time. The flocculation time in the droplets is defined as the time when $\eta_{eff} > 0.01$ Pa·s. The flocculation time in the bulk is defined as the time when $G^* > 10$ Pa.127
- Figure 6.39.** Time for 75% of the droplets sampled within an array to reach the final state (water – complete dehydration of droplet, NaCl – crystallization or no volume change, clay – no volume change). All concentrations given refer to the initial concentration of particles in the droplet.129
- Figure 6.40.** A "front" is observed in highly concentrated clay suspensions. In these images, $\phi_i = 0.004$, and the droplet was dehydrated at 5% relative humidity, however, the time required for the front to move through the drop varies with humidity. Scale bar is 100 μm130
- Figure 6.41.** Top and side views of a dehydrated clay drop. The drop diameter is equal to 61 μm and has a thickness of 27 μm . The depth of the channel is $h = 100$ μm . Scale bar is 100 μm131
- Figure 6.42.** Final clay concentration in drops containing clay suspensions as a function of relative humidity, with (●) and without (○) added salt. The initial clay concentration for all experiments is $\phi_i = 0.004$132
- Figure 7.43.** Dehydration of a trapped droplet containing a glycine solution ($C_i = 1.0$ M) in mineral oil over 12 hours at 5% relative humidity. Two hours have elapsed between each image from left to right. Scale bar is 100 μm151
- Figure 7.44.** Time for 75% of the droplets sampled within an array to reach the final state (water (○) – complete dehydration of droplet, NaCl (□ and Δ) and glycine (◆) – crystallization or constant droplet volume). All concentrations given refer to the initial concentration of the solute within the droplet.153
- Figure 7.45.** The probability that a droplet has not nucleated and crystallized at a given time for a glycine solution at the following initial concentrations: 0.5 M (●), 1.0 M (■), 2.0 M (▲). Experiment is carried out at 10% relative humidity.155
- Figure 7.46.** The probability that a droplet has not crystallized at a given time for a pure 1.0 M glycine solution (■) and a 1.0 M glycine solution with added salt ($[\text{NaCl}]_i = 100\text{mM}$ (∇) and 400 mM (◇)) or with 0.2% (v/v) silica nanoparticles (open hexagons). Experiments are carried out at 10% relative humidity. a) Full nucleation probability curves for all droplet compositions, with an expanded view of the first 10 hours shown in b).158
- Figure 7.47.** Spherical crystallization of glycine ($C_i = 1.0$ M) in a dehydrating microfluidic droplet at 10% relative humidity at 20°C. Time t on each image is equal to a) 0, b) 0.01, c) 0.06, and d) 0.11 seconds. Within a few seconds, e) the crystallized droplet begins to "age." The scale bar is 50 μm160

Figure 7.48. Growth of the effective radius of the glycine crystal for 1.0 M glycine (■); 1.0 M glycine with added salt (100 mM NaCl (∇) and 400 mM (◇)); and glycine with added silica (dilute (open star) and 0.2% (v/v) (open hexagon)). Data is only when a clear image of the growing crystal is observed and can be reasonably measured. Experiments are carried out at 10% relative humidity at 20°C.....161

Figure 7.49. Images of typical glycine crystals obtained in a microfluidic device. Note that in these experiments, spherical crystallization of glycine is first observed, and then the crystals age to yield crystals with the appearance of one of the four textures.164

Figure 7.50. Raman spectra of glycine crystals generated from the following conditions and formulations: 1.0 M glycine dehydrated at 5% and 50% relative humidity; 1.0 M glycine with 100 mM NaCl and 400 mM NaCl; and glycine with dilute amounts of silica and 0.2% silica particles. All experiments are carried out at 5% relative humidity unless otherwise stated. The expected location of the peaks for α -glycine (solid lines) and γ -glycine (dashed lines) are also included for comparison. Note that at least 10 crystals were scanned, but these are representative spectra from individual crystals.....166

Figure 7.51. XRD spectra of 1.0 M glycine dehydrated at 5% and 50% relative humidity; 1.0 M glycine with 100 mM NaCl and 400 mM NaCl. ~100 crystals are loaded onto the sample holder for these scans. Unless otherwise noted, experiments are carried out at 5% relative humidity.168

Chapter 1. Introduction

Product development is typically a costly endeavor, especially in the pharmaceutical and specialty chemicals industries. Numerous formulations are evaluated for a desired set of properties that fulfill the objectives in terms of efficacy, ease of downstream processing, and long-term storage. This requires an extensive set of screening and characterization techniques as well as enough sample to carry out these studies. For example, commercially available methods for screening active pharmaceutical ingredients require tens of microliters of fluid containing the test material for each experiment. In contrast, previous microfluidics experiments have provided a viable alternative to these traditional methods. Microfluidic techniques have been shown to successfully form monodisperse droplets with droplet volumes spanning from tens of picoliters to hundreds of nanoliters. This has led to many demonstrations of the success of droplet microfluidics to efficiently screen a system for a desired product formulation. However, the small sample volume combined with rapid, yet accurate detection and analysis techniques suggests that a microfluidic platform is uniquely suited for the purposes of probing specific properties of the test substance. In this work, we address the development of such a microfluidic platform that can be used to study phase transitions. The objective of this thesis is to demonstrate the use of microfluidic techniques to evaluate the underlying mechanisms governing the phenomena observed in screening studies.

Chapters 4 and 5 first discuss the control of droplet volume and emulsion structure using two different techniques of droplet formation and the

characterization of the basic microfluidic platform to study phase transitions. In Chapter 4, we focus on bubble and droplet generation in a microchannel with a rectangular cross-section. A geometric model is developed to describe the expected bubble or droplet shapes and structures. Although there are differences between “bubbles” versus “droplets” and “foams” versus “emulsions,” the geometric arguments presented in this chapter apply to both, and the terms are used interchangeably. The critical bubble volumes and volume fractions defining the transitions between structures are determined and used to generate a regime map for a given channel aspect ratio that covers the full range of possible monodisperse foam structures. The predicted regime maps are compared with experiments carried out in several microchannel aspect ratios with three nozzle types and various component fluids.

In Chapter 5, we use a different droplet generation technique that allows for the simultaneous formation and storage of drops. Aqueous drops are held stationary in a structure set by the network of traps for extended observation. Droplet dehydration is driven by the permeability of the microfluidic device material polydimethylsiloxane (PDMS), and the concentration gradient of water between the droplet and the ambient environment. We first show that in the case of pure water, the droplets continuously shrink and eventually disappear altogether. The rate of dehydration is examined as a function of parameters such as relative humidity, and the experiments are also performed for droplets containing salt. These results are compared to the diffusion of a spherical source that decreases in size over time. We also use the changing properties of the

droplet containing a concentrating solution to verify the accuracy of volume measurements made within the device. A protocol is developed to indirectly assess the accuracy of the model volume equations for specific droplet shapes.

Droplet dehydration is empirically controlled using the results from Chapter 5 to study the two phase transitions described in Chapters 6 and 7. In the first system, the dehydration and stability of particle suspensions are evaluated. Droplets containing silica or clay suspensions are fully dehydrated, and the final particle concentration is measured as a function of relative humidity, initial particle concentration, and initial salt concentration. The platform is combined with particle tracking techniques to probe changes in the fluid properties of silica suspensions over time. Dehydration is stopped at a desired particle concentration, and the effect of salt concentration on the suspension stability is monitored over time within single droplets. The effect of salt on the flocculation time is determined, spanning a large range of flocculation rates caused by the presence of 170 mM to 1.0 M salt at a constant silica concentration. These results are compared to bulk rheological measurements as well as previous studies on silica particle flocculation induced by increases in salt concentration.

Chapter 7 uses the microfluidic platform to study the crystallization of glycine. In this chapter, the array of stored droplets is used to obtain statistics on a stochastic process, while the individual droplets are monitored for high resolution measurements of crystal growth. Nucleation statistics and crystal growth of spherical glycine crystals are monitored as a function of glycine concentration and type of additive, which includes two concentrations of salt (100 and 400 mM) and

silica nanoparticles. Visual changes are also noted to determine the effect of humidity, salt, and silica nanoparticles on the physical appearance of the glycine crystals. The crystals are harvested and characterized off-chip using Raman spectroscopy and x-ray diffraction.

Chapter 8 summarizes the results and contributions of this work, which demonstrate proof of concept that the microfluidic platform provides a useful analysis tool for probing suspension stability over time and for understanding the mechanisms that govern crystallization. Future directions for this work are discussed, which continue the development of the microfluidic design from a PDMS prototype to a more robust platform that can be used to study aggregation and crystallization in other systems.

Chapter 2. Background

The success of microanalytical methods, such as chromatography and capillary electrophoresis, to rapidly perform highly accurate chemical analyses with small sample volumes became a starting point for the rise of microfluidics. The study of fluid flow in pipes with characteristic dimensions on the order of tens to hundreds of microns incorporates techniques developed for microelectromechanical systems (MEMS) and is applied to a variety of fields, including molecular biology, drug development, and separations. Droplet-based microfluidic techniques in particular are well-suited for applications in chemical analysis, yet they have also been considered as a method for generating designer particles and other high-value products.¹⁻⁴ This chapter broadly summarizes the types of microfluidic components that have been developed specifically for droplet generation, which forms the basis for the following chapters. It also briefly discusses the methods and materials that have been used to create these components and their impact on analysis applications.

Microfluidic techniques are primarily concerned with the manipulation of fluid flow in microchannels. Viscous forces dominate at these length scales rather than inertia, and the Reynolds number is typically on the order of one, indicating laminar flow. Fluid flow can be controlled using a variety of driving forces and external fields. In many cases, fluid flow is driven by a pressure gradient, and is controlled by external pumps that control the flow rate of the fluid. Fluids may also be manipulated with capillary forces and controlled patterning of the channel surfaces; electrokinetic techniques such as electro-osmotic flow; and other driving

forces including temperature gradients, centrifugal forces, magnetic fields, and acoustic streaming. Reviews of these driving forces and on-chip methods for pumping fluid can be found elsewhere,^{2,5-9} but the studies presented in this work implement pressure driven fluid flow.

Multiphase flows can be controlled using similar techniques, and offer additional tools for microfluidic systems. The subsequent application of droplets varies in scope, which have been used to produce tunable emulsions; to generate particles designed to have a specific shape and composition; or applied as microreactors with identical chemical environments. Due to this wide range of applicability, the controlled generation and manipulation of droplets is well-studied and documented.¹⁰⁻¹⁹

Droplet generation occurs from the breakup the dispersed phase due to forces exerted by the continuous phase. This is commonly carried out using microfluidic nozzles, which are categorized under three distinct geometries. In T-junctions, droplets form in perpendicularly flowing streams of the continuous and dispersed phases. Droplet formation in a co-flow device involves the concentric or parallel flow of the dispersed phase with the continuous phase, which results in breakup downstream of where the two phases first come in contact. In flow-focusing geometries, the phases are forced to flow through a restriction, causing an instability in the dispersed phase stream which results in droplet formation near the orifice.¹² Once formed, the droplets self-assemble into ordered structures with a regular spacing between droplets. Many theoretical and empirical models have been developed to accurately predict the droplet size and emulsion structure as a

function of flow rate for a given nozzle geometry and set of channel dimensions.^{12,13,18-21}

Microfluidic nozzles can quickly generate a large number of monodisperse droplets within minutes. The total amount of droplets is limited by the starting amounts of the dispersed and continuous phases. Previous studies have observed tip-streaming in flow-focusing geometries that form submicron-sized droplets, but otherwise, the nozzle and channel geometry will dictate the accessible range of droplet sizes and the emulsion structure of the droplets that can be generated. Smaller droplets may be formed, however, by including downstream features such as bifurcating channels to split preformed droplets in to the desired size.^{11,22,23} To decouple the droplet size from the emulsions structure, another droplet generation geometry has been reported that includes an array of a base unit consisting of a trap and bypass channel. A slug of the dispersed phase fills both the trap and bypass, and droplet pinch-off is similar to that observed in T-junctions. The droplet size is determined by the trap geometry, and is held stationary within the trap as the remainder of the dispersed phase exits the device through the bypass. While the emulsion structure is now independent of the droplet size, the total number of droplets formed is determined by the number of traps in the network.²⁴

Depending on the subsequent application, it may be necessary to carry out a significant number of iterations to find the appropriate droplet generation technique and geometric parameters to achieve the desired outcomes. Common microfluidic device fabrication methods include glass etching and traditional MEMS techniques, but these can be costly and the devices can be tedious to

fabricate for every new design. Soft lithography rectifies both of these issues, especially when combined with an inexpensive polymeric material that will form the walls of the microchannel. In this method, a stamp containing the positive relief of the channels is used to pattern the polymer that becomes the final microfluidic device. The stamp can be used repeatedly to pattern as many devices as desired.²⁶

The most common polymeric material used in microfluidic studies is polydimethylsiloxane (PDMS), a two-part elastomer that can be cured at room temperature to yield a flexible material. PDMS can replicate submicron features from the stamp and is optically transparent. Once cured, two pieces of PDMS may be irreversibly bonded to each other by changing the naturally hydrophobic surface to a hydrophilic one with the application of air or oxygen plasma.^{1,10,11,25-29} The ease of device fabrication using PDMS allows for rapid prototyping but is also used for initial demonstrations of proof of concept for applications pertaining to analysis. The transparency of the elastomer is useful for studies where the device contents can be observed with various illumination techniques, including brightfield or fluorescence illumination. There are, however, several characteristics of PDMS that limit its applicability. The natural hydrophobicity of the PDMS surface is difficult to change permanently, which can lead to issues regarding the control of fluid flow.^{30-32,33} PDMS can also be significantly impacted by various reagents and solvents, specifically low molecular weight alkanes and low viscosity silicone oils, which can swell PDMS and alter the desired microchannel design. Substances that diffuse through PDMS

can also cause the device material to become cloudy, thereby rendering it ineffective for chemical analysis.³⁴⁻³⁶ Despite these issues, few materials have been developed that are as simple to work with as PDMS, and it remains as one of the most common materials used in the microfluidic channel design process for droplet-based analysis applications.

References

1. Whitesides, G. M. The origins and the future of microfluidics. *Nature*. **2006**, *442*, 368-373.
2. Mark, D.; Haeberle, S.; Roth, G.; von Stetten, F.; Zengerle, R. Microfluidic lab-on-a-chip platforms: requirements, characteristics and applications. *Chemical Society Reviews*. **2010**, *39*, 1153-1182.
3. Nguyen, N. T.; Wereley, S. T. *Fundamentals and Applications of Microfluidics*, Artech House, 2002,
4. Stone, H. A.; Kim, S. Microfluidics: Basic issues, applications, and challenges. *AIChE J.* **2001**, *47*, 1250-1254.
5. Stone, H. A.; Stroock, A. D.; Ajdari, A. Engineering Flows in Small Devices: Microfluidics Towards a Lab-on-a-Chip. *Annual Review of Fluid Mechanics*. **2004**, *36*, 381-411.
6. Squires, T. M.; Quake, S. R. Microfluidics: Fluid physics at the nanoliter scale. *Reviews of Modern Physics*. **2005**, *77*, 977-1026.
7. Laser, D. J.; Santiago, J. G. A review of micropumps. *Journal of Micromechanics and Microengineering*. **2004**, *14*, R35.
8. Gravesen, P.; Branebjerg, J.; Jensen, O. S. Microfluidics-a review. *Journal of Micromechanics and Microengineering*. **1993**, *3*, 168.
9. *Advances in Microfluidics*, R. T. Kelly, ed. InTech, 2012, 250.
10. Seemann, R.; Brinkmann, M.; Pfohl, T.; Herminghaus, S. Droplet based microfluidics. *Reports on Progress in Physics*. **2012**, *75*, 016601.
11. Teh, S.-Y.; Lin, R.; Hung, L.-H.; Lee, A. P. Droplet microfluidics. *Lab on a Chip*. **2008**, *8*, 198-220.
12. Christopher, G. F.; Anna, S. L. Microfluidic methods for generating continuous droplet streams. *Journal of Physics D: Applied Physics*. **2007**, *40*, R319.
13. Baroud, C. N.; Gallaire, F.; Dangla, R. Dynamics of microfluidic droplets. *Lab on a Chip*. **2010**, *10*, 2032-2045.
14. Song, H.; Chen, D. L.; Ismagilov, R. F. Reactions in Droplets in Microfluidic Channels. *Angewandte Chemie International Edition*. **2006**, *45*, 7336-7356.
15. Velankar, B. J. A. a. S. S. Pressure drops for droplet flows in microfluidic channels. *Journal of Micromechanics and Microengineering*. **2006**, *16*, 1504.
16. Utada, A. S.; Lorenceau, E.; Link, D. R.; Kaplan, P. D.; Stone, H. A.; Weitz, D. A. Monodisperse Double Emulsions Generated from a Microcapillary Device. *Science*. **2005**, *308*, 537-541.
17. Pompano, R. R.; Liu, W.; Du, W.; Ismagilov, R. F. Microfluidics Using Spatially Defined Arrays of Droplets in One, Two, and Three Dimensions. *Annual Review of Analytical Chemistry*. **2011**, *4*, 59-81.

18. Garstecki, P.; Fuerstman, M. J.; Stone, H. A.; Whitesides, G. M. Formation of droplets and bubbles in a microfluidic T-junction-scaling and mechanism of break-up. *Lab on a Chip*. **2006**, *6*, 437-446.
19. Shah, R. K.; Shum, H. C.; Rowat, A. C.; Lee, D.; Agresti, J. J.; Utada, A. S.; Chu, L.-Y.; Kim, J.-W.; Fernandez-Nieves, A.; Martinez, C. J.; Weitz, D. A. Designer emulsions using microfluidics. *Materials Today*. **2008**, *11*, 18-27.
20. Zheng, B.; Tice, J. D.; Roach, L. S.; Ismagilov, R. F. A Droplet-Based, Composite PDMS/Glass Capillary Microfluidic System for Evaluating Protein Crystallization Conditions by Microbatch and Vapor-Diffusion Methods with On-Chip X-Ray Diffraction. *Angewandte Chemie International Edition*. **2004**, *43*, 2508-2511.
21. Utada, A. S.; Fernandez-Nieves, A.; Stone, H. A.; Weitz, D. A. Dripping to Jetting Transitions in Coflowing Liquid Streams. *Physical Review Letters*. **2007**, *99*, 094502.
22. Christopher, G. F.; Bergstein, J.; End, N. B.; Poon, M.; Nguyen, C.; Anna, S. L. Coalescence and splitting of confined droplets at microfluidic junctions. *Lab on a Chip*. **2009**, *9*, 1102-1109.
23. Hatch, A. C.; Fisher, J. S.; Pentoney, S. L.; Yang, D. L.; Lee, A. P. Tunable 3D droplet self-assembly for ultra-high-density digital micro-reactor arrays. *Lab on a Chip*. **2011**, *11*, 2509-2517.
24. Boukellal, H.; Selimovic, S.; Jia, Y.; Cristobal, G.; Fraden, S. Simple, robust storage of drops and fluids in a microfluidic device. *Lab on a Chip*. **2009**, *9*, 331-338.
25. Whitesides, G.; Stroock, A. Flexible methods for microfluidics. *Physics Today*. **2001**, *54*, 42-48.
26. McDonald, J. C.; Whitesides, G. M. Poly(dimethylsiloxane) as a Material for Fabricating Microfluidic Devices. *Accounts of Chemical Research*. **2002**, *35*, 491-499.
27. Minteer, S. D. *Microfluidic Techniques: Reviews and Protocols*, Humana Press, 2006,
28. Sollier, E.; Murray, C.; Maoddi, P.; Di Carlo, D. Rapid prototyping polymers for microfluidic devices and high pressure injections. *Lab on a Chip*. **2011**, *11*, 3752-3765.
29. Jo, B.-H.; Van Lerberghe, L. M.; Motsegood, K. M.; Beebe, D. J. Three-dimensional micro-channel fabrication in polydimethylsiloxane (PDMS) elastomer. *Journal of Microelectromechanical Systems*. **2000**, *9*, 76-81.
30. Eddington, D. T.; Puccinelli, J. P.; Beebe, D. J. Thermal aging and reduced hydrophobic recovery of polydimethylsiloxane. *Sensors and Actuators B: Chemical*. **2006**, *114*, 170-172.
31. Berdichevsky, Y.; Khandurina, J.; Guttman, A. s.; Lo, Y.-H. UV/ozone modification of poly(dimethylsiloxane) microfluidic channels. *Sensors and Actuators B: Chemical*. **2004**, *97*, 402-408.
32. Efimenko, K.; Wallace, W. E.; Genzer, J. Surface Modification of Sylgard-184 Poly(dimethyl siloxane) Networks by Ultraviolet and

- Ultraviolet/Ozone Treatment. *Journal of Colloid and Interface Science*. **2002**, *254*, 306-315.
33. Zhou, J.; Ellis, A. V.; Voelcker, N. H. Recent developments in PDMS surface modification for microfluidic devices. *Electrophoresis*. **2010**, *31*, 2-16.
 34. Lee, J. N.; Park, C.; Whitesides, G. M. Solvent Compatibility of Poly(dimethylsiloxane)-Based Microfluidic Devices. *Analytical Chemistry*. **2003**, *75*, 6544-6554.
 35. Provin, C.; Fujii, T. Reaction-diffusion phenomena in a PDMS matrix can modify its topography. *Lab on a Chip*. **2011**, *11*, 2948-2954.
 36. Toepke, M. W.; Beebe, D. J. PDMS absorption of small molecules and consequences in microfluidic applications. *Lab on a Chip*. **2006**, *6*, 1484-1486.

Chapter 3. Materials and Methods

In order to facilitate the microfluidic design process, we use standard soft lithography techniques to fabricate the microfluidic devices that are used to study the droplet formation and subsequent storage discussed in the following chapters. Droplet formation is carried out using microfluidic nozzles with different geometries and operating conditions, while droplet storage designs are tuned towards the specific application of the microfluidic platform. Both of these systems require a significant number of iterations and, therefore a fabrication technique that is easily adapted for each design. Soft lithography is well-suited for the development of microfluidic designs, as new microchannel designs can be fabricated by simply changing the printed transparency mask template used to pattern the mold. In this chapter, the protocol used to make elastomeric microchannels is described.

3.1. Microfluidic Device Fabrication

Microfluidic channels are fabricated using standard soft photolithography techniques that have been described in detail elsewhere.¹⁻⁴ In this method, a relief mold of the channel design is created by patterning a photoresist onto a silicon wafer. An elastomer is then poured onto the mold and cured. The elastomer replicates the features of the mold and, once cured, can be removed from the mold to create open microchannels. A second layer of elastomer is irreversibly bonded to the first patterned layer to create a closed microfluidic channel.

Microchannel molds are fabricated within a laminar flow hood in a multi-step process that includes proper wafer preparation to ensure adhesion of the photoresist pattern. A 3” silicon wafer (Cz growth method, P/Boron dopant, one side polish, <100> slide orientation, 1-10 Ω -cm resistivity, 15 ± 2 mils, test grade, SEMI standard flats) is cleaned using sequential rinses of acetone, isopropyl alcohol, and water. The wafer is then dried using nitrogen gas before being placed in a spin coater (Laurell Technologies 150 mm Spin Coater Model WS-650Mz-23NPP). A layer of the UV curable photoresist SU-8 3050 (Microchem Corp.) is spin coated to a constant layer thickness h . To control the SU-8 layer thickness and therefore the depth of the channel, a two-step spin coating process is used. All devices made for the experiments described here have a channel depth of $100 \pm 5 \mu\text{m}$; however, the depth of the channel can be varied by following the specifications listed in Table 3.1. Note that while SU-8 layer thicknesses were previously verified using a profilometer (Dektak 3 Surface Profilometer), the molds made for the experiments detailed here were not individually measured.

Depth, h (μm)	Spread Cycle (Step 1)			Spin Cycle (Step 2)		
	Speed (RPM)	Ramp (RPM/s)	Time (s)	Speed (RPM)	Ramp (RPM/s)	Time (s)
155	500	85	20	1000	340	30
105				1500		
80				2000		
65				3000		

Table 3.1. SU-3050 thickness as a function of spin cycle speed.

Once the silicon wafer has been coated with photoresist, a pre-bake or soft bake step is used to accelerate the evaporation of solvent from the photoresist to form a soft, less tacky layer. The recommended time for this step varies with film

thickness,⁵ but the following procedure is used with the channel depths listed in Table 1. The SU-8 coated wafer is transferred to a hot plate (PMC Dataplate 720 Series Digital Hot Plate), where it is baked in a two-step temperature ramp: the wafer is heated to 65°C at a ramp of 300°C/hr and held for five minutes, then heated to 95°C at the same ramp speed and held for fifteen minutes. Throughout the pre-bake time, the wafer is rotated 180° every few minutes to ensure layer uniformity. Prior to UV exposure, the wafer is removed from the hot plate and allowed to equilibrate at room temperature for five minutes.

In order to create microchannels, the SU-8 must be exposed to UV light to crosslink specific areas patterned by a transparency mask. The design printed on the transparency mask is drawn in DraftSight (Dassault Systèmes) but can be made using any similar computer-aided drawing software. The intensity and exposure time is designated by the thickness of the photoresist layer; underexposure decreases SU-8 adhesion, while overexposure creates uneven channels. The cooled silicon wafer is placed on a square plastic holder. A transparency mask with the microfluidic channel design printed at 20,000 dpi (CAD/Art Services, Inc.) is manually aligned with the wafer. In order to obtain vertical channel walls, a square glass filter that eliminates wavelengths below 360 nm is placed over the transparency, making a four-layer sandwich comprised of the plastic holder, wafer, transparency, and glass filter layered bottom to top. The manufacturer recommends 150-250 mJ/cm² for the SU-8 thicknesses listed in Table 1. The collimated UV light source (OAI 150 200W UV Exposure System) outputs a power of 3.14 mW, as measured by a power meter (Newport Power

Meter Model 1815-C), and so the wafer is exposed to UV light for 90 seconds to crosslink the epoxy.

After UV exposure, the silicon wafer is subjected to a second, two-step post-bake similar to the pre-bake: the wafer is heated to 65°C at 300°/hr and held for one minute, and then heated to 95°C at the same ramp speed and held for five minutes. After the 95°C step, the microchannel design should be visible in the photoresist. The wafer is allowed to cool to room temperature before being placed in a bath of SU-8 Developer (Microchem Corp.) for twenty minutes to develop the photoresist. During this time, the developer solution is gently agitated using a magnetic stirrer to promote the removal of any uncross-linked photoresist. Once developed, the wafer is rinsed with isopropyl alcohol and dried using nitrogen gas. The silicon wafer with cross-linked SU-8 is allowed to finish drying for at least an hour prior to use and is now a finished microchannel mold containing a relief pattern of the desired microchannel design.

Microfluidic devices are made using polydimethylsiloxane (PDMS), which comes as two-part elastomer kit (Dow Corning Sylgard 184). The prepolymer and cross-linking agent are mixed in a 10:1 mass ratio for two minutes and degassed for two minutes using a centrifugal mixer (Thinky Mixer AR-100). The mixture is then poured over the prepared channel mold, which sits in a 3” petri dish. A second, empty petri dish serves as the mold for a flat, unpatterned PDMS slab. The PDMS-filled petri dishes are baked for two hours at 60°C and then carefully cut and peeled off the mold. Inlet and outlet holes are punched into the PDMS slab patterned with the microchannels using a tissue punch (Harris

Uni-Core, Tip ID 1.0mm, OD 1.26mm). The two PDMS slabs are bonded by exposing the elastomer surfaces to air plasma (Harrick Plasma Cleaner PDC-32G) for sixty seconds and then placing the two surfaces in contact to create an irreversible seal. The surface of the PDMS elastomer is rendered hydrophilic by the plasma exposure. The bonded PDMS devices are baked at 60°C for two hours after contact to complete the bonding process and to allow the microchannel walls to revert back to hydrophobic surfaces.^{6,7}

3.2.Materials

Mineral oil (Fisher Scientific), 100 cSt silicone oil (Gelest, Inc.), and octanol (Fisher Scientific) are filtered through a 0.45 µm filter (Thermo Scientific Nalgene 25mm Syringe Filters). The oils are saturated with water by continuously mixing the oil with water for an hour using a magnetic stirrer and a stir bar. The two phases are then allowed to separate overnight, and the oil layer is collected and stored for later use. Span 80 (Sigma Aldrich) is added to the mineral oil in concentrations of 1, 3, and 5 wt. %. Deionized water (resistivity = 18.2 MΩ-cm) is obtained from a water purification system (Thermo Scientific Barnstead EasyPure II) and is used to make all aqueous solutions and suspensions. Materials used in specific experiments will be discussed in subsequent chapters.

3.3.Data Acquisition and Data Analysis

Droplets are monitored using an inverted microscope (Nikon Eclipse Ti-U or TE2000-U) fitted with either a 2X or 4X objective and observed in bright field

illumination. The Nikon TE2000-U is also used with phase contrast illumination or with crossed polarizers as needed. Images are recorded using a camera with either CCD or CMOS sensors (Allied Vision Technologies Guppy Pro; Allied Vision Technologies Prosilica; Redlake IDT XS5; or Vision Research Phantom v9.1), interfaced with the microscope using an extra viewing port. Large droplet arrays are imaged with a wider field of view using an optical table (Richards Corporation Image Interpretation Systems HFO-4 with a Bausch and Lomb microscope) fitted with a 1X objective and an additional magnification ranging from 0.6 to 3.3X. The camera connected to the optical table is a CCD camera (Panasonic WV-CD22).

Each microscope, objective, and camera grouping requires a separate calibration factor to convert image pixels to micrometers. The calibration value is calculated using a stage micrometer (Edmund Optics) that is 1 mm long with 100 divisions, yielding 10 μm calibration sections. An image of the micrometer is taken and analyzed using MATLAB Image Processing Toolbox (Mathworks) to obtain an average pixel per micron calibration factor with a corresponding standard deviation. Table 3.2 lists all of the calibration factors used for the dehydration experiments described in the following chapters.

Microscope	Camera	Magnification	Conversion Factor \pm Standard. Deviation
Nikon TE2000-U	IDT XS5	2X * 1.5	0.190 \pm 0.004 pixels/ μm
	Guppy Pro	2X * 1.5	0.520 \pm 0.010 pixels/ μm
	Prosilica	2X * 1.5	0.200 \pm 0.004 pixels/ μm
Nikon Ti-U	Phantom	4X	0.363 \pm 0.007 pixels/ μm

Table 3.2. Pixel to micron conversion factors used to determine droplet volumes.

3.4.References

1. Duffy, D. C.; McDonald, J. C.; Schueller, O. J. A.; Whitesides, G. M. Rapid Prototyping of Microfluidic Systems in Poly(dimethylsiloxane). *Analytical Chemistry*. **1998**, *70*, 4974-4984.
2. Seemann, R.; Brinkmann, M.; Pfohl, T.; Herminghaus, S. Droplet based microfluidics. *Reports on Progress in Physics*. **2012**, *75*, 016601.
3. Whitesides, G.; Stroock, A. Flexible methods for microfluidics. *Physics Today*. **2001**, *54*, 42-48.
4. Sollier, E.; Murray, C.; Maoddi, P.; Di Carlo, D. Rapid prototyping polymers for microfluidic devices and high pressure injections. *Lab on a Chip*. **2011**, *11*, 3752-3765.
5. SU-8 3000 Data Sheet. Microchem Corp.
6. Eddington, D. T.; Puccinelli, J. P.; Beebe, D. J. Thermal aging and reduced hydrophobic recovery of polydimethylsiloxane. *Sensors and Actuators B: Chemical*. **2006**, *114*, 170-172.
7. Fritz, J. L.; Owen, M. J. Hydrophobic Recovery of Plasma-Treated Polydimethylsiloxane. *The Journal of Adhesion*. **1995**, *54*, 33-45.

Chapter 4. Tuning Bubbly Structures in Microchannels

4.1 Introduction

Bubbles and droplets form the basic constituents of foams and emulsions, which have interesting bulk properties arising from the bubble size, size distribution, and placement within the surrounding medium. Foam or emulsion structure is particularly important in a number of applications. A regular spatial structure of monodisperse pores provides a 3D model tissue scaffold system that mimics the extracellular matrix and can be used to perform systematic studies of intercellular mechanisms.¹ The sound frequencies that can be transmitted through a bubbly medium depend on the spacing, crystal structure, and size of the bubbles within that medium.² In lab-on-a-chip devices, the packing of monodisperse drop reactors into ordered arrays enables high throughput assays.³

In microscale geometries, the minimal impact of inertia and the strong influence of viscous stresses and capillarity lead to regular breakup of the dispersed phase stream to form monodisperse bubbles and droplets.⁴⁻⁷ The resulting bubble or droplet volume and the qualitative foam or emulsion structure have been shown to be functions of fluid properties, operating flow parameters, and channel geometry.^{1,4,5,7-10} The presence of surface active species such as surfactants, proteins, and nanoparticles will also influence the dispersed phase size, shape, and structure.^{6,9,11} Scaling arguments and simplified models using the capillary number Ca and the volumetric flow rate ratios have been developed to characterize bubble and droplet size and frequency of formation, but relatively

little attention has been given to describing the downstream shape and structure of bubbles or droplets within a given device.^{5,6,12}

The structure of a foam is determined by the bubble volume and the gas volume fraction in the foam, and is strongly influenced by the presence of physical boundaries. In general, dry foams are those with high gas fractions and faceted bubbles that form Plateau borders with neighboring bubbles.¹³ In contrast, wet foams contain larger liquid fractions such that bubbles maintain a more spherical shape.^{7,14} When a foam is contained within a duct of comparable dimensions to the bubble size, the channel geometry influences bubble shape and arrangement. For example, in a rectangular microchannel, if the bubble size increases for a fixed gas fraction, the bubbles will become too large to fit within the rectangular channel cross-section as a sphere. When the bubble diameter exceeds the channel depth, the bubble flattens to form a “pancake” shape.¹² Typical images of spherical and pancake bubbles are shown in Fig. 4.1a and the pancake bubble shape is shown schematically in Fig. 4.2. When the pancake diameter exceeds the channel width, the bubble fills the cross-section and elongates to form a “slug” (Figs. 4.1b and 4.3).¹⁵

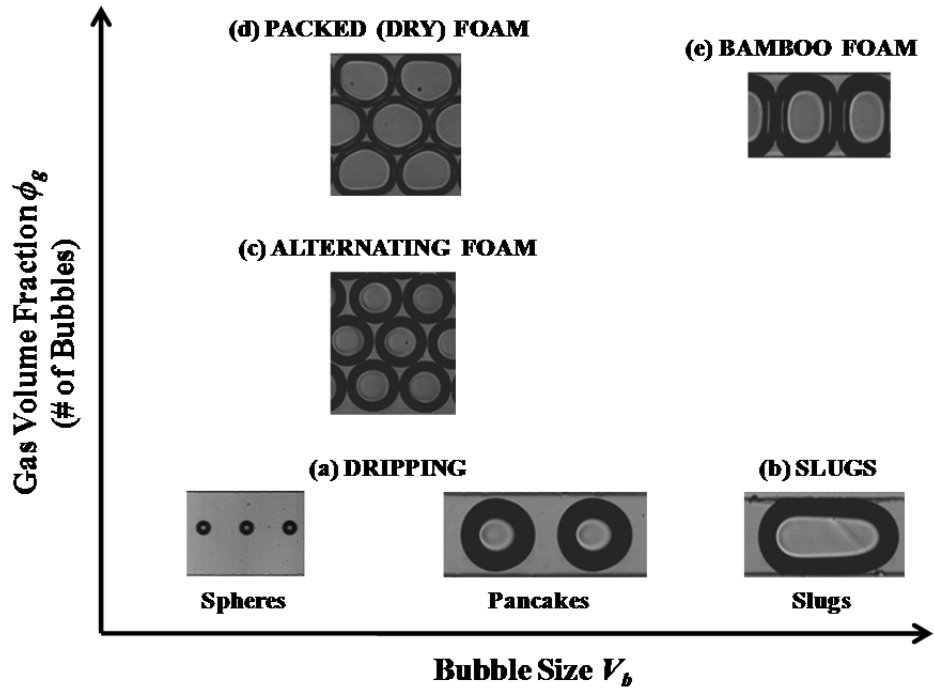


Figure 4.1. Typical images of bubble shapes and structure qualitatively organized in terms of gas volume fraction and bubble size.

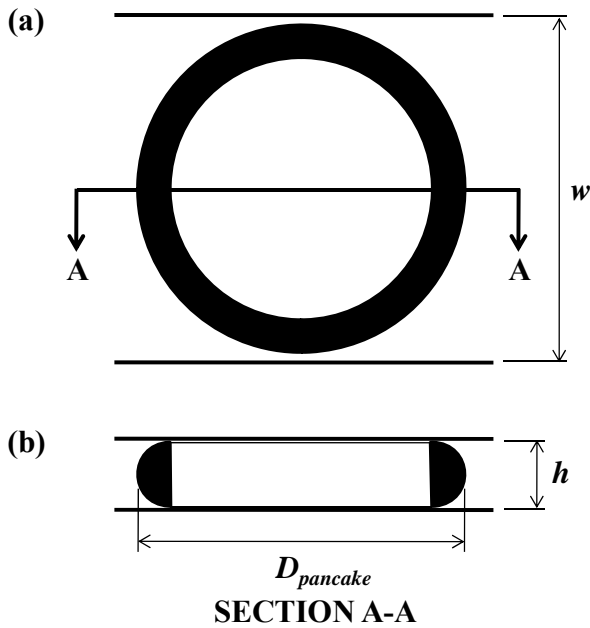


Figure 4.2. Schematic diagrams of (a) top and (b) side views of a pancake bubble in a microchannel where $w > h$.

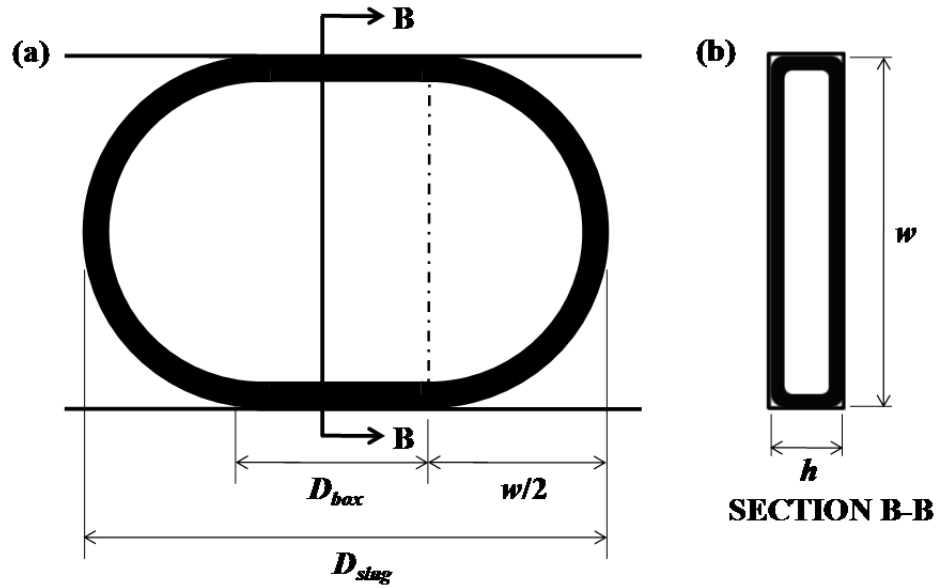


Figure 4.3. Schematic diagrams of (a) top and (b) side views of a slug bubble in a microchannel where $w > h$.

If the gas volume fraction increases for a fixed bubble size, then the arrangement of bubbles in the channel also depends on the microchannel geometry. Previous studies report five distinct types of monodisperse bubbly structures that can be formed in microfluidic devices: dripping (Fig. 4.1a), slugs (Fig. 4.1b), alternating foam (Fig. 4.1c), packed foam (Fig. 4.1d), and bamboo foam (Fig. 4.1e).^{7,15} Dripping (Fig. 4.1a) is defined as a single row of bubbles equally spaced along the centerline of the channel and applies to both spherical and pancake bubbles.⁷ Slugs (Fig. 4.1b) are essentially the same as dripping, but the bubble shape is that of a slug.¹⁵ Alternating foam (Fig. 4.1c) occurs at higher gas volume fractions when the bubbles can no longer fit within a single row and must stagger to form multiple rows. If the volume fraction increases further, the bubbles will adopt a packed structure (Fig. 4.1d), where the bubble shapes must deviate from spherical to fit into the confined space.¹⁴ Finally, the bubbles will

pack together to form a ladder-like structure denoted “bamboo foam” for a single row of packed slug-shaped bubbles (Fig. 4.1e).⁷

When monodisperse bubbles are less confined, they arrange into well-ordered structures. At low gas volume fractions, the foam structure is similar to the packing of hard spheres in a small gap between two planar surfaces. The formation of two-dimensional “crystals” containing spherical microbeads has been studied by Kumacheva *et al.*, who characterized the packing structure as a function of the ratio of microchannel width to bead size for a constant microchannel height.¹⁶ In another example of the influence of the microchannel width, Yang *et al.*¹⁷ characterized the dynamic structures of droplets after formation as a function of outlet geometry immediately after the nozzle. The authors found that different pancake-shaped droplet structures, corresponding to those that we denote dripping and alternating foam, formed depending on the shape of the expansion area between the nozzle and the final rectangular cross-section. The packing transition from two to three dimensions was observed by Pieranski *et al.* and characterized as a function of separation distance between the two confining surfaces.¹⁸ A change in the total length of the channel will also induce a change in the structure, as described in compression studies performed by Fleury *et al.*¹⁹ In three-dimensional space, Hatch *et al.*³ examined the packing of approximately 50 μm spheres into multiple layers of droplets in a large microfluidic collection chamber. The generated droplets self-assembled into various packing configurations, including hexagonally close packed and cubic close packed. The authors considered microchannel dimensions much larger than

the drop diameter and intermediate volume fractions ($\phi > 0.5$) in which the bubbles assembled but remained spherical. At higher gas volume fractions, the shape deformation from a sphere must be taken into account in the packing of bubbles. Two studies by Garstecki and Whitesides describe the possible periodic structures of dry foams that are comprised of individual bubbles whose shapes deform to minimize the local interfacial energy.^{20,21} Foams formed at higher flow rates adopt higher energy structures. Hashimoto *et al.* showed that the combination of multiple bubble and droplet generators gives rise to foams and emulsions consisting of inclusions of varying size and composition that will also adopt periodic structures.

In confined geometries, the conditions at which a foam transition from one structure to another strongly depend upon the microchannel geometry, the volume of the bubbles V_b , and the gas fraction ϕ_g . In the present study, we will characterize the bubble shape and foam structure using these two parameters in rectangular microchannels with dimensions comparable to the bubble size in the present study. A geometric model will be developed to describe the expected bubble shapes and structures. In the discussion that follows we will use the terms “bubble” and “droplet”, and the terms “foam” and “emulsion” interchangeably. Although there are differences between the two, the geometric arguments that we present here apply equally well to both. The critical bubble volumes and volume fractions defining the transitions between structures will be determined and used to generate a regime map for a given channel aspect ratio. The predicted regime maps will be compared with experiments corresponding to several microchannel

aspect ratios, various component fluids, and three different nozzle types. The experiments and model encompass bubble volumes from 10^{-2} to 10^2 nL and gas volume fractions from 0.01 to 1, covering the full spectrum of possible monodisperse foam structures.

4.2 Geometric Model for Foam Structure

In this section, we develop a simplified model describing the structure of a foam containing a uniform bubble size and confined within a rectangular microchannel. We will assume that the channel depth h is less than or equal to the width w , and that the channel length L is significantly longer than either of these two dimensions ($h \leq w \ll L$). The underlying hypothesis is that the foam structure is independent of the manner in which it is produced. In other words, we consider static conditions and neglect the influence of nozzle type, flow conditions, fluid properties (e.g. viscosity and interfacial tension), and channel wall material. We therefore develop geometric arguments for the foam structure, first defining each bubble shape transition, followed by each bubble structure transition.

Assuming that a bubble will attain a spherical shape if unbounded, the bubbles will remain spherical until the diameter of the bubble D_{sphere} exceeds the depth of the channel

$$D_{sphere} \geq h \quad (4.1)$$

Larger bubbles will be confined by the top and bottom walls of the microchannel and will adopt a pancake-like shape as shown schematically in Fig. 4.2. Expressing the diameter of the bubble in terms of its volume,

$$D_{sphere} = \left(\frac{6}{\pi} V_b \right)^{1/3}, \quad (4.2)$$

the critical bubble volume $V_{b,sp}$ at which the sphere-to-pancake transition occurs is given by

$$V_{b,sp} = \frac{\pi}{6} h^3 \quad (4.3)$$

Approximating the shape of a pancake bubble as a cylinder surrounded by a semi-circular cap, the volume of a pancake bubble $V_{pancake}$ can be estimated by a volume of revolution integral,

$$V_{pancake} = \pi \int_{-h/2}^{h/2} \left[\left(\frac{h^2}{4} - z^2 \right)^{1/2} + \left(\frac{D_{pancake} - h}{2} \right) \right]^2 dz \quad (4.4)$$

where $D_{pancake}$ is the projected diameter of the pancake and z is the axial distance from the equator of the pancake, or the midplane between the upper and lower surfaces shown in Fig. 4.2b. Note that Eq. (4.4) is written in the cylindrical coordinate system of the bubble, where the bubble profile (Fig. 4.2b) is rotated about the central axis of the bubble. The first term in the integrand of Eq. (4.4) represents the shape of the circular cap and the second term describes the interior cylinder. The integral results in a pancake volume given by

$$V_{pancake} = \frac{\pi h^3}{6} + \frac{\pi h}{4} (D_{pancake} - h) \left(\frac{\pi h}{2} + D_{pancake} - h \right) \quad (4.5)$$

Solving for the projected diameter $D_{pancake}$ of a pancake bubble with volume V_b yields

$$D_{pancake} = \left[\frac{4V_b}{\pi h} + \frac{h^2}{48} (3\pi^2 - 32) \right]^{1/2} - \frac{h}{4} (\pi - 4) \quad (4.6)$$

When the projected diameter of the pancake bubble exceeds the width of the channel,

$$D_{pancake} \geq w, \quad (4.7)$$

the bubble becomes elongated into a slug-like shape. Substituting Eq. (4.6) into Eq. (4.7) reveals a critical volume $V_{b,ps}$ at which the pancake-to-slug transition occurs,

$$V_{b,ps} = \frac{\pi}{8} wh \left[(\pi - 4)h + 2w \right] + \frac{\pi}{24} h^3 (10 - 3\pi) \quad (4.8)$$

It should be noted that the critical volumes for both shape transitions (Eqs. (4.3) and (4.8)) depend only on the channel dimensions. Once the bubble volume has exceeded the critical value $V_{b,ps}$, the bubble is confined by all four walls of the channel, thereby adopting a cross-sectional shape that conforms to that of the channel (Fig. 4.3b). The slug will adopt a finite radius of curvature in the corners of the rectangular cross-section due to surface tension. We neglect this small volume in our estimates, but note that these corners will strongly influence the speed at which the bubbles flow along the channel.^{22,23}

The slug shape can be approximated as a box with two half-pancake endcaps, where the diameter $D_{pancake}$ is equal to the width of the channel w . The volume of a slug bubble (Fig. 4.3a) is calculated by

$$V_{slug} = V_{box} + V_{pancake}, \quad (4.9)$$

where V_{box} is the remaining bubble volume not accounted for in the half-pancake endcaps. The relevant bubble dimension is the length of the slug bubble D_{slug} (Fig. 4.3a) along the axial coordinate of the microchannel. By neglecting curvature in the corners of the box cross-section and assuming that the bubble perfectly conforms to the rectangular cross-section, we can approximate the length of the box D_{box} as

$$D_{box} = \frac{1}{wh} V_{box} \quad (4.10)$$

The total length of the bubble is then

$$D_{slug} = w + D_{box} \quad (4.11)$$

Substituting Eqs. (4.5), (4.9), and (4.10) into Eq. (4.11) yields the slug bubble length for a bubble volume V_b in terms of channel dimensions and bubble volume

$$D_{slug} = w + \frac{1}{wh} \left\{ V_b - \left[\frac{\pi h^3}{6} + \frac{\pi h}{4} (w-h) \left(\frac{\pi h}{2} + w-h \right) \right] \right\} \quad (4.12)$$

In addition to bubble shape transitions, there are also bubble structure transitions that are functions of gas volume fraction, ϕ_g . The bubble structure is determined by the spatial arrangement of the bubbles in the available channel volume. The number of bubbles n_b that corresponds to a specified gas volume fraction can be estimated as

$$n_b = \frac{\phi_g whL}{V_b} \quad (4.13)$$

For a fixed bubble size, the bubbles rearrange to fit within the channel as the gas fraction increases. At low gas fractions, bubbles form a single, uniformly spaced

row of bubbles. This is the structure that we term “dripping”.⁷ The center-to-center distance, or spacing s between bubbles is given by

$$s = \frac{V_b}{\phi_g wh} \quad (4.14)$$

As the volume fraction increases, the spacing decreases.

When the spacing given by Eq. (4.14) is less than the projected diameter or length given by either Eq. (4.2) or (4.6),

$$s \leq D_{projected} \quad (4.15)$$

where $D_{projected}$ equals either D_{sphere} or $D_{pancake}$, the bubbles can no longer form a single row, and they begin to stagger to occupy additional rows, forming the structure that we call “alternating foam”.⁷ The critical volume fraction at which the structure transitions from dripping to alternating foam is obtained by substituting either Eq. (4.2) or (4.6) and Eq. (4.14) into Eq. (4.15) to obtain

$$\phi_{g,da} = \left(\frac{\pi V_b^2}{6 w^3 h^3} \right)^{1/3} \quad (4.16a)$$

for spherical bubbles and

$$\phi_{g,da} = \frac{V_b}{wh^2 \left[\left(\frac{4 V_b}{\pi h^3} + \frac{\pi^2}{16} - \frac{2}{3} \right)^{1/2} + -\frac{\pi}{4} + 1 \right]} \quad (4.16b)$$

for pancake bubbles.

Alternating foam occurs when the number of rows of bubbles is greater than one. The number of rows n is determined by calculating the number of channel lengths L required to fit all the bubbles into one row with the spacing s equal to the projected bubble diameter $D_{projected}$

$$n_r = \frac{n_b D_{projected}}{L} \quad (4.17)$$

If Eq. (4.17) does not yield an integer number, then the number of rows that we would observe is n_r rounded up to the next integer value, or

$$n = ceiling(n_r) \quad (4.18)$$

Eq. (4.18) indicates that any fraction of row between, for example, $1 < n_r \leq 2$ will form two rows of bubbles. The value of the decimal in n is a measure of the spacing of the bubbles in one row, such that a higher decimal value is indicative of a greater number of bubbles and therefore a smaller center-to-center distance between bubbles in one row for a fixed bubble volume. The spacing s can be calculated by combining Eqs. (4.13) and (4.14) and accommodating for a multiple number of rows

$$s = \frac{nL}{n_b} \quad (4.19)$$

As the volume fraction increases, the bubbles will fill up one row and form additional rows as necessary to maintain their circular shape. This will occur whether the bubbles have increased in size or in number. The maximum packing configuration that allows the projected shape of the bubbles to remain circular is a 2D hexagonal close packed structure, illustrated schematically in Fig. 4.4. In this densely packed structure, the center-to-center spacing s in any one row of bubbles is given by

$$s = D_{projected} \quad (4.20)$$

The center-to-center distance between bubbles in adjacent rows is $(\sqrt{3}/2)D_{projected}$ and therefore the total channel width required to accommodate n_r rows of bubbles is given by

$$w_n = D_{projected} \left((n-1) \frac{\sqrt{3}}{2} + 1 \right). \quad (4.21)$$

For a given number of rows, there is a maximum bubble size that can be achieved before the bubble shape must deform to fit within the confines of the channel. The transition between alternating to packed foam occurs when the total width of all bubble rows w_n exceeds the width of the microchannel w

$$w_n \geq w. \quad (4.22)$$

Substituting Eq. (4.21) and either Eq. (4.2) or (4.6) in to Eq. (4.22) and solving for V_b yields the critical bubble volume above which n rows becomes packed,

$$V_n = \frac{\pi}{6} \left[\frac{2}{\sqrt{3}(n-1)+2} \right]^3 w^3, \quad (4.23a)$$

for spherical bubbles and

$$V_n = \pi \frac{h^3 \alpha (10 - 3\pi) + 2wh^2 \left\{ \sqrt{3}(n-1) \left[2wh^2 (10 - 3\pi) + 3(\pi - 4) \right] + 6(\pi - 4) \right\} + 24}{24 \left[\alpha + 4\sqrt{3}(n-1) \right]} \quad (4.23b)$$

for pancake bubbles, where $\alpha = 3n(n-2) + 7$.

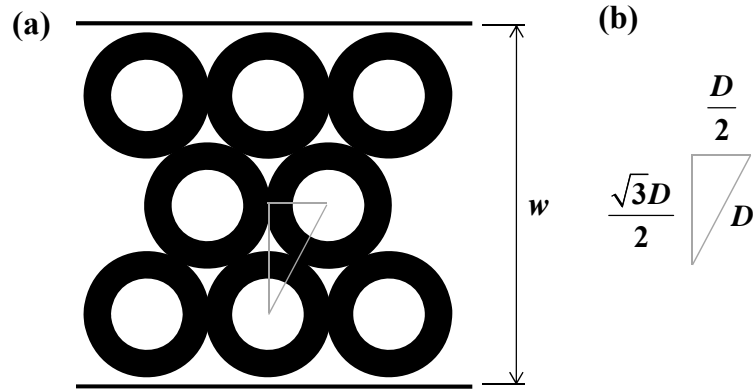


Figure 4.4. Schematic diagram depicting the arrangement of bubbles occupying multiple rows in a two-dimensional hexagonal close packed pattern in a microchannel of width w .

Note that for a given number of rows, the critical volume at which a foam transitions from alternating to packed is independent of volume fraction. However, there is an additional consideration needed to fully describe this transition. The transition is also defined by the maximum number of rows that can physically fit within the width of the microchannel. Substituting Eq. (4.21) into Eq. (4.22) yields the maximum number of rows n_{max} of bubbles with a diameter $D_{projected}$ that can fit in a microchannel with width w .

$$n_{max} = \frac{2(w - D_{projected})}{\sqrt{3}D_{projected}} + 1 \quad (4.24)$$

Fractions of rows are not possible since the presence of a physical boundary would require the bubbles to shift or otherwise deform to fit within the channel walls. Thus, n_{max} is rounded down to the nearest integer value. The critical volume fraction at which the bubble structure transitions from alternating to packed foam occurs when the number of rows required for all the bubbles to fit within the channel exceeds the maximum number of rows given by Eq. (4.24)

$$n \geq n_{\max} \quad (4.25)$$

Combining Eqs. (4.13), (4.18), and (4.20) with Eq. (4.25) yields

$$\frac{\phi_g wh D_{\text{projected}}}{V_b} = n_{\max} \quad (4.26)$$

Substituting in either Eq. (4.2) or (4.6) for $D_{\text{projected}}$ in Eq. (4.26) and solving for ϕ_g yields the critical volume fraction for this transition

$$\phi_{g,ap} = n_{\max} \left(\frac{\pi V_b^2}{6 w^3 h^3} \right)^{1/3}, \quad (4.27a)$$

for spherical bubbles and

$$\phi_{g,ap} = n_{\max} \frac{V_b}{wh^2 \left[\left(\frac{4 V_b}{\pi h^3} + \frac{\pi^2}{16} - \frac{2}{3} \right)^{1/2} - \frac{\pi}{4} + 1 \right]}, \quad (4.27b)$$

for pancake bubbles. Note that Eqs. (4.27) account for multiple rows of bubbles and are the more general forms of Eqs. (4.16), which are only valid for a single row of bubbles.

These transitions also exist for slug bubbles, which are already confined by all four sides of the microchannel. The number of rows n is therefore always equal to one, and the bubbles are already deformed from circular. As such, the slug regime is analogous to the dripping regime, and slugs will transition directly to a single row of packed foam, denoted ‘‘bamboo foam’’. The transition between slugs and a single row of packed foam occurs when the center-to-center spacing s is shorter than the projected length of the slug bubble D_{slug}

$$s \geq D_{\text{slug}}, \quad (4.28)$$

which is essentially the same as Eq. (4.20). Substituting Eq. (4.12) into Eq. (4.28) yields the critical gas fraction at which slugs will transition to bamboo foam,

$$\phi_{g, sb} = \frac{V_b}{V_b + \left(1 - \frac{\pi}{4}\right) \left(w^2 h + \frac{\pi}{2} w h^2\right) + \frac{\pi}{2} \left(\frac{\pi}{4} - \frac{5}{6}\right) h^3}. \quad (4.29)$$

Note that this definition of bamboo foam is slightly different from what is qualitatively observed and named bamboo foam by Raven *et al.*⁷ By our definition, a single row of packed foam is distinguished from bamboo foam. In a single row of packed foam, the projected circular diameter of the bubble can be smaller than the width of the microchannel, while in bamboo foam, this projected diameter must always be larger than the width of the microchannel. These two scenarios are equivalently termed bamboo foam in the literature.⁷ Our definition of bamboo foam typically occurs at larger bubble volumes than what has been previously described qualitatively.

The shape and structural transitions given by Eqs. (4.3), (4.8), (4.16), (4.23), (4.27), and (4.29) can be written in dimensionless form, defining a dimensionless bubble volume by

$$V^* = \frac{V_b}{w^2 h}, \quad (4.30)$$

and defining the channel aspect ratio by

$$\Lambda = \frac{h}{w}. \quad (4.31)$$

The resulting expression for the critical volume at which the spherical to pancake shape transition occurs is given by

$$V_{sp}^* = \frac{\pi}{6} \Lambda^2 \quad (4.32)$$

while the critical volume for the pancake to slug shape transition is described by

$$V_{pb}^* = \frac{\pi}{4} \left(\frac{10-3\pi}{6} \Lambda^2 + \frac{\pi-4}{2} \Lambda + 1 \right) \quad (4.33)$$

Similarly, the critical volume fraction at which the bubble structure transitions from dripping to alternating foam to packed foam is given by

$$\phi_{g,dap} = n_{\max} \left(\frac{\pi V^*}{6 \Lambda} \right)^{1/3}, \quad (4.34a)$$

for spherical bubbles and

$$\phi_{g,dap} = n_{\max} \frac{V^*}{\Lambda \left[\left(\frac{4 V^*}{\pi \Lambda^2} + \frac{\pi^2}{16} - \frac{2}{3} \right)^{1/2} - \frac{\pi}{4} + 1 \right]}, \quad (4.34b)$$

for pancake bubbles. The corresponding volume fraction independent transitions are defined by

$$V_n^* = \frac{\pi}{6} \left[\frac{2}{\sqrt{3}(n_{\max} - 1) + 2} \right]^3 \frac{1}{\Lambda}, \quad (4.35a)$$

for spherical bubbles and

$$V_n^* = \pi \frac{\alpha(10-3\pi)\Lambda^2 + 2 \left\{ \sqrt{3}(n_{\max} - 1) [2\Lambda(10-3\pi) + 3(\pi-4)] + 6(\pi-4) \right\} \Lambda + 24}{24 \left[\alpha + 4\sqrt{3}(n_{\max} - 1) \right]} \quad (4.35b)$$

for pancake bubbles. Finally the critical volume fraction at the transition from slug to bamboo foam can be described by

$$\phi_{g, sb} = \frac{V^*}{V^* + 1 - \frac{\pi}{6} \Lambda^2 + \frac{\pi}{4} \left[\left(\frac{\pi}{2} - 1 \right) \Lambda^2 + \left(2 - \frac{\pi}{2} \right) \Lambda - 1 \right]} \quad (4.36)$$

4.3 Materials and Methods

To validate the geometric arguments outlined in the previous section, we conduct experiments using microfluidic geometries to generate monodisperse bubbles and drops with various volumes and dispersed phase volume fractions. Three microfluidic geometries are used to form bubbles and droplets, (a) flow-focusing, (b) co-flow, and (c) T-junction devices. Each of these nozzle geometries have been described and characterized extensively.⁶ In the flow-focusing and co-flow geometries, the dimensions used are $w_{in} = L_{in} = 200 \mu\text{m}$, $L_{out} = 10 \text{ mm}$, and $w_{out} = \{100, 200, 400, 500, 1000\} \mu\text{m}$. The width of the orifice in the flow-focusing device is $w_{or} = 50 \mu\text{m}$. The dimensions of the T-junctions are such that both arms are approximately the same width and $w = \{100, 500, 1000\} \mu\text{m}$. The depth $h = \{80, 100, 200\} \mu\text{m}$ for all three geometries. The depth and width of each outlet channel are selected to correspond to one of the three aspect ratios considered: $\Lambda = 1, 0.2, \text{ and } 0.1$.

All microfluidic devices are fabricated in poly(dimethylsiloxane) (PDMS) (Dow Sylgard 184) using standard soft lithography fabrication techniques.⁴ The channels are sealed against a thin slab of PDMS to ensure that all four walls exhibit the same wetting characteristics. The dimensions listed above are the

design dimensions. Fabricated in-plane dimensions were measured optically and found to be within 10 μm of the target dimensions. Channel depths were measured using a contact profilometer (Veeco Dektak) and found to be within 5 μm of the target depth. Swelling due to permeation of oil into the PDMS can also change these dimensions slightly and is assumed to change the dimensions by the same multiplicative factor in all directions. As a result, the aspect ratio is assumed to remain constant.

In the case of bubble formation, nitrogen gas is used as the dispersed phased fluid. The continuous phase liquid is de-ionized water containing 1, 5, or 10% w/w Triton X-100 (Sigma Aldrich T8532 – for electrophoresis, used as received), which is a water soluble non-ionic surfactant with a critical micelle concentration of $\text{CMC} = 0.22$ to 0.24 mM (manufacturer specs, Sigma-Aldrich). The presence of dissolved surfactant at such high concentrations is required for stable bubble formation. In the case of droplet formation, the dispersed phase is either pure de-ionized water or a 50/50 glycerol-water mixture. The continuous phase is either light mineral oil (Fisher Scientific) with a viscosity of $\mu = 40$ cP or silicone oil (Fluka) with a viscosity of $\mu = 6$ cP. Oil-soluble surfactant, Span 80 (Sigma Aldrich S6760, used as received), is dissolved in the oil phase at a concentration of either 0.67% or 10% w/w. Because monodisperse bubble and droplet formation is the goal of all the experiments, the exact fluid properties are not of particular interest and the fluids and surfactant concentrations are chosen to yield consistent, stable, monodisperse bubbles and droplets based on previous

experience. Data from previously published work are also compared with the geometric arguments; the details are described elsewhere.²⁵

The two parameters of interest are the droplet or bubble volume and the overall dispersed phase volume fraction. In practice, the fluid flow rates control both of these parameters and V_d and ϕ_d are measured using image analysis of high speed videos. For foams, a two-stage pressure regulator followed by a second electronic pressure regulator (ControlAir, Inc. T550X Miniature EIA) is used to control the nitrogen gas pressure, which varies between 15 and 35 kPa at the exit of the second regulator. Note that the input mass flow rate of gas is not controlled or measured in this experimental setup. Rather, the bubble volume and corresponding volume fraction are measured visually at a given location in the microchannel, as described below. The mass fraction will vary with bubble size since the Laplace pressure within a bubble increases with decreasing bubble size. For emulsions, the volumetric flow rates of the water and oil phases are controlled by separate syringe pumps (Harvard Apparatus PHD2000) and vary between 0.05 and 300 $\mu\text{L min}^{-1}$. All experiments are allowed to achieve steady state flow conditions for at least 15 minutes before images are recorded.

Bubble and droplet formation is visualized using an inverted microscope (Nikon TE2000U or Ti-U) with an attached high-speed camera (IDT XS5, Redlake or Phantom v9.1, Adept Turnkey Pty, Ltd.). Videos of the droplet or bubble formation process in addition to the downstream structure are captured digitally and individual images are analyzed using ImageJ (NIH 1.43u). If the shape is approximately circular, the measured diameter is compared with the

known channel depth. If the diameter exceeds the channel depth, the volume is determined assuming the shape is a pancake (Eq. (4.6)). If not, the volume is determined assuming the shape is a sphere or droplet. The measured volume fraction is obtained by taking the ratio of the total bubble volume and the total channel volume of interest. The total bubble volume is determined by multiplying the volume of one bubble or droplet by the number of droplets observed in a section of the microchannel. The total channel section volume is obtained by measuring the length of that section of the channel and multiplying it by the measured width and depth of the channel. Swelling effects are taken into account in the calculated total channel section volume. The foam or emulsion structure for a given experiment is determined by counting the number of rows, measuring the droplet or bubble spacing, and observing whether the shape is distorted by proximity to neighboring objects (i.e. another bubble or droplet, or the channel walls). To determine the difference between alternating and packed foam, the ellipticity of the interface is estimated using image analysis. An ellipticity value ε close to 1.0 ($\varepsilon > 0.8$) is considered circular and values below $\varepsilon \leq 0.8$ are considered sufficient deviation from circular to denote the structure as packed.

4.4 Results

The dimensionless equations (4.30)-(4.36) can be used to generate a regime map categorizing the bubble shapes and structures expected as a function of dimensionless bubble volume V_b^* and gas fraction ϕ_g for a fixed channel aspect ratio Λ . The geometric arguments outlined here result in transitions that depend

only on bubble size, gas volume fraction, and channel geometry. Therefore, the criteria should apply to any dispersed phase fluid, including liquid droplets dispersed in an immiscible liquid. To generalize Eqs. (4.30)-(4.36), the bubble volume V_b^* is replaced with the dispersed phase volume V_d^* and the gas volume fraction ϕ_g is replaced with the dispersed phase volume fraction ϕ_d . Similarly, the predicted transitions are independent of the nozzle shape or method of formation of the drops or bubbles prior to entering the channel. A typical regime map corresponding to an aspect ratio of $\Lambda = 0.2$ using these renamed variables is shown in Fig. 4.5. The figure is plotted on a log-log scale where the horizontal axis is the dimensionless bubble or droplet volume V^* , and the vertical axis is the dispersed phase volume fraction ϕ_d . Both axes span several orders of magnitude but have a physical lower limit of zero, which corresponds to a pure medium. The bubble or droplet volume has no numerical upper limit, as the bubble volume can be much larger than the unit volume w^2h of channel. However, the upper limit of the volume fraction ϕ_d is unity because the dispersed phase volume cannot be greater than the total volume.

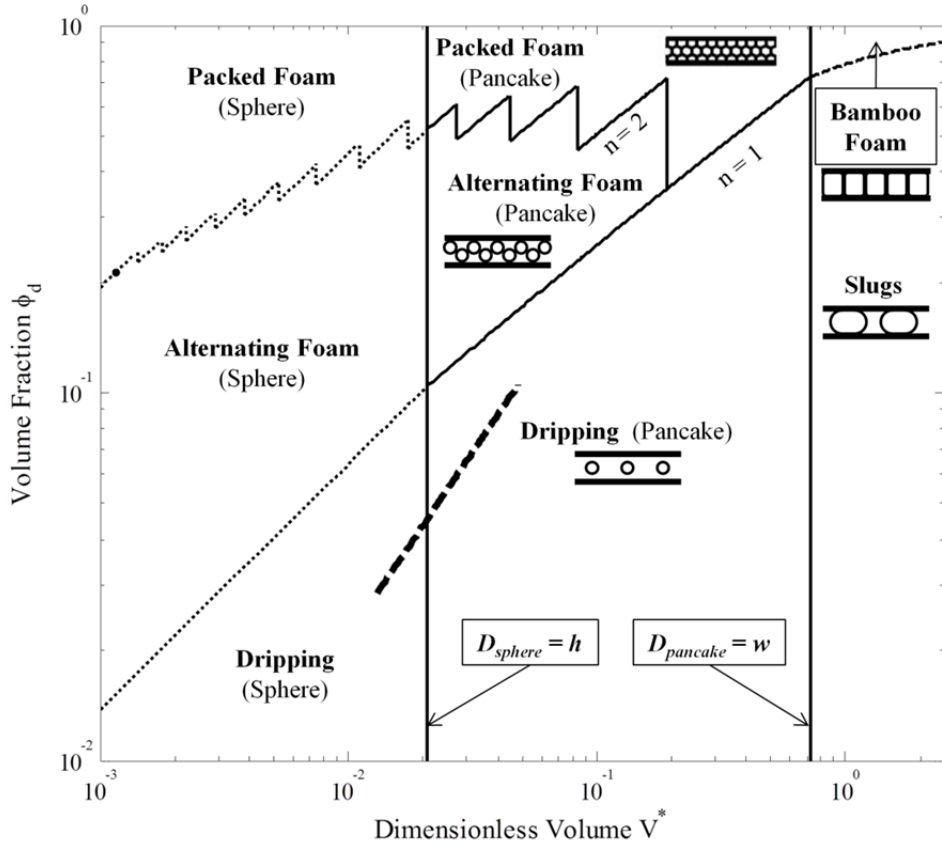


Figure 4.5. Predicted regime map of bubble shapes and structures in a rectangular microchannel with $\Lambda = 0.2$.

In Fig. 4.5, the lines represent the critical conditions for each transition given by Eqs. (4.30)-(4.36). Each region of operating space is labeled with the corresponding shape and structure. The critical dimensionless bubble volumes are the solid vertical lines that divide the regime map into three bubble shape regions corresponding to spheres, pancakes, and slugs in order of increasing volume. For this aspect ratio, the critical dimensionless bubble volume defining the expected transition from spherical to pancake bubbles is $V_{sp}^* = 0.02$, which is indicated by the left most vertical line on the figure. Similarly, $V_{ps}^* = 0.72$ is the critical volume defining the expected transition from pancake to slug bubbles. The critical bubble volume fractions that divide each shape region into smaller regions

defining the structure are functions of the dimensionless bubble volume and the channel dimensions. The transitions pertaining to spheres are shown as dotted lines, those corresponding to the pancakes are shown as solid lines, and the single structure transition for the slug bubbles is shown as a dashed line. In order of increasing volume fraction, the regions correspond to dripping, alternating, and packed foam for sphere and pancake shapes, and slugs and bamboo foam for slug shapes. Furthermore, the alternating to packed foam transition appears as a sawtooth line for each integer jump in the maximum number of rows. The sawtooth pattern reflects the two components of the transition; one that depends only on the bubble volume (vertical lines), and one that depends on both bubble volume and volume fraction (slanted lines).

The operating space described here depends purely on the local bubble volume and volume fraction at a given position along the length of a microchannel. However, in a pressure-driven microchannel flow, there is a linear pressure decrease along the length of the channel. This implies that the volume of a bubble containing compressible gas will increase along the length of the channel, which will in turn change both the volume fraction and the resulting foam structure. Since the pressure drop along a microchannel depends on flow rate and flow resistance of the foam within a channel, the volume-volume fraction trajectory followed by a given bubble depends on the flow rate and the foam structure, which can significantly influence the flow resistance. To illustrate the concept, we consider small, spherical bubbles in which the bubbles themselves do not contribute significantly to the flow resistance in the channel. Assuming that

the bubbles contain an ideal gas, and that the flow resistance arises from a Hagen-Poiseuille-like relationship for a Newtonian fluid in a rectangular channel, the changes in bubble volume and gas volume fraction along the channel can be estimated. The dashed line shown in Fig. 4.5 shows an example of a volume-volume fraction trajectory for a spherical bubbly structure that starts in the dripping mode and travels along a one meter length of microchannel. Note that the length over which this trajectory is estimated is longer than the typical length of a microchannel, and that the bubble volume changes by less than 3% over a typical microchannel length (10 mm). However, once the bubble volume and volume fraction are large enough to contribute to the flow resistance, the calculation of the changes in volume and volume fraction along the channel becomes more complicated.^{26,27} Droplets are generally considered incompressible and therefore would not exhibit a volume change arising from the pressure drop in the channel.

Eqs. (4.30)-(4.36) are applicable to any pair of immiscible fluids and any nozzle type, which is reflected in the chosen experimental systems. To compare with the geometric transitions predicted in Fig. 4.5, we determine the volumes and volume fractions for a wide range of emulsions and foams generated using flow-focusing and co-flow microfluidic devices with downstream aspect ratios equal to $\Lambda = 0.2$. Nitrogen bubbles in water containing dissolved Triton X-100 comprise the foams that are studied. The emulsions consist of deionized water drops in a continuous phase of mineral oil containing dissolved Span 80. The bubbles and droplets generated are monodisperse and stable during the time the

bubbles or droplets travel the length of the channel (1-10 seconds). For each bubble volume and volume fraction achieved in experiments, the bubble shape and structure is determined using the image analysis protocols outlined in the previous section. The results are shown in Fig. 4.6 along with the same predicted transitions shown in Fig. 4.5. The three data points lying between $10^{-3} < V^* < 10^{-2}$ at the dripping to alternating foam transition line are included from Case B of Ref. (25), which corresponds to drops of water with dissolved octaethylene glycol monododecyl ether ($C_{12}E_8$) surfactant in light mineral oil, as described in Materials and Methods.²⁵

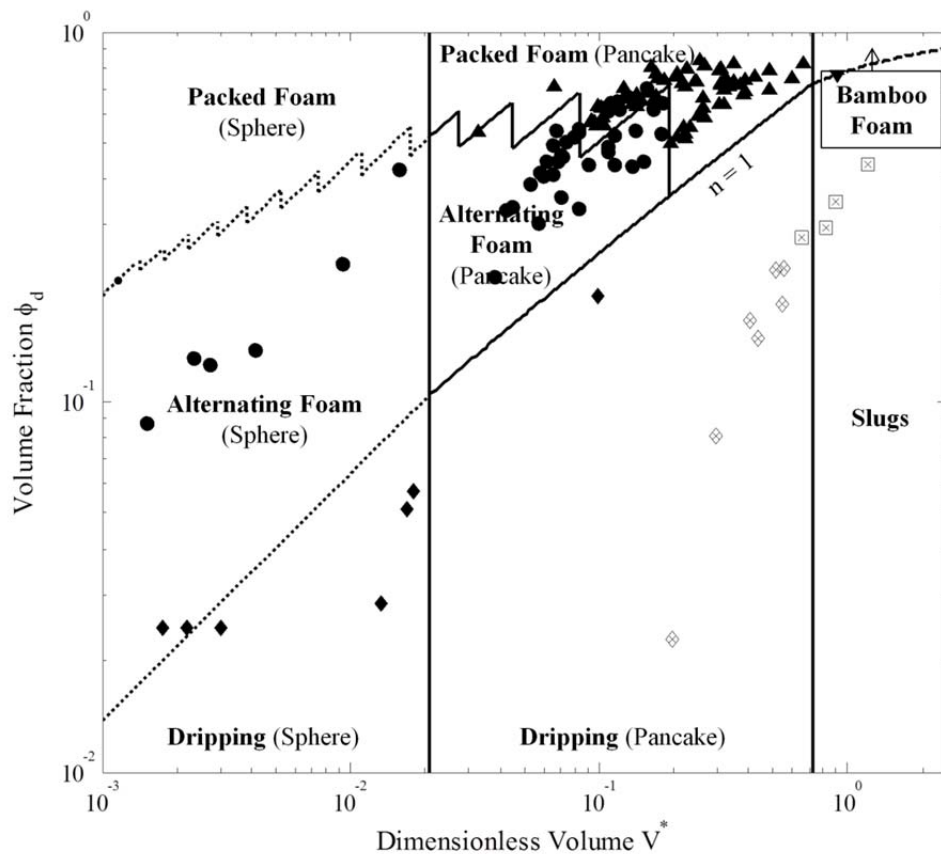


Figure 4.6. Regime map of observed and predicted dispersed phase shapes and structures in a rectangular microchannel ($\Lambda = 0.2$). Symbol fill indicates the nozzle type: filled symbols – flow-focusing, open symbols - T-junction, and x-filled symbols - co-flow. Symbol shapes indicate structure: (\diamond) dripping, (\square) slugs, (\circ) alternating foam, (Δ) packed foam, and (∇) bamboo foam.

In Fig. 4.6, there are two symbol fills to represent the two nozzle types used to generate the foams and emulsions for this aspect ratio: filled symbols represent flow-focusing data and x-filled symbols represent co-flow data. The regimes that are represented experimentally include dripping (\diamond) for both spheres and pancakes, slugs (\square), alternating foam (\circ) for both spheres and pancakes, packed foam (Δ) for pancakes, and bamboo foam (∇). The same symbols are used to represent the structures for spheres and pancakes because we could not experimentally observe this shape transition in the top-down view of the microscope. We assume that the bubbles are pancake-shaped if the diameter is greater than the channel depth. The only regime not represented experimentally for the aspect ratio $\Lambda = 0.2$ is the packed foam structure consisting of spherical bubbles. Attempts to reach this region of the regime map experimentally result in either no bubble or droplet break-up or larger bubbles and droplets.

Fig. 4.6 indicates that for most experimental conditions, the bubble shape and foam structure observed for a given bubble volume and volume fraction is the same as that predicted by the geometric arguments of Eq. (4.30)-(4.36) for an aspect ratio $\Lambda = 0.2$. Again, the sphere to pancake transition was not experimentally observable, so we have not verified this shape transition. The pancake to slug shape transition, however, is easily visualized with our experimental setup. There is good agreement with the model in cases where the bubble volumes are not near the critical volume for a shape transition, as seen by experimental data symbols lying within the corresponding shape region of the regime map. Near the critical bubble volume, $V_{ps}^* = 0.72$, there is one inconsistent

data point where the shape is predicted to be a pancake bubble, but is categorized as a slug bubble (\square).

The structure transitions are similarly easy to visualize as they occur. Away from the transition lines, there is again good agreement between the predicted and observed foam structures. There are a few discrepancies near the predicted transitions. At the dripping to alternating transition for spheres, there are two data points that exhibit a dripping structure (\diamond) but are expected to form an alternating foam. At the alternating to packed foam transition at $n = 2$ rows for pancakes, there are several data points that are observed to exhibit an alternating foam structure (\circ) but are expected to form a packed foam instead.

The geometric arguments suggest that the bubble shape and foam structure regimes depend on channel aspect ratio. For example, the critical dimensionless bubble volume for the transition from spherical to pancake bubbles occurs at $V_{sp}^* = 0.005$ for an aspect ratio $\Lambda = 0.1$, which is significantly smaller than the same transition for the aspect ratio $\Lambda = 0.2$. The pancake to slug transition occurs at $V_{ps}^* = 0.75$ for $\Lambda = 0.1$, which is slightly larger than the same transition for $\Lambda = 0.2$. Thus, the region of parameter space in which we expect to observe pancake-shaped bubbles grows wider as the aspect ratio decreases. All expected structure transitions are still present in the reduced aspect ratio case but have shifted from those presented in Figs. 4.5 and 4.6 for $\Lambda = 0.2$. The transitions from dripping to alternating foam, alternating to packed foam, and slug to bamboo foam occur at increasing volume fractions for a fixed volume as the aspect ratio decreases. A distinct difference between the aspect ratios $\Lambda = 0.2$ and $\Lambda = 0.1$ is

the increase in the number of rows of pancake bubbles that can be accommodated across the microchannel before they become distorted. The limits on the axes of the phase diagram remain the same as before. The predicted shape and structure transitions are shown for $\Lambda = 0.1$ in Fig. 4.7.

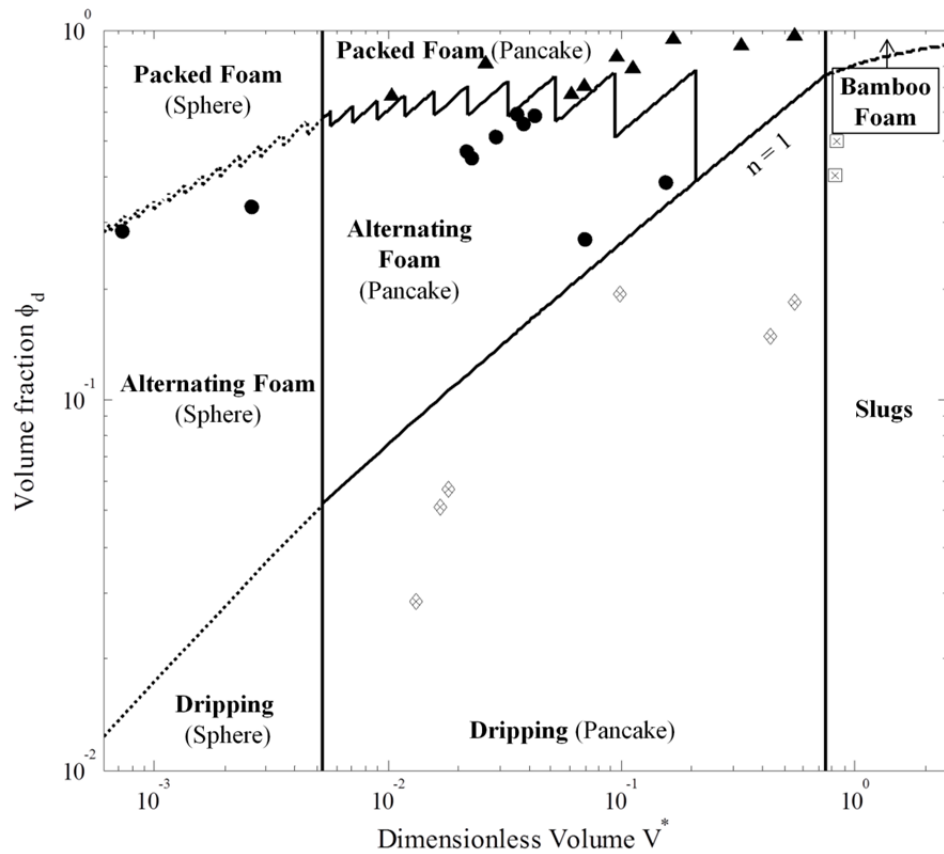


Figure 4.7. Regime map of observed and predicted dispersed phase shapes and structures in a rectangular microchannel ($\Lambda = 0.1$). Symbol fill indicates the nozzle type: filled symbols – flow-focusing, open symbols - T-junction, and x-filled symbols - co-flow. Symbol shapes indicate structure: (\diamond) dripping, (\square) slugs, (\circ) alternating foam, (Δ) packed foam, and (∇) bamboo foam.

We conducted experiments using flow-focusing and co-flow nozzles to generate emulsion drops in channels with aspect ratio $\Lambda = 0.1$. The emulsions consisted of deionized water droplets in mineral oil containing 10% w/w Span 80. Using the same symbols shown in Fig. 4.6, the bubble and droplet shapes that are represented experimentally include all three shapes, while the structure regimes

represented include pancake dripping (\diamond), slugs (\square), alternating foam (\circ) for both spheres and pancakes, and pancake packed foam (Δ). The regions that are not experimentally observed are dripping and packed foams of spheres and bamboo foam. Bubble and droplet formation is experimentally unstable in these regions and did not generate stable monodisperse bubbles or droplets. For the shape and structure regions that are experimentally represented, the data shows good agreement with predicted regimes. The observed emulsion and foam structures match the expected shapes and structures for the corresponding volume and volume fraction, even near the critical dimensionless bubble volumes and volume fractions.

For an aspect ratio of $\Lambda = 1$, the channel cross-section is square, implying that the droplet or bubble shape will transition directly from spheres to slugs, which is reflected in the collapse of the pancake region observed in Fig. 4.8. As such, the one vertical line in this figure at a dimensionless bubble volume $V_{sp}^* = V_{ps}^* = 0.52$ represents the predicted critical volume where the sphere to slug shape transition will occur. All of the bubble structures are still present in the predicted regime map, with the exception of those associated with the pancake region. Another distinct difference between the previous two regime maps ($\Lambda = 0.2$ and 0.1) and this one ($\Lambda = 1$) is the presence of a single row packed foam regime at smaller spherical bubble volumes to the left of the transition to bamboo foam at larger bubble volumes, which is present only in the pancake-shaped packed foam regime at lower aspect ratios. The limits of the axes otherwise remain the same. The square cross-section is an important physical limit of the

microchannel geometry. The depth of the channel can exceed the width, but the two parameters could then be interchanged and the same transitions would still apply. The square microchannel ($\Lambda = 1$) is therefore the upper limit of the aspect ratio on the geometric model and yields a distinctly different phase diagram compared with aspect ratios less than unity.

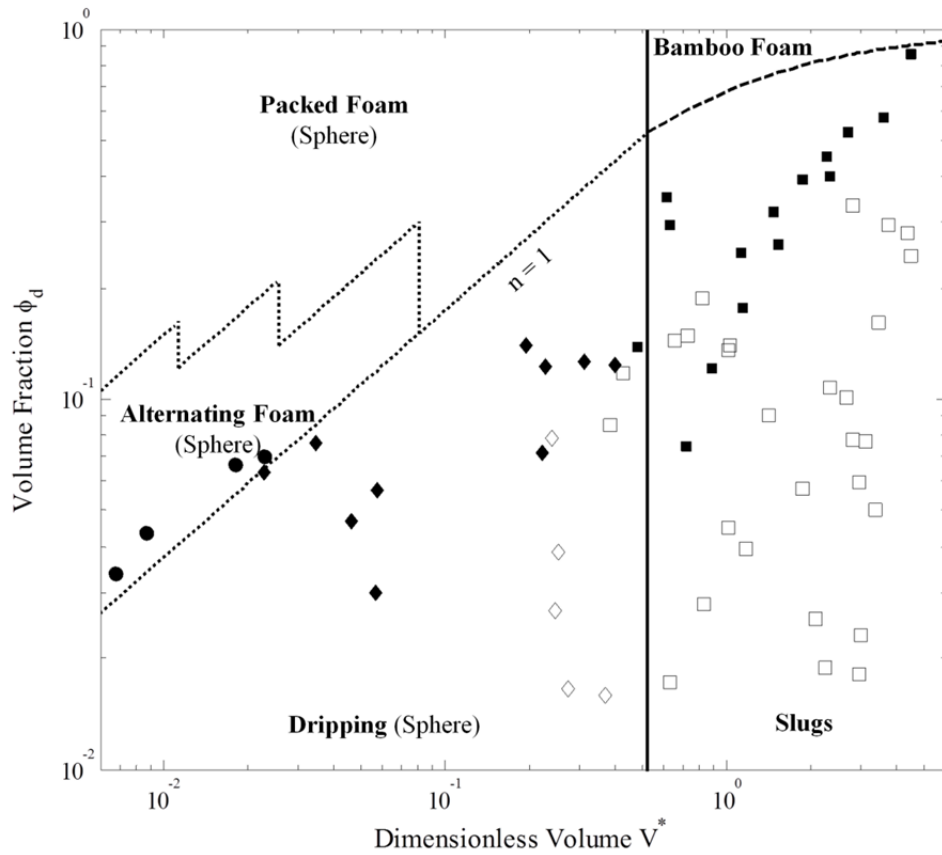


Figure 4.8. Regime map of observed and predicted dispersed phase shapes and structures in a rectangular microchannel ($\Lambda = 1$). Symbol fill indicates the nozzle type: filled symbols – flow-focusing, open symbols - T-junction, and x-filled symbols - co-flow. Symbol shapes indicate structure: (\diamond) dripping, (\square) slugs, (\circ) alternating foam, (Δ) packed foam, and (∇) bamboo foam.

The shape and structure transitions plotted in Fig. 4.8 are experimentally verified using flow-focusing and T-junction nozzles to generate water-in-oil emulsions. Here, flow-focusing data continue to be represented by the filled symbols and the T-junction data are represented by open symbols. For the flow-

focusing experiments, the emulsions are comprised of deionized water in mineral oil containing 10% w/w Span 80. The droplets generated in T-junctions contain either deionized water or glycerol-water (50/50) solutions in a continuous phase of mineral oil or silicone oil. Experiments with and without 0.67% Span 80 in the oil phase are also carried out in the latter nozzle design. Using these experimental conditions, data is obtained in the dripping (\diamond), slugs (\square), and alternating foam (\circ) regimes for the aspect ratio $\Lambda = 1$. Data could not be obtained for packed foams with spherical inclusions or for bamboo foam due to either unstable bubble or droplet break-up or none at all.

Comparison of the geometric model and the experimental data for an aspect ratio of $\Lambda = 1$ (Fig. 4.8) shows that the observed shapes and structures that reside away from the transition lines match the predictions for the corresponding volumes and volume fractions. At the sphere to slug transition, there are three data points (one from a flow-focusing nozzle and two from a T-junction nozzle) that have been characterized as slugs but lie in the sphere region. The available data for dripping and alternating foams correspond well to the expected structures.

4.5 Discussion

The geometric model described in Section 4.2 predicts that the bubble shape and structure of a foam confined within a rectangular microchannel will vary with the microchannel aspect ratio. This dependence is confirmed in Figs. 4.6-4.8. As the aspect ratio increases up to unity, the region containing pancake-shaped bubbles decreases in breadth until it completely disappears for a

square microchannel. The critical volume fractions defining the structure transitions decrease for a given bubble volume as the aspect ratio increases, but all structures are observed for each aspect ratio. The experimental data and predicted regime maps presented in Figs. 4.6-4.8 agree relatively well for both bubbles and droplets generated using three nozzle types for the microchannel aspect ratios ($\Lambda = 0.1, 0.2,$ and 1) studied here. More specifically, the geometric model predicts the shape and structure of the bubbles and droplets reasonably well for observed bubble volumes and volume fractions away from the critical values that indicate a transition between shapes or structures for all three aspect ratios discussed here. We observed a few discrepancies between the model and experiments in two of the aspect ratios ($\Lambda = 0.2$ and 1) near the pancake-to-slug (sphere-to-slug for $\Lambda = 1$) shape transition and at both the dripping to alternating foam and the alternating to packed foam structure transitions. The discrepancies between the model and the experimental data for these aspect ratios (Figs. 4.6 and 4.8) indicate that there are additional aspects of the physical systems that have not been taken into account.

The experimental procedure used to make comparisons with the geometric model has several limitations. For example, a cross-sectional view of the microchannel is not imaged, so the actual depth of the microchannel is unknown and the experimental critical volume at which a bubble or droplet deforms from a sphere to a pancake shape cannot be detected. This also affects the reported value of the dimensionless bubble volume, which requires knowledge of the actual microchannel dimensions. Since we do not know the local channel depth, we

assume that the contact profilometer measurement provides an accurate average depth value for the microchannel. In addition, the model of the pancake shape, which currently assumes that the shape is a cylinder with a semi-circular endcap, is approximate and cannot be verified without a cross-sectional view of the channel. In general, error in the assumed shape contributes to the error in the reported bubble volume.

Another potential source of error arises from low image quality when capturing the bubble or droplet formation. Insufficient frame rates and low image contrast can cause difficulty with subsequent image analysis. For example, frame rates that are too slow to resolve the motion of the bubble or droplet along the channel produce blurry images, while insufficient image contrast leads to poor threshold limits for conducting edge detection analysis. Both of these issues affect the accuracy of bubble volume and ellipticity calculations. In the experiments corresponding to the alternating to packed foam structure transition in the pancake region for the aspect ratio $\Lambda = 0.2$ (Fig. 4.6), low image quality made it difficult to determine the ellipticity of the bubbles using digital image analysis. Instead, we visually estimate when deformation of the bubble interface was significant enough between alternating and packed foam for the bubble structure. Low image quality is likely the primary reason for blurring of the boundary between these two regions for experiments at $\Lambda = 0.2$.

Overall, the accuracy of the geometric model is surprisingly good given its simplicity. However, it does not describe all experimental conditions. For example, we assume that the foam is static even though flow is used to generate

the bubbles and droplets and the structures are typically still moving when imaged. In reality, the short length of channel (10 mm) coupled with the rapid formation and flow of the surfactant-stabilized structure along the length of the microchannel (residence times ≈ 1 second) does not allow for significant volume or structure change in the imaging time. We assume the observed structures are equivalent to the static counterpart for the same bubble volume and volume fraction. For emulsions, the input volumetric flow rates and the image analysis provide independent measures of the volume fraction. For foams, the volume fraction is obtained solely from image analysis since gas is input through a constant pressure source and the input mass flow rate is not controlled or measured. In both cases, we use the visually measured volume fraction rather than the input volumetric flow rate fraction since the two are not necessarily equal during flow, even in the case of (incompressible) emulsions. This assumption works well for cases that are not too close to transitions. However, the flow can distort the shape away from the circular shape that we assume. Flow-induced distortion is particularly evident in experiments observed near the pancake to slug shape transition. Pancake-shaped bubbles will adopt a distorted shape even before the volume is large enough to be deformed by the channel walls. A variety of possible bubble and drop shapes induced by pressure driven flow in capillaries have been reviewed by Olbricht and calculated asymptotically by Nadim and Stone.^{15,28} Garstecki and Whitesides have also commented on the effect of flow on the shape and structure that a foam will subsequently adopt.^{20,21} The deformation of the bubble or droplet shape can also change as the foam or

emulsion flows down the channel, which allows time for the inclusions to rearrange and find a lower energy state. Additional information on the specific shapes of the bubbles that comprise a dry foam can be found elsewhere.²⁹ Shape distortion by flow can induce error in the measured bubble volume and volume fraction as well as in the classification of the structure.

We assume that the fluid properties do not influence the bubble or droplet shape or the subsequent structure. This, along with the previously discussed static assumption, results in the absence of a capillary number dependence in this model. However, the fluid property that will influence the shape the most is the interfacial tension, which will affect the curvature of the interface as the bubble or drop conforms to the rectangular corners of the channel.^{23,24} Since a change in curvatures along the corners of the bubble amounts to a shape change, this variation will also contribute to uncertainty in the measured volume.

The presence of a high concentration of surfactant above the critical micelle concentration ensures monodisperse bubbles and droplets that are stable against coalescence in the microchannel, which meets several key criteria of the model. We consider only small molecule surface active species in this study, which can easily adsorb and desorb at the interface to allow the bubble or droplet shape to relax to a circular interface.^{30,31} We do not consider more complex adsorbing species, such as proteins and particles that may not allow the shape to fully relax.³²

We also do not address structures formed by polydisperse foams and emulsions even though these can be produced at some conditions in microfluidic

nozzles. For example, Raven *et al.*⁷ described production of a bidisperse foam structure, and Garstecki *et al.*^{33,34} reported on oscillations and instabilities associated with bubble formation at certain experimental flow conditions. While we observe these phenomena, the analysis of such cases is outside the scope of this paper. In some cases, very small satellite droplets are formed. These are neglected assuming that they do not significantly affect the calculated bubble volumes and volume fractions.^{35,36}

In microfluidic bubble and droplet generation, each type of nozzle operates using a different mode of break-up: flow-focusing and co-flow devices use the elongation of the dispersed phase stream to induce break-up,^{12,37} while droplets are formed by shear flow in T-junctions.^{38,39} The different modes of break-up lead to different ranges of accessible bubble volumes and volume fractions as shown in the regime maps of Figs. 4.6-4.8. The flow-focusing devices produce smaller bubble volumes for a given volume fraction (see $0.02 \leq \phi_d \leq 0.2$ for Fig. 4.6 or $\phi_d \sim 0.2$ for Fig. 4.7) and larger volume fractions for a given bubble volume ($0.1 \leq V^* \leq 1$ for Fig. 6 and $0.01 \leq V^* \leq 1$ for Fig. 4.7) compared with co-flow devices. A similar comparison is made between flow-focusing devices and T-junction devices ($0.07 \leq \phi_d \leq 0.2$ for a set volume and $0.1 \leq V^* \leq 5$ for a fixed volume fraction) in Fig. 4.8. Co-flow and T-junction nozzles generate similar sized bubbles and droplets, but T-junctions are able to generate structures with lower volume fractions. However, varying the nozzle type still could not produce experimental data for all of the regimes predicted by the geometric model. Experiments at conditions expected to yield spherical packed foam and bamboo

foam structures resulted in either no break-up of the dispersed phase flow or the formation of large bubbles or droplets rather than increased numbers of smaller bubbles or droplets. This can be attributed to the larger mechanical stresses needed to overcome large Laplace pressures inside smaller bubbles.⁴⁰ At the high speeds needed to achieve larger mechanical stresses, there is also less time for surfactants to adsorb to and stabilize the interface, so the interfacial tension is larger and the break-up of the dispersed phase into smaller droplets is less likely.²⁵

Finally, we have already considered the limit of the geometric model that occurs when the depth and width of the channel are equal (Fig. 4.8). At the other extreme, we can consider an infinitely wide channel ($\Lambda \rightarrow 0$). In direct contrast to the case of $\Lambda = 1$, in which the pancake regime collapses, the pancake region in this case will have no upper bound and the slug and bamboo foam regions will effectively disappear. In this limiting case, the structure cannot become packed for either sphere or pancake shapes because there is no maximum number of rows, so the packed foam regions will also disappear when $\Lambda \rightarrow 0$. In summary, an infinitely wide channel will yield only spheres and pancakes in dripping and alternating structures, and the critical dimensionless volume defining the transition between shapes will approach $V^* \rightarrow 0$ as $\Lambda \rightarrow 0$.

We have outlined some limitations and key criteria for the present model and experimental setup and we observe that a single microfluidic nozzle design cannot access certain regions of the operating diagram, specifically the packed and bamboo foam regions. However, future modifications to the experimental setup can be considered to access these regimes. For example, a method by which

continuous fluid can be removed would allow the dispersed phase volume fraction to increase within the outlet channel. This can be accomplished by including an additional side channel.⁴¹ Alternatively, the foam or emulsion could be compressed such that the effective length of the channel decreases by forcing the excess liquid out of the channel and causing the inclusions to deform and rearrange as necessary.¹⁹ The bubble or droplet volume can also be controlled by the introduction of an automated system that would allow for a greater accessible range of bubble and droplet sizes, such as one that incorporates external valves.⁴²

4.6 Conclusions

We have developed a geometric model for the shape and structure of a foam or emulsion confined within a rectangular microchannel. The critical volumes and volume fractions at which the transitions between bubble shapes (sphere, pancake, or slug) and structures (dripping, slug, alternating foam, packed foam, or bamboo foam) occur are described and used to generate operating diagrams for three downstream microchannel aspect ratios. Experiments agree reasonably well with the geometric model indicating that the underlying simplifying assumptions are valid over a relatively wide range of conditions. Bubble and droplet data from flow-focusing, T-junction, and co-flow devices were used to compare the geometric model with experimental results. The most significant shortfall of the geometric arguments is the lack of accounting for flow effects. Flow effects most strongly influence the highly confined shapes and highly packed structures, and the effect is that the boundaries between regimes are

blurred. These results, particularly the predicted transition conditions outline in Eqs. (4.30) through (4.36), lead to a set of design criteria that can be used as a starting point for generating desired foam or emulsion structures for many applications.

4.7 References

1. K.-Y. Chung, N. C. Mishra, C.-C. Wang, F.-H. Lin and K.-H. Lin, *Biomicrofluidics* **3**, 022403 (2009).
2. M. Devaud, T. Hocquet and V. Leroy, *Eur. Phys. J. E* **32**, 13 (2010).
3. A. C. Hatch, J. S. Fisher, S. L. Pentoney, D. L. Yang and A. P. Lee, *Lab on a Chip* **11**, 2509 (2011).
4. G. M. Whitesides and A. D. Stroock, *Physics Today* **54**, 42 (2001).
5. A. M. Gañán-Calvo and J. M. Gordillo, *Physical Review Letters* **87**, 274501 (2001).
6. G. F. Christopher and S. L. Anna, *Journal of Physics D: Applied Physics* **40**, R319 (2007).
7. J. P. Raven, P. Marmottant and F. Graner, *European Physical Journal B* **51**, 137 (2006).
8. D. Weaire, S. Hutzler, W. Drenckhan, A. Saugey and S. Cox, edited by W. Richtering (Springer Berlin / Heidelberg, 2006), Vol. 133, pp. 100.
9. J. I. Park, E. Tumarkin and E. Kumacheva, *Macromolecular Rapid Communications* **31**, 222 (2010).
10. A. S. Utada, E. Lorenceau, D. R. Link, P. D. Kaplan, H. A. Stone and D. A. Weitz, *Science* **308**, 537 (2005).
11. B. P. Binks and T. S. Horozov, *Colloidal Particles at Liquid Interfaces*. (Cambridge University Press, 2006).
12. P. Garstecki, I. Gitlin, W. Diluzio, G. M. Whitesides, E. Kumacheva and H. A. Stone, *Applied Physics Letters* **85**, 2649 (2004).
13. E. B. Matzke, *Am J Bot* **33**, 58 (1946).
14. W. Drenckhan and D. Langevin, *Current Opinion in Colloid and Interface Science* **15**, 341 (2010).
15. W. L. Olbricht, *Annual Review of Fluid Mechanics* **28**, 187 (1996).
16. E. Kumacheva, P. Garstecki, H. K. Wu and G. M. Whitesides, *Physical Review Letters* **91** (2003).
17. S. Yang, S. Ahn, A. Kang, D. Lee, S. Lee, J. Kim, K. Ahn and S. Lee, *Korea-Australia Rheology Journal* **23**, 119 (2011).
18. P. Pieranski, L. Strzelecki and B. Pansu, *Physical Review Letters* **50**, 900 (1983).
19. J.-B. Fleury, O. Claussen, S. Herminghaus, M. Brinkmann and R. Seemann, *Applied Physics Letters* **99**, 244104 (2011).
20. P. Garstecki and G. M. Whitesides, *Physical Review E* **73** (2006).
21. P. Garstecki and G. M. Whitesides, *Physical Review Letters* **97** (2006).
22. See supplementary material at [URL will be inserted by AIP] for a more detailed description of the geometric model for the foam structure.
23. H. Wong, C. J. Radke and S. Morris, *Journal of Fluid Mechanics* **292**, 71 (1995).
24. H. Wong, C. J. Radke and S. Morris, *Journal of Fluid Mechanics* **292**, 95 (1995).

25. W. Lee, L. M. Walker and S. L. Anna, *Physics of Fluids* **21**, 032103 (2009).
26. T. Cubaud and C. M. Ho, *Physics of Fluids* **16**, 4575 (2004).
27. M. J. Fuerstman, A. Lai, M. E. Thurlow, S. S. Shevkoplyas, H. A. Stone and G. M. Whitesides, *Lab on a Chip* **7**, 1479 (2007).
28. A. Nadim and H. A. Stone, *Stud Appl Math* **85**, 53 (1991).
29. D. Weaire and S. Hutzler, *The physics of foams*. (Oxford University Press, 2001).
30. J. Eastoe and J. S. Dalton, *Advances in Colloid and Interface Science* **85**, 103 (2000).
31. R. Pan, J. Green and C. Maldarelli, *Journal of Colloid and Interface Science* **205**, 213 (1998).
32. M. Abkarian, A. B. Subramaniam, S.-H. Kim, R. J. Larsen, S.-M. Yang and H. A. Stone, *Physical Review Letters* **99**, 188301 (2007).
33. P. Garstecki, M. J. Fuerstman and G. M. Whitesides, *Nature Physics* **1**, 168 (2005).
34. P. Garstecki, M. J. Fuerstman and G. M. Whitesides, *Physical Review Letters* **94** (2005).
35. S. L. Anna, N. Bontoux and H. A. Stone, *Applied Physics Letters* **82**, 364 (2003).
36. Y.-C. Tan, V. Cristini and A. P. Lee, *Sensors and Actuators B: Chemical* **114**, 350 (2006).
37. R. Q. Xiong, M. Bai and J. N. Chung, *J Micromech Microeng* **17**, 1002 (2007).
38. P. Garstecki, M. J. Fuerstman, H. A. Stone and G. M. Whitesides, *Lab on a Chip* **6**, 437 (2006).
39. T. Thorsen, R. W. Roberts, F. H. Arnold and S. R. Quake, *Physical Review Letters* **86**, 4163 (2001).
40. P. C. Hiemenz and R. Rajagopalan, *Principles of colloid and surface chemistry*, 3rd ed. (Marcel Dekker, New York, 1997).
41. K. Jiang, C. Xue, C. Arya, C. Shao, E. O. George, D. L. Devoe and S. R. Raghavan, *Small* **7**, 2470 (2011).
42. J. Guzowski, P. M. Korczyk, S. Jakiela and P. Garstecki, *Lab on a Chip* **11**, 3593 (2011).

Chapter 5. Controlled Dehydration of Nanoliter Droplets Stored in a Microfluidic Device

5.1 Introduction

Monodisperse bubbles and droplets have applications in the food, personal care, and paint industries as foams and emulsions where the contents of each phase can be precisely tuned. Droplets within an emulsion can be viewed as individual microreactors, which is useful in applications requiring numerous studies to be performed with a limited amount of cost-prohibitive test material. Examples include pharmaceutical drug discovery and explosives development, where large scale experiments are potentially dangerous.¹⁻⁴

Depending on the application, droplets containing the reactants or chemical species of interest may need to be further manipulated. Previous work has focused on design criteria governing precise droplet generation and many other useful droplet-based operations, such as coalescence, mixing, storage, dehydration, and detection.^{1,5,6} In the previous chapter, a geometric model was developed to predict the droplet shape and packing structure for a given bubble/droplet volume and volume fraction. In that study, droplet generation occurred as a steady state process, and it was shown that the geometric model could accurately predict the shape and structure of the emulsion without consideration of the upstream channel geometry or the flow conditions. However, flow conditions may become important depending on the application. In a typical microfluidic device, droplets are generated at rates of 1-1000 droplets/second with

volumes of 100 pL to 1000 nL with polydispersity less than 3%. Taking into account that droplets are typically formed at flow rates between 1 and 100 $\mu\text{L}/\text{min}$ and the outlet length of a microchannel is between 10 and 100 mm, the residence time of a droplet within the microfluidic device is between 1 ms and 100 s.⁷ In comparison, processes such as protein crystallization, colloidal aggregation, and complete separation of aqueous two phase systems may occur in timescales of the order of tens of hours.⁸⁻¹⁰ These types of processes also often involve highly concentrated mixtures that can be difficult to access and control in high speed droplet generation, which works best for low viscosity, inert, and homogeneous samples. These considerations suggest a need to develop methods to store and concentrate microscale droplet reactors over long timescales.

A brief summary of microfluidic designs that specifically address the first issue of long-term storage and observation of droplets will be reviewed here. In the simplest case, the droplets that are generated using the microfluidic nozzles described in the previous chapter flow in a long outlet channel at a controlled size and spacing. The flow is then stopped and the drops come to rest, maintaining constant spacing.^{8,11-13} The droplet shape, size, and spacing are set by flow conditions and channel geometry, and so droplet generation and storage are inherently coupled in this system.

Separate trapping and storage modules have been designed that decouple the generation technique from the droplet trapping. In one type of trap system,¹⁴⁻¹⁷ the design takes advantage of the fact that droplets deform to fit in the confines of the microchannel and are therefore not at the lowest possible surface energy. A

channel expansion in any direction allows the droplet to relax and attain a lower surface energy. This energy decrease can be used to pin the droplet in place in the presence of flow slower than a critical flow rate or to guide droplets along a desired path.¹⁶⁻¹⁸

Another type of trapping system uses capillary forces to hold a droplet in place using restrictions placed along the path of fluid flow.^{15,19-22} One example of this trapping technique is the trap and bypass unit, shown in Fig. 5.1, which has been previously developed and characterized by Boukellal *et al.* and Bithi and Vanapalli.²³⁻²⁵ A pre-formed droplet enters the trap from the horizontal channel to the left of the trap. The restriction to the right of the trap introduces an increased resistance to flow and prevents the droplet from leaving the trap. The presence of the droplet increases the resistance to flow through the trap. The next droplet follows the first along the horizontal channel, but because the trap is filled and the path through the trap is unfavorable, this droplet will travel along the bypass channel instead.

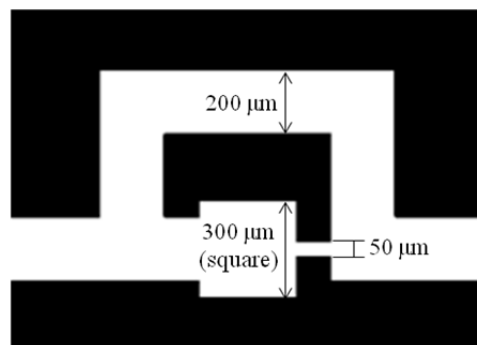


Figure 5.1. Schematic diagram of a microfluidic trap unit that consists of a 300 μm trap and 200 μm bypass channel. The uniform depth of the channel is $h = 100 \mu\text{m}$.

The trap and bypass unit can also be used to simultaneously create and store droplets. As shown in Fig. 5.2, the trap and bypass are initially filled with

only the continuous phase fluid. A slug of the droplet phase flows in and enters the bypass channel. The resistance to flow increases in the bypass channel, and so the slug enters and fills the trap instead. The slug meets the restriction at the other end of the trap, which has a higher resistance to flow than the bypass, so the slug continues to flow through the bypass again. Eventually, the tail of the slug reaches the junction of the bypass and trap, and slug breakup occurs due to shear forces. A droplet is formed from the breakup and is held in the trap. The remainder of the slug repeats the process for the next trap and bypass unit. An array of these trap and bypass units can be filled likewise to yield an emulsion of tunable composition and spacing.^{23,25} In the studies described in this chapter, this particular droplet generation and trap system is used to form droplets of a desired size, composition, and spacing for observations spanning tens of hours to days.

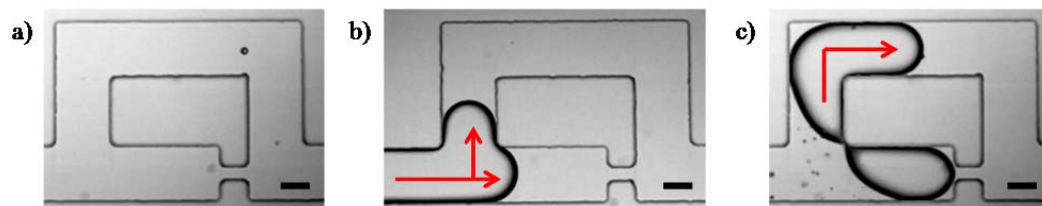


Figure 5.2. Formation and storage of a single drop inside a trap and bypass unit. (a) The trap and bypass are filled with mineral oil. (b) A slug of the droplet phase enters the trap and bypass simultaneously. The trap fills first until it reaches the restriction, and then the rest of the slug enters the bypass. (c) The tail end of the slug reaches the junction of the trap and bypass and pinches off a droplet that is held stationary within the trap. The remainder of the slug repeats the process with the next trap and bypass unit. Scale bar is 100 μm .

The droplet production method shown in Fig. 5.2 eliminates the need for a separate droplet generation technique, but produces a droplet size that is defined by the geometric parameters of the trap. For example, the 300 x 300 x 100 μm trap shown in Fig. 5.1 has a volume of 9 nL, so a droplet that fills the trap is expected to have a droplet volume that is on the order of several nanoliters. This

volume is significantly larger than the droplets generated in a flow-focusing device, where the droplet volume is controlled by the geometry of the nozzle and is typically hundreds of picoliters or smaller.

Additional manipulation of the droplet contents may be required once the droplets are stored. For example, an application may require controlled concentration adjustments in the droplet, which can be carried out by solvent removal. Microfluidic devices are regularly fabricated using polydimethylsiloxane (PDMS), which is slightly permeable to a variety of fluids including water and oil. The diffusion of water through the continuous phase oil and PDMS is negligible for droplet formation that occurs on the order of seconds, but becomes significant in static drops that are under observation for hours.²⁶ As a result, PDMS has been used as an inexpensive membrane material to control the exchange of solvents between compartments in multilayer devices and for controlled dehydration over time.²⁷⁻³⁰

A typical microchannel geometry with a rectangular cross-section consists of a depth h that is much smaller than the width of the trapping area w_t . A large droplet deforms to fill the trap and attains a pancake shape (Fig. 5.3).²⁹ When the depth and width of the channel are comparable, such as in Fig. 5.1, the mass transport of water can be modeled most simply as that of a species diffusing from a sphere into an infinite medium.³¹ In this situation, a spherical droplet containing an aqueous solution with an initial radius a_o diffuses into an infinite oil medium. Any solute present is assumed to remain in the droplet and only water diffuses out of the droplet. The diffusion coefficient of oil into the droplet $D_{o \rightarrow w}$ is expected to

be significantly smaller than that of water into the oil $D_{w \rightarrow o}$. The interface between the droplet and the oil phase is assumed to be in thermodynamic equilibrium, and thus fully saturated with water, so the concentration at the interface is equal to the saturation concentration c_s . The concentration of water is assumed to be independent of time, which is expected to hold at early times. When solute effects are negligible, the radius of the spherical droplet a at time t is

$$a(t) = \left(a_o^2 - \frac{6Dc_s}{\rho_w} t \right)^{1/2},$$

where D is the diffusion coefficient of water through the oil phase and ρ_w is the density of water. The volume of the droplet at time t is then

$$V(t) = \frac{4}{3} \pi \left(a_o^2 - \frac{6Dc_s}{\rho_w} t \right)^{3/2} \quad (5.1)$$

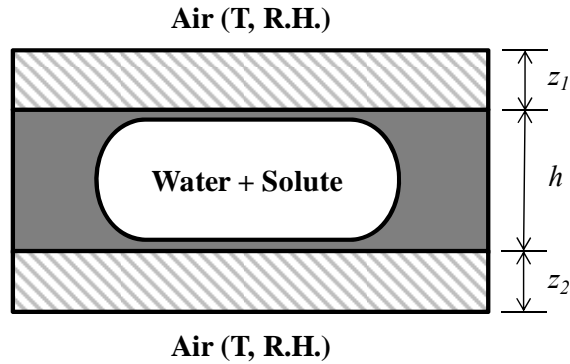


Figure 5.3. A side view of the microfluidic trap with the oil phase represented in gray, and the PDMS channel walls with crosshatching. Water will diffuse from the droplet through the oil and PDMS, and evaporate into the air surrounding the device.

In the following studies, the permeability of PDMS is shown to be a useful tool for controlling the dehydration of droplets over tens of hours in air. We first show that in the case of pure water, the droplets continuously shrink and eventually disappear altogether. The rate of dehydration is examined as a function of parameters such as relative humidity and droplet contents. We also use the

changing properties of the droplet containing a concentrating solution to verify the accuracy of volume measurements made within the device.

5.2 Materials and Methods

The microfluidic trap design used in the dehydration experiments is similar to those published previously by Boukellal *et al.* and Bithi and Vanapalli.^{23,24} As seen in Fig. 5.1, each trap unit consists of a square trap with a side length $w_t = 300 \mu\text{m}$ and bypass channel with a width $w_b = 200 \mu\text{m}$. The volume of the drops formed with this geometry is approximately 8 nL. Trap units are placed 1.4 mm center-to-center from the next trap to form a square array consisting of 10 rows of 25 units each, for a total of 250 traps in a microfluidic device. Two rectangular channels run perpendicular to the rows of traps to connect the rows and allow for fluid to fill each row in parallel.

A SU-8 master mold of the array design and the corresponding microfluidic devices are fabricated using the techniques described in Chapter 3. Because droplet dehydration is affected by the permeability and thickness of the device material, the formulation and total amount of polydimethylsiloxane (PDMS) used to make the microfluidic devices are carefully monitored to prevent unintended fluctuations in dehydration rate. 12.34 g of PDMS prepared using a 10:1 pre-polymer to cross-linking agent ratio is poured into the 3” Petri dish holding the microchannel mold; 9.62 g is used for the PDMS slab to close the channels. The amounts used for each side ensures a constant PDMS device

thickness across all experiments. After the final bake step to complete the bonding process at 60°C, all devices are trimmed to an area of 4.5 cm x 2 cm.

The devices are soaked in the water-saturated continuous phase oil for at least five days to ensure full saturation of the PDMS with the continuous phase oil. This step minimizes any effects from a second diffusing phase on the dehydration rate by removing the driving force for the diffusion of the oil into the PDMS. Prior to running an experiment, the oil-saturated devices are soaked in water overnight to saturate the entire device with water. This ensures that droplet dehydration is affected only by the relative humidity of the device storage environment, which acts as a mass transfer boundary condition by establishing a concentration gradient between the droplet and the exterior of the device.

Three continuous phase oils are used in the droplet dehydration experiments. Mineral oil (Fisher Scientific), 100 cSt silicone oil (Gelest, Inc.), and octanol (Fisher Scientific) are obtained and filtered through a 0.45 µm filter (Thermo Scientific Nalgene 25mm Syringe Filters). The oils are saturated with water by continuously mixing the oil with water for an hour and then allowing the two phases to separate overnight. The oil layer is retained for use in experiments, while the water layer is discarded. Span 80 (Sigma Aldrich) is dissolved in mineral oil in concentrations of 1, 3, and 5 wt. %; no surfactants were added to the silicone oil. The refractive indices of these continuous phases are measured using an automatic reflected light refractometer (Reichert AR70 Automatic Digital Refractometer). Octanol is not saturated with water prior to use, and experiments performed using octanol are carried out in mineral oil-saturated

devices. This is to avoid complications with droplet formation, as the dispersed phase has been observed to wet octanol-saturated PDMS channel walls, preventing reproducible, robust droplet formation.

Solvents, however, are known to swell cross-linked PDMS, which alters both the thickness of the device and the expected dimensions of the microchannel. Water and low molecular weight alcohols do not swell PDMS significantly, but alkanes and silicone oil can significantly affect the PDMS dimensions.³⁴ The device thickness is monitored across all experiments and is 1.9 ± 0.1 mm for both PDMS slabs after full saturation with mineral or 100 cSt silicone oils. A top-down view of the channel provides a measure of changes due to PDMS swelling, and the channel geometry is typically within $5 \mu\text{m}$ of the original design dimensions. An estimate of the depth of the channel h is acquired by imaging a cross-sectional cut of the microchannel and is typically measured to be $90 \pm 5 \mu\text{m}$. The measured channel dimensions are therefore approximately the same as the original design dimensions, which indicates that none of the oils swell the PDMS significantly.

For the dispersed phase fluid, water, sodium chloride solutions, and sucrose solutions are used. Deionized water (resistivity = $18.2 \text{ M}\Omega\text{-cm}$) is obtained from a water purification system (Thermo Scientific Barnstead EasyPure II) and is used to make all solutions. NaCl (99%) is obtained from Fisher Scientific and solutions with initial concentrations of 1 or 100 mM are prepared. Sucrose (Fisher Scientific) is purified by recrystallization in ethanol (Pharmco-Aaper 190 Proof, 95%, ACS/USP Grade). Two grams of sucrose is added to ethanol and heated to boiling. Additional ethanol is added until the sucrose is fully

dissolved. The sucrose-ethanol solution is allowed to cool to room temperature and is then transferred to a refrigerator for two weeks to allow sucrose crystals to form. The crystals are then filtered and rinsed with cold ethanol before being placed in a vacuum chamber for 24 hours. Sucrose solutions are made by dissolving the purified sucrose crystals in deionized water. All solutions are filtered using a 0.2 μm filter (Pall Acrodisc CR PTFE Syringe Filter).

Fluids are introduced into the microchannels via polyethylene microtubing (Scientific Commodities PE/4) that is inserted into the inlet hole of the PDMS device and held in place by friction. The tubing is connected to a plastic syringe (BD Luer-Lok syringe) fitted with a needle (BD Single Use 20 gauge, 1.5" needle). Fluid flow is controlled by syringe pump (Harvard Apparatus PHD2000 or Braintree Scientific BS-8000) at flow rates of 0.5 to 5 $\mu\text{L}/\text{min}$.

An array of droplets is created in the PDMS device by first filling the array with the continuous phase oil and waiting for approximately five minutes before the droplet phase is introduced into the microchannel (Fig. 5.2a). In the case of mineral oil with Span 80, this waiting period allows the surfactant to absorb to the PDMS surfaces and decreases the number of issues that arise from partial wetting of the droplet phase. The same protocol is used with silicone oil and octanol to maintain consistency across the different experiments. A 10 μL slug of the dispersed (droplet) phase is then introduced into the channels at a flow rate of 2-5 $\mu\text{L}/\text{min}$. This volume is significantly greater than needed to form 250 droplets, but the excess volume ensures that > 96% of the traps will be filled with a single large droplet. The continuous phase liquid is reintroduced into the device

at a flow rate of 0.5 to 2 $\mu\text{L}/\text{min}$. This last step pushes the droplet phase through the rows of trap and bypass units (Fig. 5.2b); breaks off droplets from the tail end of the slug at the junction of the trap and bypass; and repeats for each trap in the row, thereby creating and storing one droplet in each trap. The excess dispersed phase liquid exits the device, leaving an ordered matrix of droplets in a continuous phase fluid shown in Fig. 5.4.

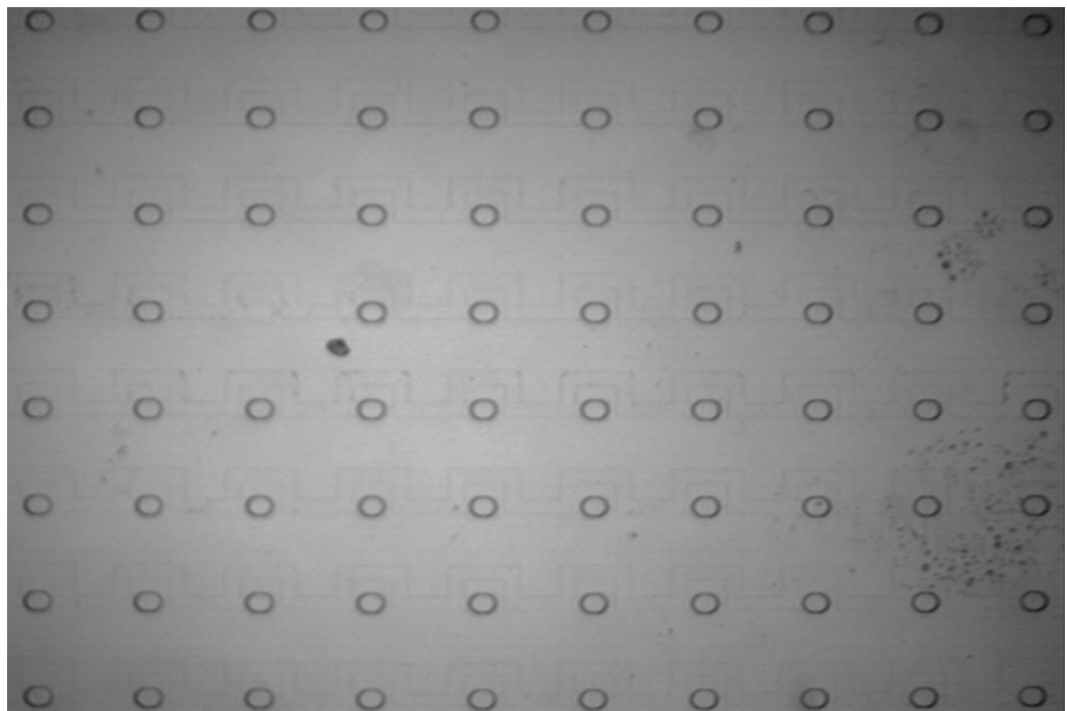


Figure 5.4. An example section of a 10x25 microfluidic trap array. The same trap shown in Fig. 5.1 is patterned in a square array. Droplets are spaced 1.4 mm apart (center-to-center).

Droplets are monitored using an inverted microscope (Nikon Eclipse Ti-U or TE2000-U) fitted with either a 2X or 4X objective and illuminated in bright field. Images are recorded using a camera with either CCD or CMOS sensors (Allied Vision Technologies Guppy Pro; Allied Vision Technologies Prosilica; Redlake IDT XS5; Vision Research Phantom v9.1) attached to a microscope port.

While there are 250 drops within a single device, only 50 drops (two rows, 25 drops per row) are monitored for the duration of the experiment. The time

required for each experiment depends on several factors, but is most impacted by the relative humidity and is typically between 3-14 hours. Images are taken at least once an hour during this time, and more frequently near times of interest (i.e. shape transitions, crystallization). For extended (> 14 hours) experiments, four drops are automatically monitored at frame rates from 0.01 to 0.15 fps.

As the droplets shrink over time, the droplet shape transitions between the three distinct droplet shapes depicted in Fig. 5.5. The droplet shape transitions modeled in the previous chapter are observed in the following order as the droplet volume decreases: the droplet initially fills the trap as a slug, then becomes a cylindrical pancake, and finally becomes spherical. Image analysis is performed using ImageJ (National Institutes of Health) using two protocols to measure the droplet size. The length of a slug-shaped droplet D_{slug} (Fig. 4.3) is obtained by measuring the peak-to-peak distance of the intensity profile along the horizontal axis of the droplet. For pancake-shaped and spherical droplets, a circle is fitted to the droplet to measure the perimeter of the droplet, and the corresponding drop diameter is calculated. The droplet size obtained from ImageJ is in pixels and is converted to microns using the appropriate pixel to micron conversion factor listed in Table 3.2.

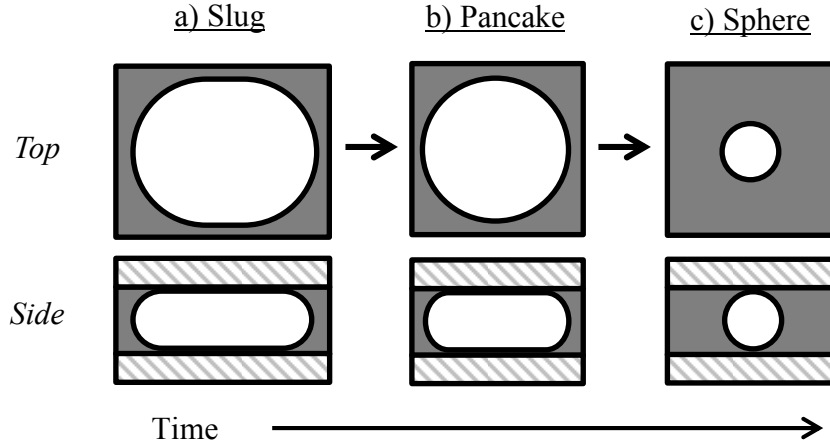


Figure 5.5. Evolution of droplet shape as droplet volume decreases with time. The aqueous phase is represented in white, the oil phase in gray, and the PDMS channel walls with crosshatching.

The geometric model of shape and structure transitions described in the previous chapter is used to estimate the volumes of the droplets in the trap array as the droplet decreases in size over time. In the trap and bypass unit design, the width of the trap w_t is the dimension that will define the volume of a slug droplet (Eq. (4.9)), as well as the volume at which the droplet shape transitions between a slug and a pancake (Eq. (4.8)). The volume of a slug-shaped drop V_{slug} is given by

$$V_{slug} = w_t h (D_{slug} - w_t) + \frac{1}{2} \left[\frac{\pi h^3}{6} + \frac{\pi h}{4} (w_t - h) \left(\frac{\pi h}{2} + w_t - h \right) \right]. \quad (5.2)$$

The volume at which the slug to pancake shape transition occurs is

$$V_{ps} = \frac{\pi}{8} w_t h [(\pi - 4)h + 2w_t] + \frac{\pi}{24} h^3 (10 - 3\pi). \quad (5.3)$$

The equations for the volume of pancake-shaped (Eq. (4.5)) and spherical droplets

($V_{sphere} = \frac{\pi}{6} D_{sphere}^3$) as well as the equation for the transition between these two

shapes (Eq. (4.3)) remain the same.

As described previously, the device and all continuous phase fluids are saturated with water prior to running the experiment to minimize dehydration variations across devices. The PDMS devices are placed in a homemade humidity chamber, where the relative humidity is systematically varied to control the dehydration rate of the droplets. The humidities tested in these experiments are 5%, 25%, 50%, and 75%. The basic setup of the humidity chamber used in these experiments involves a small, plastic container and two inlet streams: a dry air stream from the house air and a saturated air stream produced by bubbling house air through water. The humidity is manually tuned and is measured using a humidity probe (Digi-Sense Thermohygrometer with Dew Point). For higher humidities (>50%), there is a 5% decrease in humidity over 24 hours, while the decrease is about 2% for the lower humidities (<25%). Note that the concentration of pure water is 55 M, while the concentration of water in air at 20°C and 100% relative humidity is 10^{-3} M. This indicates that even at high humidities, there is a water concentration gradient that drives dehydration. The devices are also immersed in a water bath such that the external concentration of water is 55 M, removing the driving force for mass transfer and allowing for the test of the ability to stop dehydration.

5.3 Results and Discussion

An example of the temporal evolution of a droplet stored in a microfluidic trap with mineral oil as the continuous phase fluid is displayed in Fig. 5.6. The droplet shown in Fig. 5.6a is generated using the create-and-store method

described by Boukellal *et al.*,²³ and can be approximated by the model slug shape depicted in Fig. 5.5a. Over ten hours, the droplet decreases in size; transitions to a pancake shape (Figs. 5.6b-5.6e); and attains the shape of a sphere (Fig. 5.6f), which correspond to the model shapes shown in Figs. 5.5b and 5.5c, respectively. The droplet fully dehydrates and disappears after 12 hours at 5% relative humidity.

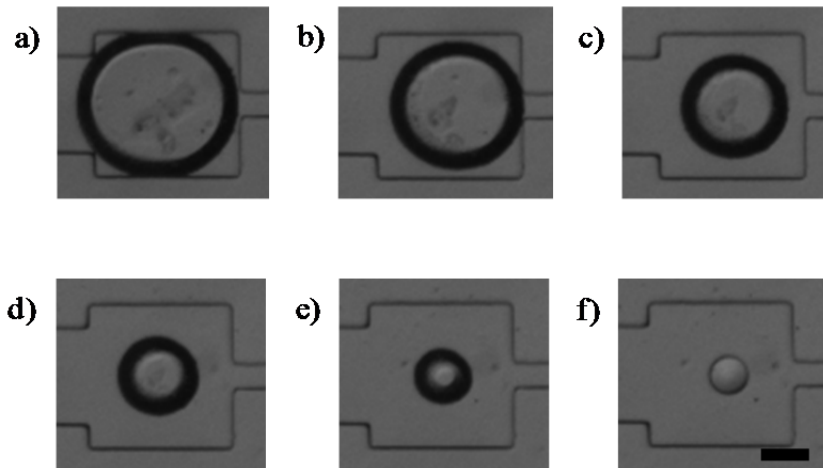


Figure 5.6. A typical image progression of the dehydration of a trapped droplet over 10 hours at 5% relative humidity. Mineral oil is used for the continuous phase fluid. Two hours have elapsed between each image from left to right. Scale bar is 100 μm .

The droplet volume is calculated from the images shown in Fig. 5.6 using the equations for the volumes of slug-shaped droplet (Eq. (5.2)), a pancake-shaped droplet (Eq. (4.3)), and a sphere. Fig. 5.7 plots the average droplet volume over time for an array of drops surrounded by mineral oil that is stored within an environment held at 5% relative humidity. Three sets of data are plotted, each set corresponding to a separate array of droplets that is stored in different devices but has dehydrated under the same conditions. Each data point represents an average of 12-25 droplets sampled within a single device, and the error bars indicate the

sample standard deviation. The droplet volume decreases from an initial droplet volume of ~8 nL to zero over 12 hours.

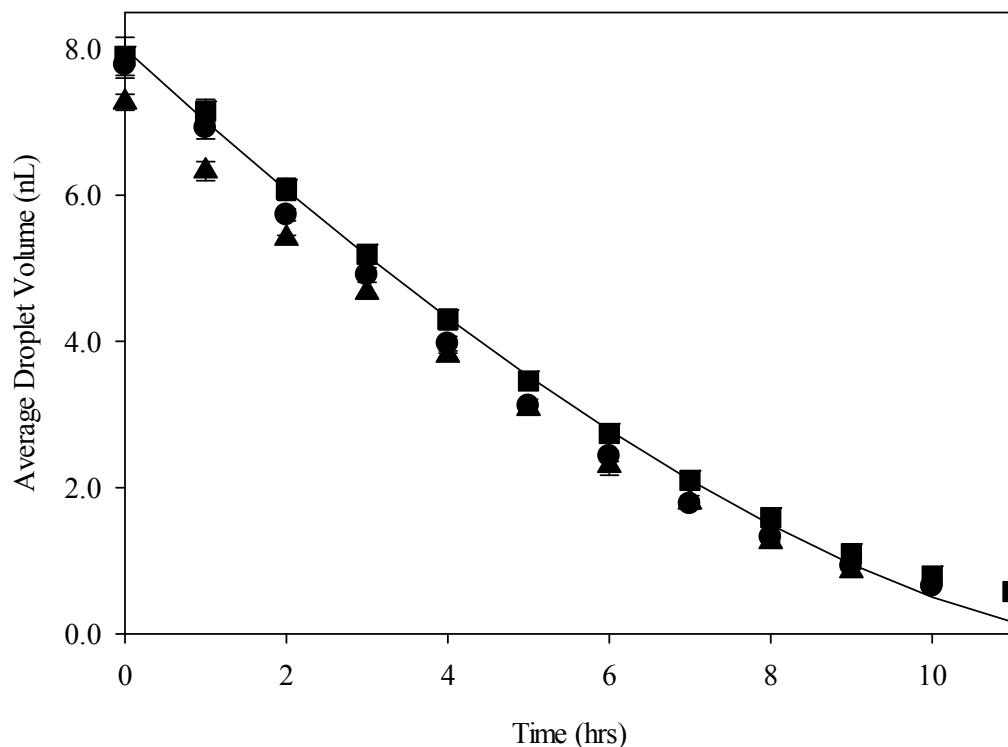


Figure 5.7. Average droplet volume measured in three different devices at 5% relative humidity. Each filled symbol shape represents a separate device. The solid line is a fit to the spherical model Eq. (5.1). Mineral oil is used for the continuous phase fluid. Error bars indicate the standard deviation of the droplet volumes in the array.

The slope of the droplet volume versus time curve is the droplet dehydration rate. As seen in Fig. 5.7, the dehydration rate is not constant and decreases with time. The small (~2%) standard deviation associated with each data point indicates that the droplets stored within an array dehydrate at the same rate across a single device, and the device design can thus be used to generate statistical information pertaining to concentrating processes occurring in a droplet for a given system. In contrast, the image resolution from the microscope and

camera setup produces a propagated error of $\sim 10\%$ in the volume measurements (Fig. 5.9). Pixilation therefore contributes more to the uncertainty in the results than the experimental protocol. This can be simply rectified by increasing the magnification and/or using a camera with better resolution, but it also suggests that there is a tradeoff between obtaining accurate volume measurements and statistical data about the system encapsulated within the droplet. A comparison of the three experiments performed in separate devices shows some variability between the dehydration curves, especially at earlier times. There is good agreement between the three repetitions overall, however, and dehydration behavior appears to be reproducible both across droplets in a single device and across arrays stored in different devices. In addition, the droplets are trapped and stored without additional manipulation of the drops,²³ making this a simple microfluidic platform for generating droplets for long-term observations.

The droplet dehydration data shown in Fig. 5.7 are also compared with the predicted volume as a function of time calculated from Eq. (5.1). This model does not take into account that water must diffuse through two media (PDMS and oil) that may have different diffusion coefficients in the microfluidic device. However, the diffusivity of water through PDMS is $D \sim 10^{-9} \text{ m}^2/\text{s}$, which is similar to that of water through mineral oil.^{29,32,33} To simplify the model, a single effective diffusion coefficient is assumed to be valid for the system. Eq. (5.1) is fitted to the experimental data by varying the diffusion coefficient D . Using an initial droplet radius $R_o = 125 \text{ }\mu\text{m}$ (calculated from an initial volume $V_o = 8 \text{ nL}$); the saturation concentration of water in oil at 20°C $c_s = 0.050 \text{ kg/m}^3$; and the

density of water $\rho_w = 1000 \text{ kg/m}^3$, with a time t_o beginning at the formation of the droplet, an effective diffusion coefficient $D = 1.2 \times 10^{-9} \text{ m}^2/\text{s}$ is obtained, which matches the experimental data reasonably well. This value also agrees with the literature values reported for the diffusion coefficient of water through both mineral oil and PDMS, which vary between 1×10^{-9} and $2 \times 10^{-9} \text{ m}^2/\text{s}$.^{29,32,33}

To assess the accuracy of the model volume equations used to calculate the droplet volumes shown in Fig. 5.7, we use the refractive index dependence on solute concentration. Assuming that only water diffuses out of the drops, dehydration of the droplets concentrates any solutes contained within the drop. As the concentration of a solute increases, the physical properties of the solution may also change. Two of the properties commonly affected are the density and refractive index. The refractive index increases from approximately that of pure water ($n = 1.33$ at 25°C) to that of the pure solute. As a result, solutions of varying solute concentration can be used as calibration standards for refractometers. A common standard is sucrose, whose refractive index varies from 1.33 to 1.49 for concentrations between 0 and 3.3 M, respectively. Fig 5.8 plots the refractive index of sucrose versus concentration.³⁵ A linear relationship can be fit to this data, and the concentration of a sucrose solution $C_{sucrose}$ required to achieve a specific refractive index $n_{solution}$ can be calculated from the relationship

$$n_{solution} = 0.048C_{sucrose} + n_{solvent} \quad (5.4)$$

where $n_{solvent}$ is the refractive index of pure water in this case and is equal to $n_w = 1.33$ at room temperature. The slope of the linear relationship is an empirical constant that depends on the solute. The refractive indices of many pure oils fall

within the range of values attained by sucrose solutions. Three values are marked on Fig. 5.8 that correspond to the silicone oil, octanol, and mineral oil used in the present dehydration experiments.

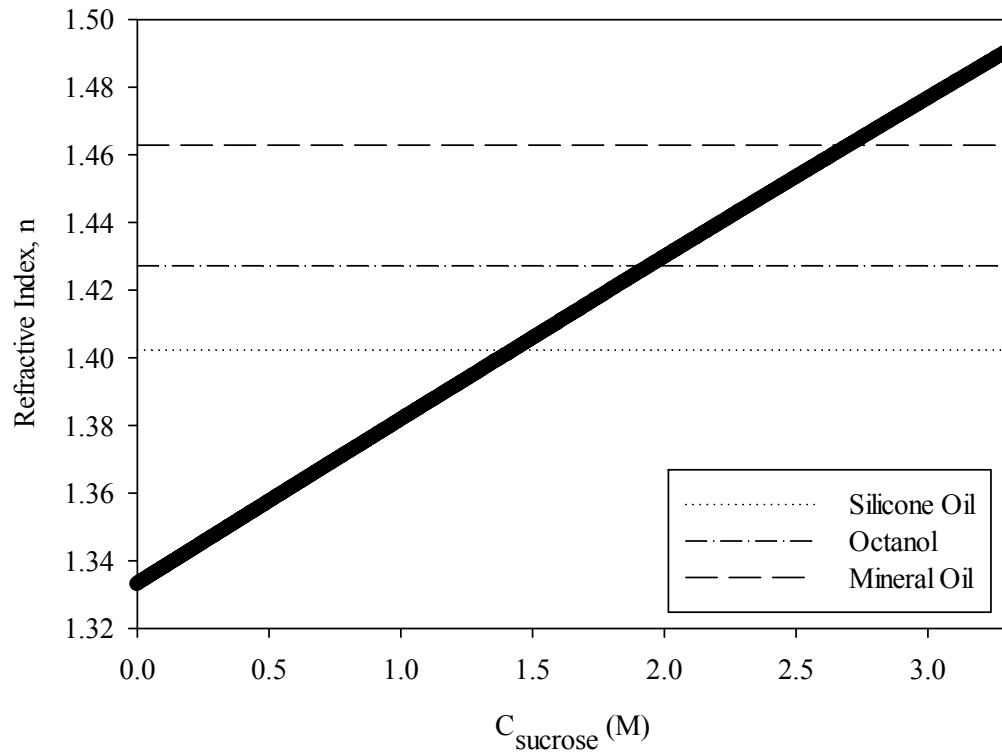


Figure 5.8. Refractive index varies linearly with sucrose concentration with the relationship $n_{\text{solution}} = 0.048C_{\text{sucrose}} + n_{\text{solvent}}$, where n_{solvent} is equal to the refractive index of water, $n_w = 1.33$. The refractive indices of silicone oil ($n = 1.40$), octanol ($n = 1.43$), and mineral oil ($n = 1.46$) with 5% (w/w) Span 80 are marked by the horizontal lines. Data from Ref. 35.

In the previous chapter, the droplet volume calculations presented are based on geometric approximations of the three dimensional droplet shape. The accuracy of these approximations can be assessed by verifying the concentration C_{match} at which the sucrose solution refractive index equals that of the continuous phase oil. Visually, a droplet containing a sucrose solution dehydrates and eventually disappears once it has attained the concentration C_{match} (Fig. 5.9b). The

droplet reappears as the volume continues to decrease (Figs. 5.9c and 5.9d) and the contrast in index of refraction returns. Specific droplet volumes can be probed by using the criterion

$$n_{solution}(C = C_{match}) = n_{oil} \quad (5.5)$$

at a known droplet volume V_{match} . By varying the initial sucrose concentration $C_{initial}$, Eq. (5.5) can be satisfied at a desired volume regardless of the droplet shape, and therefore can be used to independently validate the geometric assumptions made in Section 5.2. Combining Eqs. (5.4) and (5.5) with conservation of mass,

$$C_{initial}V_{initial} = C_{match}V_{match}, \quad (5.6)$$

the expected droplet volume at which Eq. (5.6) is satisfied can be estimated by the relationship

$$\frac{V_{match}}{V_{initial}} = \frac{0.048C_{initial}}{n_{oil} - n_{solvent}}. \quad (5.7)$$

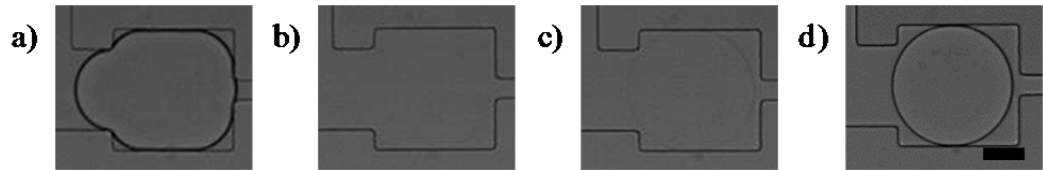


Figure 5.9. An example of a droplet of sucrose undergoing refractive index changes as the droplet volume decreases and solute concentration increases. a) Initial trapped sucrose droplet. b) Some water has diffused out of the droplet and has achieved the concentration where $n_{droplet} = n_{oil}$. c & d) The droplet has continued to dehydrate and has reappeared. Scale bar is 100 μm .

Five droplet volumes are selected to be verified in three continuous phase oils. The oils chosen are mineral oil with 5 wt. % Span 80 ($n = 1.46$), octanol ($n = 1.43$), and silicone oil ($n = 1.40$). The volumes tested correspond to the three droplet shapes (slug, pancake, and sphere) and the two droplet shape transitions as

defined by Eqs. (4.3) and (5.3). The experiments are designed based on an average initial droplet volume $V_{initial} = 8$ nL to calculate the initial concentration required to refractive index match at the desired volumes for a given oil using Eq. (5.7). The starting concentrations of sucrose solutions listed in Table 5.1 are loaded into separate devices at 5% relative humidity. Droplet sizes are measured on the images immediately following the reappearance of the droplet once a distinct droplet interface can be discerned. Because there are slight variations between each droplet in the array and each array that is formed, the volumes and concentrations of interest are calculated for each droplet individually.

			<i>confined</i>	<i>transition</i>	<i>pancake</i>	<i>transition</i>	<i>sphere</i>
Oil	$n_{D,measured}$	$C_{m,calc}$ (M)	$C_{i,calc}$ (M)				
silicone oil	1.4023	1.44	1.23	1.11	0.62	0.07	0.03
octanol	1.4272	1.96	1.68	1.52	0.84	0.10	0.04
mineral oil	1.4629	2.70	2.32	2.09	1.16	0.13	0.06

Table 5.1. Initial sucrose concentrations used in the volume verification experiments given the average initial droplet volume (7.6 nL) and the desired droplet volumes: confined: 6.0 nL, transition to pancake: 5.4 nL, pancake: 3.0 nL, transition to sphere: 0.3 nL, sphere: 0.2 nL. The oil index of refraction and corresponding match concentration C_{match} of the sucrose are used to calculate the initial concentration needed to attain C_{match} at the desired volume in the five columns on the right.

Fig. 5.10 is a plot of the quantity $(V_{match}/V_{initial})(n_{oil}-n_{solvent})$ versus initial sucrose concentration $C_{initial}$ for mineral oil. The data points correspond to the experimental values obtained for $(V_{match}/V_{initial})(n_{oil}-n_{solvent})$ for the droplets dehydrated from the corresponding initial concentrations $C_{initial}$ listed in Table 5.1. The predicted values for these experiments are calculated using Eq. (5.7) and plotted as the sloped solid line in Fig. 5.10. The experimental and predicted curves show that as the initial droplet concentration increases, the droplet volume at which Eq. (5.5) is satisfied increases. In decreasing values of the scaled volume

$(V_{match}/V_{initial})(n_{oil}-n_{solvent})$, the horizontal dotted lines indicate the target volumes of a slug-shaped droplet (6 nL; Eq. (5.2)); slug to pancake transition (5.4 nL; Eq. (5.3)); pancake-shaped (3 nL; Eq. (4.5)); pancake to sphere transition (0.3 nL; Eq. (4.3)); and spherical droplet (0.2 nL). The error bars are equal to the error propagated from image pixilation.

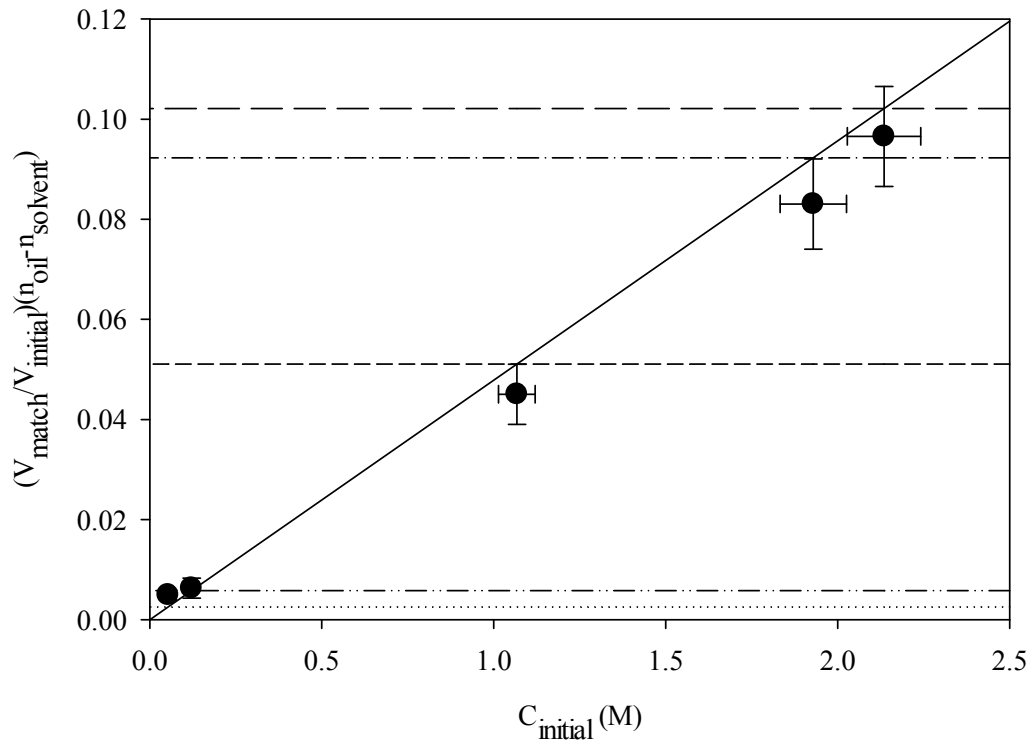


Figure 5.10. Refractive index verification of droplet volumes in mineral oil. Predicted scaled volumes for each droplet shape or transition using equation for the volume of a slug (—), slug to pancake transition (- · -), pancake (- - -), sphere to pancake transition (- · -), and sphere (···) are shown as horizontal lines.

The experimental data points are expected to be located at the intersection of the horizontal target volume and predicted refractive index match volume lines. Within error, the experimental values show good agreement between the experimental volumes and the predicted values given by Eq. (5.7). A comparison of each data point to its corresponding shape-dependent target volume also shows

reasonable agreement. The data points corresponding to the slug to pancake transition and the pancake volumes are just outside of the reported error bars, and may be due to the error introduced from the protocol used to measure the droplet size. This measurement is made after the droplet has dehydrated past the refractive index match volume, so the experimentally obtained value where Eq. (5.5) is satisfied would be systematically lower than the predicted value, and may contribute to the low refractive index match volumes observed in Fig. 5.10.

Fig. 5.11 is a plot of the quantity $(V_{match}/V_{initial})(n_{oil}-n_{solvent})$ versus initial sucrose concentration $C_{initial}$ for the experiments performed in mineral oil (●), octanol (■), and silicone oil (▲). The data points correspond to the experimental values obtained for $(V_{match}/V_{initial})(n_{oil}-n_{solvent})$ for the initial sucrose concentrations and oil pairs listed in Table 5.1. By plotting the scaled droplet volume versus initial solute concentration, the data for each oil collapses onto the line with a slope equal to the empirical constant from Eq. (5.4). The target volumes plotted as horizontal dotted lines in Fig. 5.10 depend on the continuous phase oil used, so the expected volumes where Eq. (5.5) is satisfied are not included in Fig. 5.11. The refractive index of each oil defines the maximum value accessible for the quantity $(V_{match}/V_{initial})(n_{oil}-n_{solvent})$ in that solution-oil pair, and as the refractive index of the oil decreases, the scaled droplet volume also decreases.

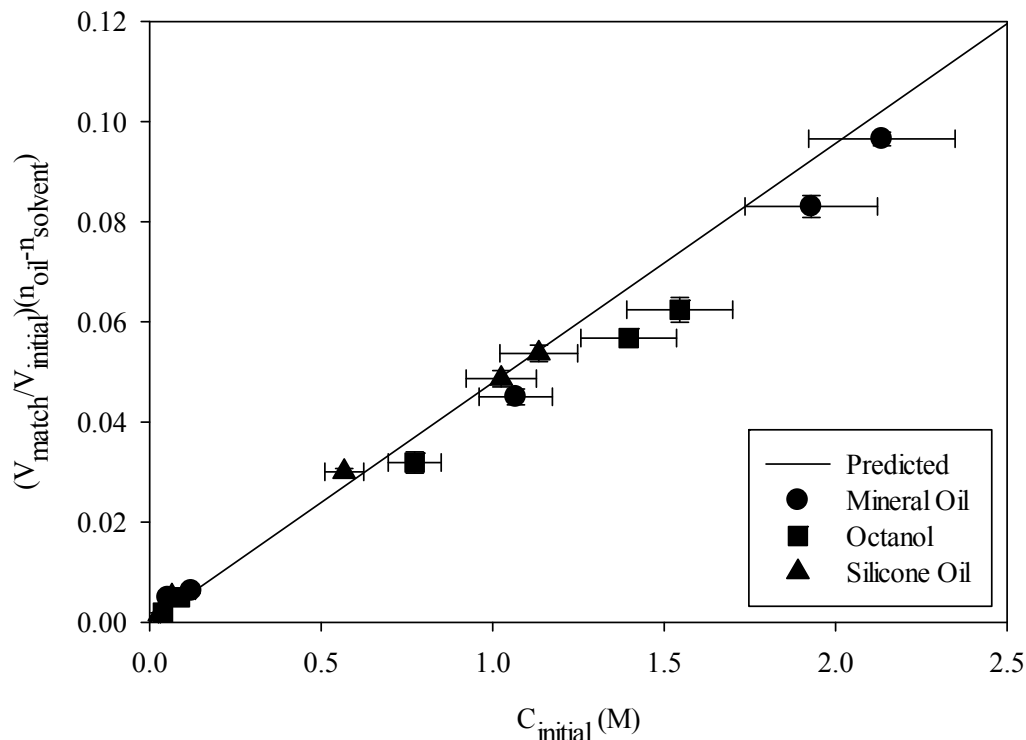


Figure 5.11. Scaled droplet volume versus initial concentration of sucrose for all droplet volumes in mineral oil, octanol, and silicone oil.

The results from the experiments carried out in silicone oil and mineral oil agree with the expected values to within experimental error, and overall, all three sets of experiments show that the model equations for droplet volume based on a given shape are valid. The volume verification experiments performed in octanol (■ in Fig. 5.11), however, show significant deviation from the expected values at high initial sucrose concentrations, even beyond the droplet measurement error that has already been discussed. These experiments correspond to the largest expected droplet volumes, which have the lowest relative error arising from pixilation. Given the good agreement between the experimental and expected values of droplets dehydrated in silicone and mineral oils, and the small error

introduced from the experimental protocol at large volumes, it is unlikely that this deviation is from systematic error. An underlying assumption in these droplet storage and dehydration experiments is that the continuous and droplet phases are completely immiscible. While this is generally true for mineral and silicone oils, octanol has a larger solubility and partitioning coefficient with water and a significant amount of both phases will most likely partition into the other phase. The octanol would raise the expected refractive index of the drop, while the water would lower the refractive index of the octanol around the droplet. Both of these trends would then lead to a decrease in the quantity $(V_{match}/V_{initial})(n_{oil}-n_{solvent})$, and would result in a value lower than predicted from the pure fluid refractive indices. The partitioning of octanol in water could therefore explain the deviation of the experimental results from the expected values at large droplet volumes. These results demonstrate that if a refractive index match between droplet and oil phases is used to verify droplet volume calculations, completely immiscible phases must be used to obtain an accurate assessment of the refractive index match concentration of an aqueous droplet stored in an oil.

To further characterize the dehydration of droplets stored in a PDMS device, the relative humidity of the air is tuned to vary the rate at which water diffuses out of the droplet. Because the dehydration rate is not constant, the experimental end time for a droplet to achieve its final state is used instead to show the effect of relative humidity on the overall dehydration behavior in the microfluidic devices. Fig. 5.12 plots the experimental end time for droplets containing water (●), 1 mM NaCl (■), and 100 mM NaCl (▲) dehydrated as a

function of humidity. The definition of the experimental end time differs slightly between systems, and is defined here as the time required for 75% of the drops imaged that initially contain water or 1 mM NaCl to disappear altogether, or the time for 75% of the drops initially containing 100 mM NaCl to crystallize or reach a steady drop size. Fig. 5.12 shows that an increase in relative humidity leads to a longer experimental time required for the droplet to reach its final state.

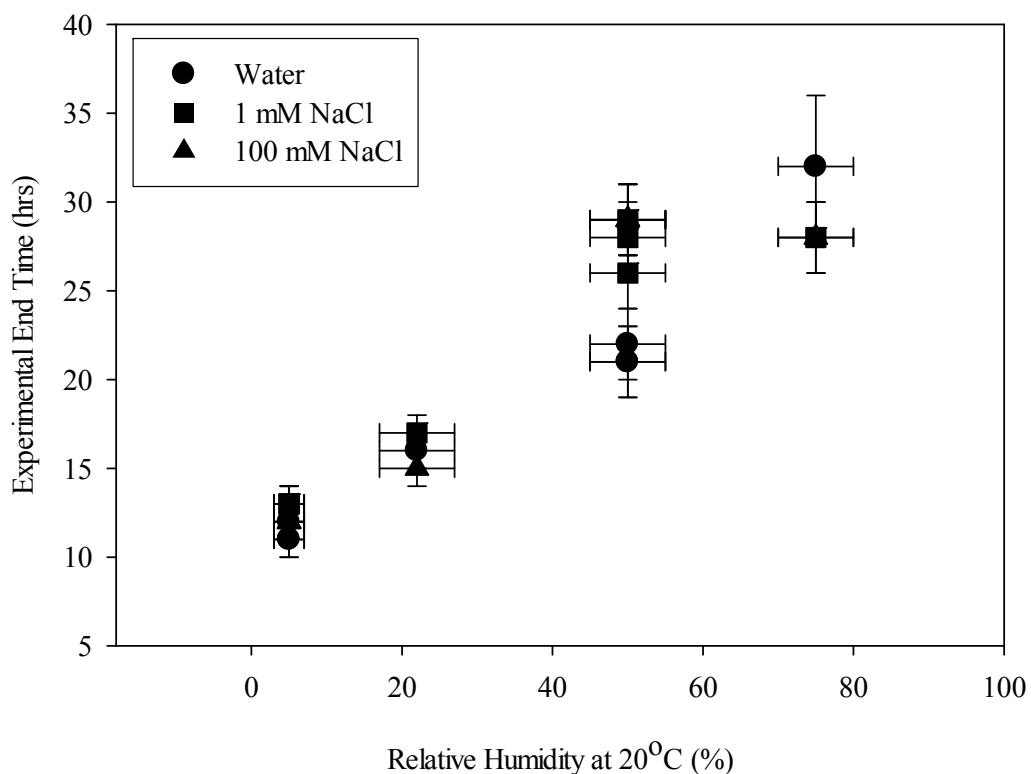


Figure 5.12. Time for 75% of the droplets sampled within an array to reach the final state (water – complete dehydration of droplet, NaCl – crystallization or constant droplet volume). All concentrations given refer to the initial concentration in the droplet.

The total time for droplet dehydration is of the order of tens of hours at 5% relative humidity and increases with increasing humidity. In order to decrease the amount of time required to fully dehydrate the droplets, other variables

governing the mass transfer out of the water must be considered. Mineral oil is used exclusively to study droplet dehydration in these experiments, and is known to have a low permeability to water compared to other oils.²⁴ Preliminary experiments carried out with 100 cSt silicone oil show a four hour difference in dehydration time at 5% relative humidity, indicating that significantly faster dehydration rates may be achieved by using an oil with a higher water permeability coefficient. Other experimental parameters can be similarly considered, such as dehydration of the oil with molecular sieves and a decrease in PDMS device thickness. Neither of these changes, however, results in an appreciable difference in the dehydration time.

The final droplet volumes are plotted versus relative humidity in Fig. 5.13 for droplets containing pure water (●), 1 mM NaCl (■), or 100 mM NaCl (▲) initially. Fully dehydrated droplets and crystallized droplets have a droplet volume equal to zero. Humidity does not have an effect on the final volume of the droplet in the pure water and 1 mM NaCl cases; all these droplets dehydrate completely regardless of the relative humidity. The final state of drop initially containing 100 mM NaCl, however, may either be a crystal or an uncrystallized droplet with a constant volume. The latter case is observed at higher relative humidities (> 50%), and the droplet remains uncrystallized while the device is held at constant ambient conditions.

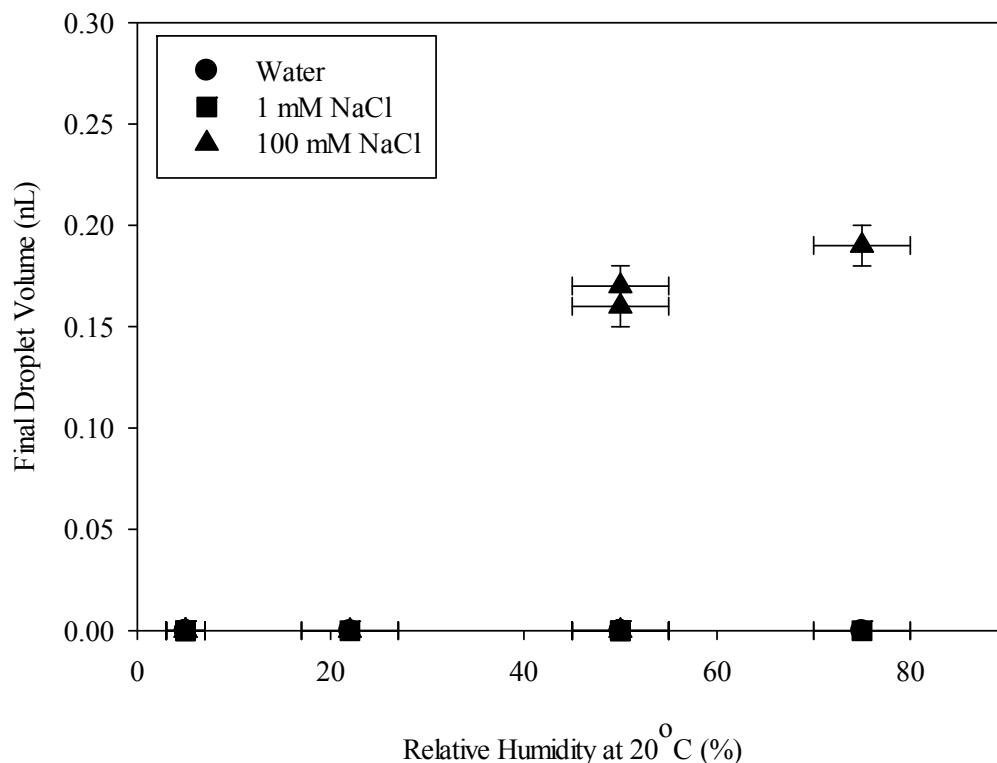


Figure 5.13. Final droplet volumes corresponding to the experiments shown in Fig. 5.12. The triangles represent $[\text{NaCl}]_i = 100 \text{ mM}$, which at higher humidities did not crystallize and remained at a constant final volume.

The suppression of crystallization at relative humidities greater than 50% suggests that a state has been achieved where the droplet is in equilibrium with the ambient environment, but the solute concentration is significantly higher than saturation. High supersaturation typically leads to a greater probability of crystallization, yet these droplets remain uncrystallized until the humidity is lowered and additional dehydration has occurred. This shows that dehydration in the microfluidic platform can generate stable, highly concentrated droplets.

At 75% relative humidity, the droplets containing pure water will dehydrate completely. In order to completely remove the driving force for

dehydration, the difference in chemical potential of water between the droplet and the air must be zero. This would require that the relative humidity be equal to 100%, but complete saturation of air with water vapor is difficult to achieve experimentally. As a result, the droplets stored in the microfluidic device are expected to dehydrate if the device is stored in air. To stop dehydration or to reverse the direction of the diffusion of water, the PDMS devices are submerged in a water bath. In the preliminary experiments, the devices are submerged immediately after forming the droplets. A small decrease in droplet volume is observed (<1 nL) before the droplet volume remains relatively constant for 10 hours; additional storage time in the pure water bath results in significant droplet growth. This result applies to both the water and NaCl droplets. Droplet dehydration is also successfully stopped at various times along the dehydration curve to achieve a desired droplet volume or solute concentration. It should be noted that the devices appear cloudy after extended submersion in water, but become clear again after the device is removed from the water bath and stored in air, regardless of the humidity. The cloudiness is associated with small water droplets that are embedded within the PDMS and subsequently evaporate. As a result, the initial saturation of the PDMS does not remove the driving force for the diffusion of water out of the device, and droplet dehydration is therefore expected to occur if the devices are stored in air.

The overall microfluidic device design has several operational considerations that may limit the types of systems that may be studied in the platform. Dehydration and equilibration of the device following the submersion of

the device is on the order of hours. Given these time scales, phenomena that occur in minutes at constant conditions would be difficult to separate from the effects of dehydration. In addition, the maximum dehydration rate achieved in these devices is a few nanoliters per hour, and is typically less than one nanoliter per hour. Bulk dehydration rates can be on the order of microliters per minute, and thus there may be a significant difference between the results observed in bulk drying experiments versus those obtained from dehydration of droplets in microfluidic experiments.

5.4 Conclusions

We have shown that droplet dehydration over tens of hours is reproducible and controllable using the microfluidic trap array platform. Aqueous droplets are generated and stored in a microfluidic device for tens of hours, during which the diffusion of water through the outer phase oil and PDMS device results in a controlled dehydration of the droplets. The droplet is confined by the walls of the microchannel, and as the droplet volume decreases, the droplet shape transitions to one of lower surface energy. Sucrose is used as a refractive index calibration standard to assess the accuracy of the model droplet volume equations in the microfluidic device. The measured concentrations at which the refractive index of the drop and oil are equal agree with the predicted values from the calibration curve to within experimental error, and droplet volumes are accurately calculated within these devices. The droplet dehydration rate is controlled by changing the ambient relative humidity; however, droplet dehydration can be arrested by

submerging the entire PDMS device in water, thereby removing the driving force for the diffusion of water. In addition, large sample sizes of drops may be monitored for extended periods of time without a significant volume or phase change. These characterization experiments demonstrate a proof of concept of a microfluidic platform that can be used to generate an array of identical droplets and to control the dehydration of the droplets.

5.5 References

1. Pompano, R. R.; Liu, W.; Du, W.; Ismagilov, R. F. Microfluidics Using Spatially Defined Arrays of Droplets in One, Two, and Three Dimensions. *Annual Review of Analytical Chemistry*. **2011**, *4*, 59-81.
2. Song, H.; Chen, D. L.; Ismagilov, R. F. Reactions in Droplets in Microfluidic Channels. *Angewandte Chemie International Edition*. **2006**, *45*, 7336-7356.
3. Seemann, R.; Brinkmann, M.; Pfohl, T.; Herminghaus, S. Droplet based microfluidics. *Reports on Progress in Physics*. **2012**, *75*, 016601.
4. Simon, M.; Lee, A. Microfluidic Droplet Manipulations and Their Applications. *Microdroplet Technology*. Springer New York, 2012, 23-50.
5. Christopher, G. F.; Bergstein, J.; End, N. B.; Poon, M.; Nguyen, C.; Anna, S. L. Coalescence and splitting of confined droplets at microfluidic junctions. *Lab on a Chip*. **2009**, *9*, 1102-1109.
6. Lee, C.-Y.; Chang, C.-L.; Wang, Y.-N.; Fu, L.-M. Microfluidic mixing: a review. *International journal of molecular sciences*. **2011**, *12*, 3263-3287.
7. Vuong, S. M.; Anna, S. L. Tuning bubbly structures in microchannels. *Biomicrofluidics*. **2012**, *6*, 022004.
8. Ildefonso, M.; Candoni, N.; Veesler, S. p. A Cheap, Easy Microfluidic Crystallization Device Ensuring Universal Solvent Compatibility. *Organic Process Research & Development*. **2012**, *16*, 556-560.
9. Martin, J. E. Slow aggregation of colloidal silica. *Physical Review A*. **1987**, *36*, 3415-3426.
10. Hardt, S.; Hahn, T. Microfluidics with aqueous two-phase systems. *Lab on a Chip*. **2012**, *12*, 434-442.
11. Laval, P.; Crombez, A.; Salmon, J.-B. Microfluidic Droplet Method for Nucleation Kinetics Measurements. *Langmuir*. **2008**, *25*, 1836-1841.
12. He, M.; Sun, C.; Chiu, D. T. Concentrating Solutes and Nanoparticles within Individual Aqueous Microdroplets. *Analytical Chemistry*. **2004**, *76*, 1222-1227.
13. Lau, B. T. C.; Baitz, C. A.; Dong, X. P.; Hansen, C. L. A Complete Microfluidic Screening Platform for Rational Protein Crystallization. *Journal of the American Chemical Society*. **2006**, *129*, 454-455.
14. Schmitz, C. H. J.; Rowat, A. C.; Koster, S.; Weitz, D. A. Dropspots: a picoliter array in a microfluidic device. *Lab on a Chip*. **2009**, *9*, 44-49.
15. Huebner, A.; Bratton, D.; Whyte, G.; Yang, M.; deMello, A. J.; Abell, C.; Hollfelder, F. Static microdroplet arrays: a microfluidic device for droplet trapping, incubation and release for enzymatic and cell-based assays. *Lab on a Chip*. **2009**, *9*, 692-698.
16. Dangla, R.; Kayi, S. C.; Baroud, C. N. Droplet microfluidics driven by gradients of confinement. *Proceedings of the National Academy of Sciences*. **2013**, 1-6.

17. Abbyad, P.; Dangla, R.; Alexandrou, A.; Baroud, C. N. Rails and anchors: guiding and trapping droplet microreactors in two dimensions. *Lab on a Chip*. **2011**, *11*, 813-821.
18. Fradet, E.; McDougall, C.; Abbyad, P.; Dangla, R.; McGloin, D.; Baroud, C. N. Combining rails and anchors with laser forcing for selective manipulation within 2D droplet arrays. *Lab on a Chip*. **2011**, *11*, 4228-4234.
19. Cohen, D. E.; Schneider, T.; Wang, M.; Chiu, D. T. Self-Digitization of Sample Volumes. *Analytical Chemistry*. **2010**, *82*, 5707-5717.
20. Shi, W.; Qin, J.; Ye, N.; Lin, B. Droplet-based microfluidic system for individual *Caenorhabditis elegans* assay. *Lab on a Chip*. **2008**, *8*, 1432-1435.
21. Simon, M. G.; Lin, R.; Fisher, J. S.; Lee, A. P. A Laplace pressure based microfluidic trap for passive droplet trapping and controlled release. *Biomicrofluidics*. **2012**, *6*, 014110.
22. Wang, W.; Yang, C.; Li, C. M. On-demand microfluidic droplet trapping and fusion for on-chip static droplet assays. *Lab on a Chip*. **2009**, *9*, 1504-1506.
23. Boukellal, H.; Selimovic, S.; Jia, Y.; Cristobal, G.; Fraden, S. Simple, robust storage of drops and fluids in a microfluidic device. *Lab on a Chip*. **2009**, *9*, 331-338.
24. Bithi, S. S.; Vanapalli, S. A. Behavior of a train of droplets in a fluidic network with hydrodynamic traps. *Biomicrofluidics*. **2010**, *4*, 044110.
25. Sun, M.; Bithi, S. S.; Vanapalli, S. A. Microfluidic static droplet arrays with tuneable gradients in material composition. *Lab on a Chip*. **2011**, *11*, 3949-3952.
26. Shim, J.; Cristobal, G.; Link, D. R.; Thorsen, T.; Fraden, S. Using Microfluidics to Decouple Nucleation and Growth of Protein Crystals *Crystal Growth & Design*. **2007**, *7*, 2192-2194.
27. Watson, J. M.; Baron, M. G. The behaviour of water in poly(dimethylsiloxane). *Journal of Membrane Science*. **1996**, *110*, 47-57.
28. Shim, J.; Cristobal, G.; Link, D. R.; Thorsen, T.; Jia, Y.; Piattelli, K.; Fraden, S. Control and Measurement of the Phase Behavior of Aqueous Solutions Using Microfluidics. *Journal of the American Chemical Society*. **2007**, *129*, 8825-8835.
29. Shim, J.; Patil, S. N.; Hodgkinson, J. T.; Bowden, S. D.; Spring, D. R.; Welch, M.; Huck, W. T. S.; Hollfelder, F.; Abell, C. Controlling the contents of microdroplets by exploiting the permeability of PDMS. *Lab on a Chip*. **2011**, *11*, 1132-1137.
30. Salmon, J.-B.; Leng, J. Microfluidics for kinetic inspection of phase diagrams. *Comptes Rendus Chimie*. **2009**, *12*, 258-269.
31. Bird, R. B.; Stewart, W. E.; Lightfoot, E. N. *Transport Phenomena*, Wiley, 2007,
32. Randall, G. C.; Doyle, P. S. Permeation-driven flow in poly(dimethylsiloxane) microfluidic devices. *Proceedings of the National*

- Academy of Sciences of the United States of America*. **2005**, *102*, 10813-10818.
33. Verneuil, E.; Buguin, A.; Silberzan, P. Permeation-induced flows: Consequences for silicone-based microfluidics. *Europhysics Letters*. **2004**, *68*, 412-418.
 34. Lee, J. N.; Park, C.; Whitesides, G. M. Solvent Compatibility of Poly(dimethylsiloxane)-Based Microfluidic Devices. *Analytical Chemistry*. **2003**, *75*, 6544-6554.
 35. Sucrose Conversion Table - Technical Inspection Procedures. *United States Department of Agriculture*. 1981.

Chapter 6. Microfluidic Platform for the Characterization of Concentrating Electrostatically Stabilized Nanoparticle Suspensions

6.1. Introduction

Colloidal suspensions are present in many everyday applications, including food, personal care products, detergents, and paints. In the case of paints, the suspension is typically applied as a liquid and allowed to dry. The dehydration process affects the final structural properties and appearance of the dried suspension film. Bulk drying studies are thus valuable for identifying and understanding the microstructural and mechanical changes that occur within the concentrating suspension as the solvent phase evaporates. In addition, many factors affect the efficacy of a product over time, and suspension stability is an important aspect of the product performance. Additives such as salts and surfactants are commonly used to stabilize and increase the lifespan of a suspension, and storage conditions such as temperature and light are also taken into account. Destabilization of colloidal suspensions results in physical changes, such as increased turbidity, increased viscosity, and phase separation, and these changes are detectable using a variety of experimental methods including light scattering, small angle x-ray scattering, particle tracking, and rheology.¹⁻⁴

Dehydration of films of particle suspensions is governed by capillary and viscous forces, as well as the physiochemical properties of the solution. During the dehydration of a sessile drop containing a particle suspension, the particles within the suspension promote contact line pinning of the interface as the solvent

evaporates, and the particles move toward the air-solvent interface as the suspension concentrates. The pinning of the interface induces the flow of the particles to the edges of the drop.⁵⁻⁸ The particles at the interface form an incompressible solid, and sudden changes in particle concentration can be seen as a compaction front propagating from the drying edge.⁹ Water continues to flow through this solid region to replace the water that is lost from evaporation.^{5,9} Eventually, crack formation and delamination is observed as the solid continues to dehydrate.⁸⁻¹² During dehydration, the rheology of a suspension containing spherical particles progresses from viscous to elastic behavior, and eventually the suspension forms a brittle solid.^{4,9,13,14} The typical maximum particle concentration reported for dehydrating suspensions of spherical particles is a volume fraction $\phi \sim 0.63$, which corresponds to the limit for an ordered suspension.¹⁵⁻¹⁷

Gels will form at high particle concentrations during dehydration experiments,^{4,14,17,18} but can also form over time at constant particle concentration depending on the ionic strength of the suspension.^{1,17,19,20} The formation of a gel from silica suspensions is a function of a variety of parameters, including particle size, particle concentration, surface charge, and particle interactions.^{17,19,20} The ionic strength of a particle suspension can be controlled by varying the pH of the suspension, thereby altering the surface charge of the particles, or by adding salt to the suspension, which screens the particle surface charges and reduces the electrostatic repulsion. Both lead to the destabilization of the suspension as the particles flocculate, and eventually the suspension forms a space-filling

flocculated gel. The focus of the experiments presented in this chapter will be to use the dehydrating droplets in array devices to demonstrate and control the effect of ionic strength on the flocculation phenomenon.

Aggregation of hard sphere suspensions has been examined in detail previously. The rate of aggregation can be described by the stability ratio W , defined as the ratio of the rate of aggregation of dimers in the diffusion limit to the actual aggregation rate. W strongly depends on salt concentration below a critical concentration n_{crit} given by

$$n_{crit} = 9.0 \left(\frac{kT}{A_{eff}} \right)^{2/3} \left(\frac{ql_b^2}{e} \right)^{4/3} \quad (6.1)$$

where k is the Boltzmann constant, T is the temperature, A_{eff}/kT is the Hamaker constant, and q is the charge density. The parameter l_b is the Bjerrum length given by

$$l_b = \frac{e^2}{4\pi\epsilon\epsilon_0 kT},$$

where ϵ is the permittivity of the medium, ϵ_0 is the permittivity of a vacuum, and e is the electron charge. Below n_{crit} , the stability ratio decreases monotonically with increasing salt concentration. Above n_{crit} , the stability ratio approaches a minimum value that is independent of the salt concentration. Eq. (6.1) shows that the suspension stability is sensitive to any changes in charge or concentration.^{17,19}

Experimentally, the flocculation or gelation time can be probed by measuring the conditions at which the suspension properties change significantly. The effect of added salt on the flocculation time has been examined using rheological measurements where the gelation time is defined as the crossover time

of the storage and loss moduli. The suspension first exhibits viscous behavior and transitions to elastic behavior as the particles flocculate and the suspensions gels. These experiments have shown that the flocculation time decreases as the silica concentration increases for a constant salt concentration; the flocculation time also decreases with increasing salt concentration for a constant silica concentration. The addition of the salt only affects the time at which the suspension gels; the strength of the final gel remains unaffected.^{1,17}

Microfluidic techniques have also been used to study the dehydration and gelation of silica suspensions.^{11,21,22} Merlin *et al.* perform experiments in PDMS microchannels that exploit the permeability of the device material to dehydrate colloidal suspensions up to a concentration at which colloidal crystals form. The setup is similar to the unidirectional drying studies conducted in capillary devices, but dehydration occurs primarily in a direction perpendicular to the direction of the suspension concentration gradient. The authors show that the dehydration rate and the design of the microfluidic channels that confine the suspension can be used to tune the appearance and properties of the colloidal crystal.¹¹ Shirk *et al.* use microfluidic techniques to form double emulsions droplets with the silica suspensions comprising the innermost phase. In this case, colloidal crystals are obtained by dehydrating the suspensions through the silicone oil shell of the droplet. The ionic strength influences the ability to form colloidal silica crystals.²²

Particle tracking can be used in place of bulk rheological measurements to probe fluid property changes in the small sample sizes that are characteristic of microfluidic techniques.²³⁻²⁹ Tracer particles of the order of hundreds of

nanometers to a few micrometers in size are introduced into the fluid suspension of interest at dilute concentrations typically of the order of 0.05% solids in solution.²⁴ At such dilute concentrations, the tracer particles are not expected to alter the suspension properties. A microscope and camera are used to image and record the position of the tracer particles. High spatial resolution, proper illumination, acquisition frame rate, and acquisition time can all be tuned to accurately capture tracer particle movement within a given sample. The images are then analyzed to obtain the trajectories of the tracer particles and the mean square displacement (MSD) of the particles is analyzed.³⁰⁻³³ Experimentally, the MSDs of many particles are used to obtain an ensemble-average of the MSD, which is then used to calculate quantities such as viscosity and modulus. For example, the effective diffusion coefficient D of a spherical tracer particle in a purely viscous medium undergoing a random walk can be calculated from

$$\langle x^2 \rangle = 4D\tau \quad (6.2)$$

for two-dimensional diffusion where $\langle x^2 \rangle$ is the mean square displacement and τ is the time step. Using the Stokes-Einstein relation, the effective viscosity of the fluid is estimated from

$$\eta_{eff} = \frac{dkT}{3\pi a \langle x^2 \rangle} \tau \quad (6.3)$$

where d is the number of dimensions, k is the Boltzmann constant, T is temperature, and a is the tracer particle radius.³³ Eqs. (6.2) and (6.3) together can be used to estimate the viscosity of a suspension from the measured MSD values.

In this chapter, the microfluidic platform described and characterized in the Chapter 5 is used to study the dehydration and stability of particle suspensions. Droplets containing silica or clay suspensions are fully dehydrated, and the final particle concentration is measured as a function of relative humidity and salt concentration. Particle tracking is used to probe changes in the fluid properties of the silica suspensions over time. For this part of the study, dehydration is arrested at a desired particle concentration, and the effect of salt concentration on the suspension stability is monitored through fluorescent tracer particle movement.

6.2. Materials and Methods

Silica suspensions are prepared by diluting Ludox TM-40 particles, which are spherical with diameter $2a = 22$ nm (Sigma Aldrich), with deionized water to the desired concentration. Initial concentrations of 5, 10, 20, 30 and 40 wt. % are used in the microfluidic experiments; 8 wt. % is used in the bulk rheological measurements. Clay suspensions of 1 wt. % are prepared by adding Laponite XLG particles, which are disk-shaped with diameter $2a = 25$ nm and thickness $h \sim 1$ nm (Southern Clay Products), to deionized water. All silica suspensions are sonicated (Cole-Parmer One-Pint Compact Ultrasonic Cleaner) for at least 10 minutes; clay suspensions are sonicated for at least 30 minutes or until the suspension appears clear. Droplets are formed in either light mineral oil (“MO”, Fisher Scientific) or 100 cSt silicone oil (“SO”, Gelest, Inc.).

To study the effect of salt on the dehydration and stability of the suspensions, a stock of solution of 2.0 M sodium chloride is prepared by dissolving salt (> 99%, Fisher Scientific) in deionized water. The salt solution is diluted as needed before addition to a suspension to minimize shock to the particle suspension. Initial salt concentrations of 100, 200, 270, and 400 mM are prepared with 5 wt. % Ludox TM suspensions for the microfluidic experiments. Suspensions containing 8 wt. % Ludox TM are prepared with 170, 320, 430, and 630mM NaCl for bulk rheological measurements to mimic the final droplet concentrations in the microfluidics experiments. All silica-salt suspensions are sonicated for at least 10 minutes and monitored immediately following sonication.

Droplets containing particle suspensions are formed using the same protocol described in Chapter 5 for generating droplet arrays in a microfluidic device. The humidity control chamber described in Section 5.2 is used for the experiments that involve the full dehydration of particle suspensions at 5, 25, 50, and 75% relative humidities. Partial dehydration of particle suspensions is achieved by dehydrating the droplets at a relative humidity of 5-10% for two hours to attain a desired particle concentration. The devices are then submerged in a Petri dish filled with water for the remainder of the experiment (12 hours to 12 days) to stop dehydration and to allow the suspensions to flocculate at a fixed composition.

Sulfate-modified green fluorescent polystyrene tracer particles (diameter $2a = 3 \mu\text{m}$, G0300, 1% solids, Duke Scientific) are dispersed in the droplet phase to probe changes in fluid properties. The particles have an excitation wavelength

of 468 nm and an emission wavelength of 508 nm. The concentration of fluorescent particles added to the silica suspensions is approximately 1/5000 of the stock solution, to yield about 10-20 particles per droplet in the microfluidic array. Glycerol (Fisher Scientific) and water solutions from 0 to 70 wt. % are used to validate viscosity measurements.

Individual droplets are imaged in brightfield to obtain volume data using the protocol described in Chapter 5. The movement of the tracer particles is recorded using a camera (Vision Research Phantom v9.1) at frame rates between 10 and 30 fps for 900 frames. A 20X objective, an exposure time between 33 ms and 100 ms, and a 120W excitation light source (EXFO/Lumen Dynamics X-Cite 120Q) are used image the particles. Tracer particle trajectories are subsequently tracked using the ImageJ (National Institutes of Health) plugin Mosaic,³¹ and the mean square displacements (MSD) are calculated in MATLAB (Mathworks).

Two sets of particle tracking experiments are carried out with glycerol-water solutions. In the first of these, a thin layer of glycerol-water solution is sandwiched between two microscope slides separated by a ~1 mm thick spacer (“bulk” data). The second experiment is performed within the microfluidic droplet array. Droplets of glycerol-water solutions are created and stored within the device as previously described in Chapter 5 (“microchannel” data). Particle trajectories are converted to MSDs, and an effective viscosity is calculated using Eq. (6.3). Figure 6.1 is a plot of the measured effective viscosity as a function of the mass fraction of glycerol in the solution. The error bars are the standard deviation of the effective viscosity values calculated from five particle trajectories

for a given condition and technique. Both bulk and microchannel measurements agree with one another to within experimental uncertainty. In addition, both sets of measurements agree well with values previously reported in the literature for glycerol-water solutions.³⁴

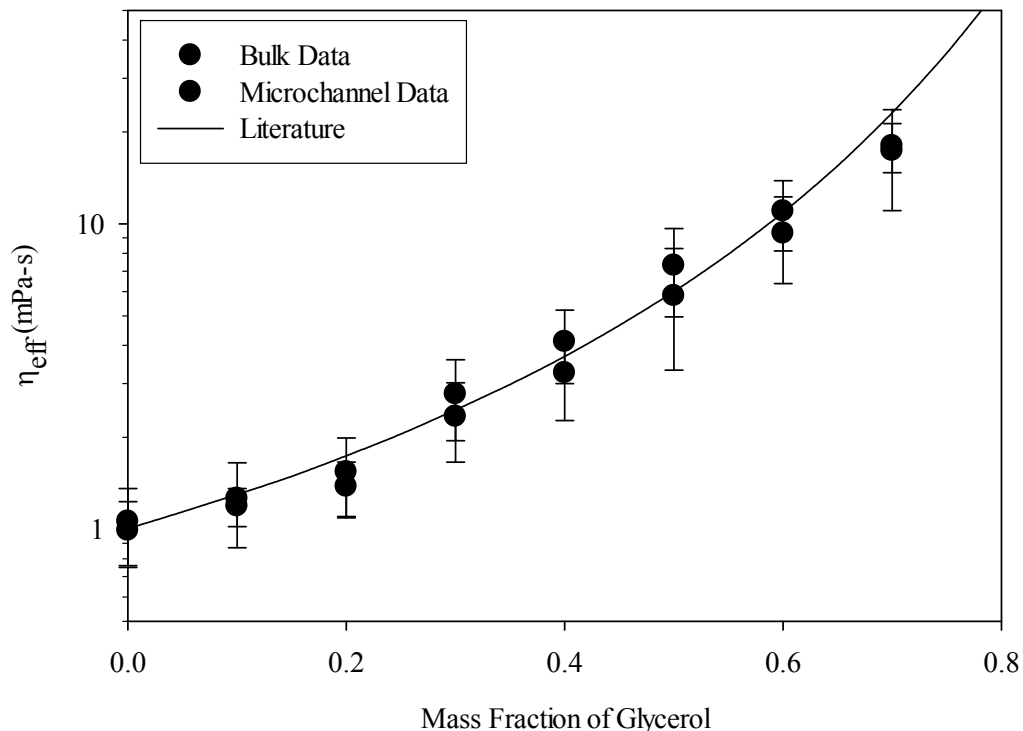


Figure 6.1. Comparison of microrheological measurements conducted in trapped nanoliter droplets with those measured in a thin film of and predicted in the literature³⁴ for glycerol-water solutions of varying concentration.

The upper limit on the effective viscosity that can be probed using particle tracking depends on the operating parameters used to record particle motion. The particle must diffuse a distance greater than the detection resolution to distinguish between a real measurement and detector noise. Breedveld and Pine²⁵ estimate these limits as

$$\eta_{\max} = \frac{dk_B T}{3\pi a \delta^2} \tau \quad (6.4a)$$

$$G_{\max} = \frac{dk_B T}{3\pi a \delta^2} \quad (6.4b)$$

where η_{\max} is the maximum effective viscosity that can be probed, τ is the time step, δ is the spatial resolution, and G_{\max} is the maximum modulus that can be measured. The authors state that it is possible to achieve 0.1 pixel accuracy (given that the particle image is at least 5-10 CCD pixels and has a Gaussian intensity profile). The calibration factor for our Nikon Eclipse Ti-U microscope with a 20X objective and Vision Research Phantom v9.1 camera is 0.56 $\mu\text{m}/\text{pixel}$, so the spatial resolution in our system with a 0.1 pixel accuracy is $\delta = 0.056 \mu\text{m}$. The maximum viscosity η_{\max} and modulus G_{\max} are then $0.19\tau \text{ Pa}\cdot\text{s}$ and 0.19 Pa , respectively. The maximum viscosity thus depends on the amount of time that the particle trajectory is sampled. The maximum material properties can also be improved by decreasing the probe particle size, increasing the objective magnification, or increasing the image resolution. There is also an upper limit on the maximum amount of time that a tracer particle will remain in the field of view in the case that the effective viscosity is low and diffusion is fast. The maximum lag time τ_{\max} is defined as

$$\tau_{\max} = \frac{3\pi a d_f^2 \eta}{2k_B T} \quad (6.5)$$

where d_f is the depth of focus, which depends on the microscope objective parameters. For the microscope used in the present experiments, the depth of field is $6 \mu\text{m}$. For pure water, the maximum lag time τ_{\max} is approximately 60 s.

Macroscale rheological measurements are also used to probe the suspension mechanical properties during the gelation process. A stress-controlled rheometer (TA Instruments TA D-HR 2) with a cone and plate geometry (1°, 40 mm) is used to probe suspensions with the same composition as that of the final composition achieved within the droplets. The temperature is held fixed at 25°C using a Peltier unit. The samples containing 430 and 630 mM NaCl are loaded onto the Peltier plate immediately after preparation, while the two samples containing 170 and 320 mM are prepared and stored for 2 or 8 days, respectively, prior to loading. To prevent evaporation, a small amount of mineral oil is placed around the sample, covering any exposed free surfaces. The complex modulus of each of the silica suspensions containing 320, 430, and 630 mM NaCl is measured by applying a continuous strain of $\gamma = 0.5\%$ and a frequency of 1 rad/s until the samples approach a steady state modulus value. The suspension containing 170 mM NaCl is sampled in three separate measurements lasting 5 days each. The time required to probe each sample varies from 8 hours (630 mM NaCl) to several weeks (170 mM NaCl). In the analysis, the start time is set to the point when the salt is added to the sample prior to sonication, which is approximately 20 minutes prior to the start of the complex modulus measurement.

6.3.Results

Fig. 6.2 shows the total time required to fully dehydrate droplets containing silica suspensions in the microfluidic array as a function of relative humidity. There are four sets of points shown, which include the arrays of

droplets containing water (●), 1 mM NaCl (■), 100 mM NaCl (▲), and silica (◆). The first three systems are included from Fig. 5.12 for comparison. The experimental end time for silica suspensions is defined as the time at which 75% of the droplets imaged achieve a constant droplet volume with time. Only droplets of pure silica with an initial concentration corresponding to $\phi_i = 0.02$ are tested for these experiments. An increase in the relative humidity leads to an increase in the total time required to fully dehydrate the droplets containing silica suspensions. The trend observed for silica suspension droplets agrees with the behavior exhibited previously for droplets containing water and salt.

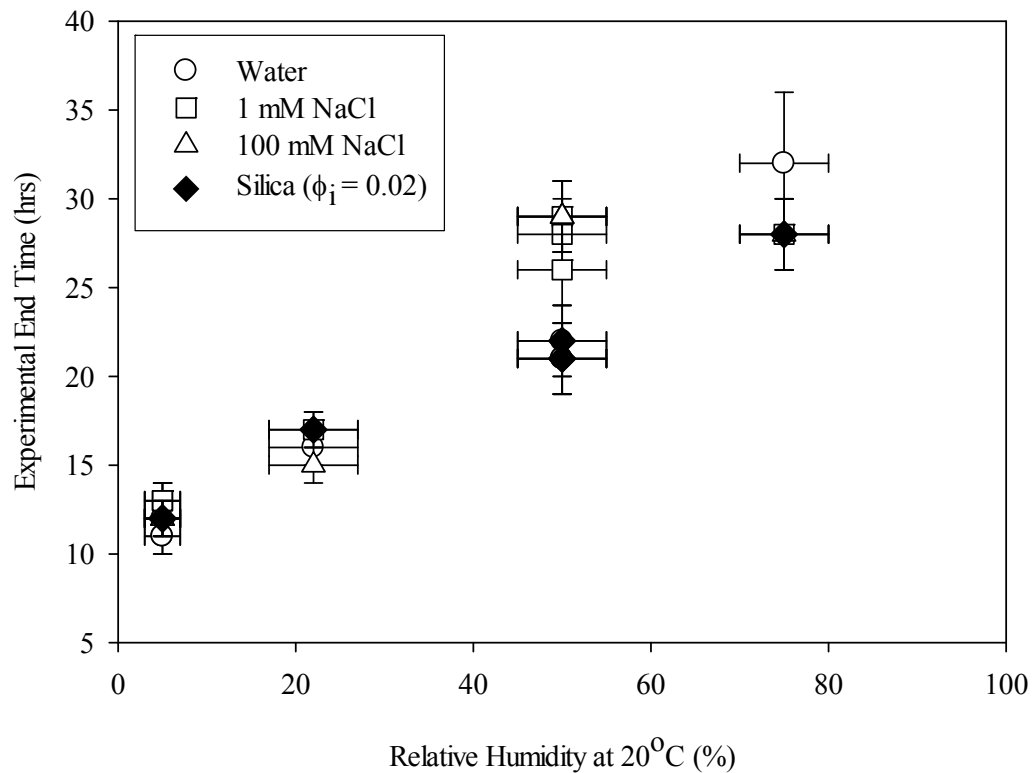


Figure 6.2. Time for 75% of the droplets sampled within an array to reach the final state (water – complete dehydration of droplet, NaCl – crystallization, silica – no volume change). All concentrations given refer to the initial concentration of the droplet.

Fig. 6.3 shows the final silica concentration of the dehydrated droplets as a function of the relative humidity. Each final concentration is calculated from the same experiments carried out for the experimental end times shown for Fig. 6.2. The final concentrations of these seven experiments are nearly independent of the relative humidity at which the droplets are dehydrated. The horizontal error bars are the maximum observed deviations in relative humidity observed at a given humidity, while the horizontal error bars are calculated from image pixilation; both errors are described in Chapter 5. The average final silica concentration $\phi_f = 0.63 \pm 0.03$ is indicated by the dashed line in Fig 6.3. This final silica concentration is consistent with the volume fraction corresponding to the random packing of hard spheres, suggesting that the droplets have stopped dehydrating due to a mechanical limit.¹⁵⁻¹⁷

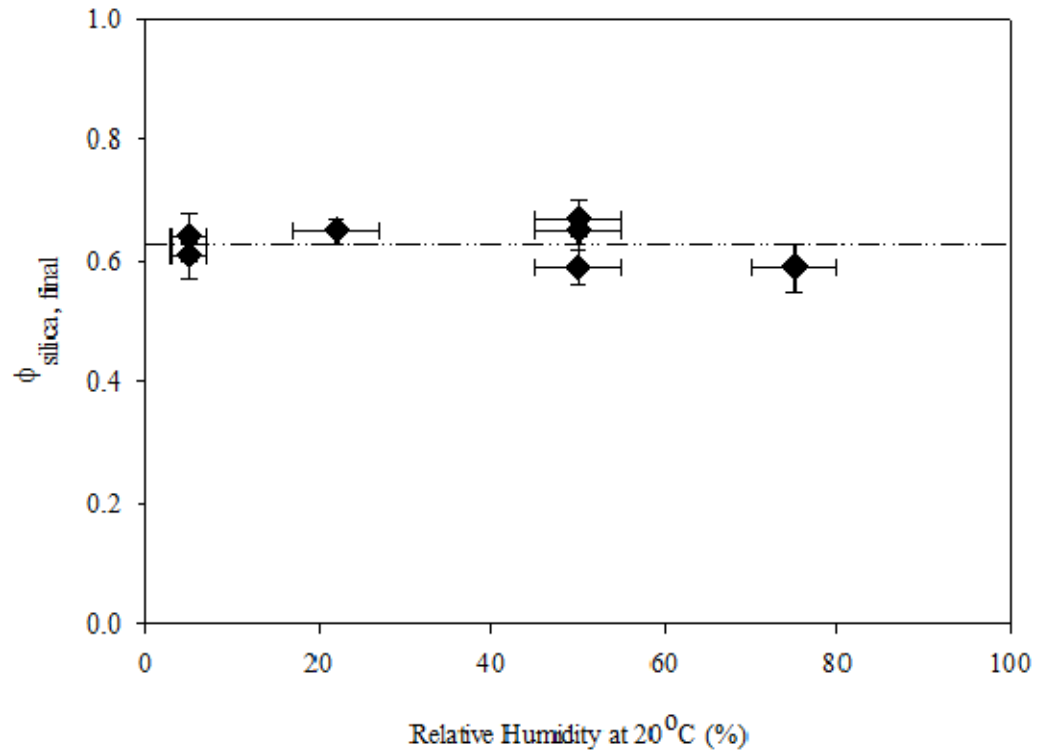


Figure 6.3. Final silica concentration as a function of relative humidity. The initial silica concentration for all experiments is $\phi_i = 0.02$.

Fig. 6.4 is a plot of final silica concentration versus initial silica concentration. The type of continuous phase oil, the presence of salt, and the initial concentration of salt are also varied for these experiments. The filled symbols correspond to the dehydration of pure silica suspensions, while the open symbols refer to the experiments with salt. The different shapes of the symbols are used to distinguish between different initial compositions of silica and salt. The solid line at $\phi = 0.50$ is the maximum silica concentration for a disordered suspension; the dashed line at $\phi = 0.55$ is the minimum silica concentration for an ordered suspension. The region between these two limits is a coexistence regime.¹⁷

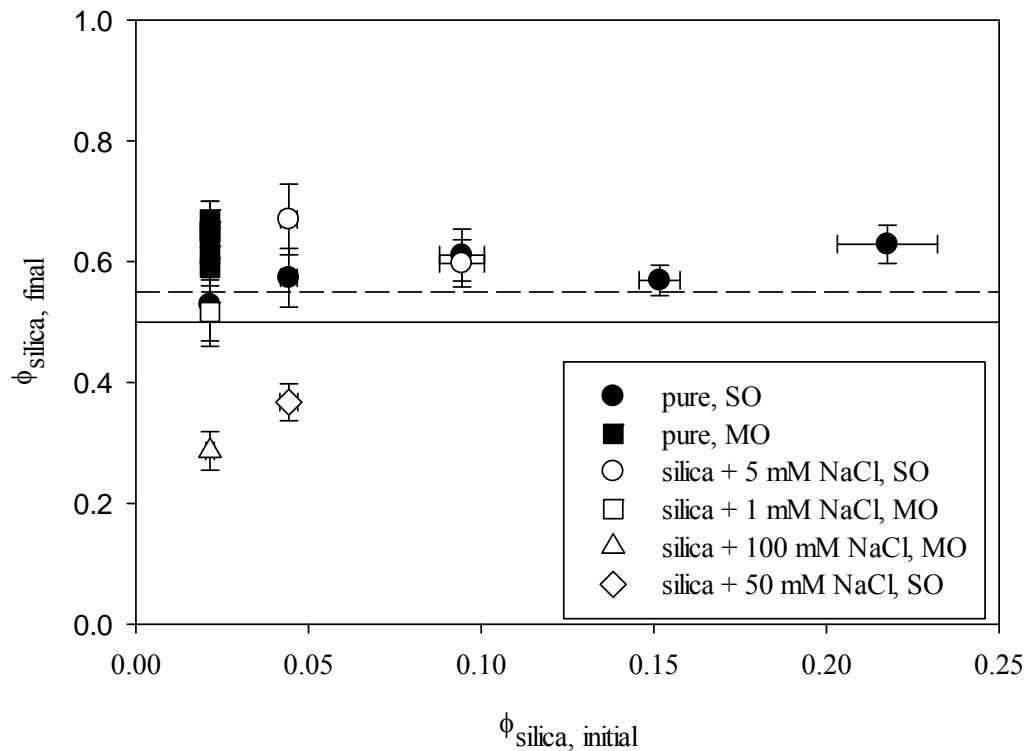


Figure 6.4. Final silica concentration as a function of initial silica concentration and added NaCl, including cases that exhibited formation of a dark mass at higher salt concentrations. All experiments are carried out at 5-10% humidity.

Fig. 6.4 shows that the droplets containing only silica (filled symbols) at varying initial concentrations dehydrated to the same final concentration. The dehydration experiments with droplets containing silica with different initial salt concentrations are shown as open symbols and exhibit two types of behavior. At low (< 5 mM) initial concentrations of NaCl, the added salt has no effect on the final silica concentration of the droplets. In all of these cases, the droplets stop shrinking at an average final silica volume fraction of $\phi_f = 0.59 \pm 0.08$. However, at higher initial salt concentrations (> 50 mM), the final silica concentration is significantly lower and depends on the initial composition of the droplet.

Visually, the dehydrating droplets with and without high concentrations of salt undergo strikingly different behaviors. Droplet dehydration in the microfluidic platform undergoes a two-stage drying process. As the image sequence of Fig. 6.5 shows, water diffuses out of the droplet in the first stage, and progresses through the expected shape transitions described in Chapter 5. More specifically, the droplet deforms to fit into the confines of the trap and attains a slug shape immediately after droplet formation (Fig. 6.5a). As the droplet dehydrates, the droplet shape transitions to a circular pancake shape (Fig. 6.5b-d) and finally a sphere (Fig. 6.5e-f). The droplet contents appear optically homogenous throughout the dehydration process, and no cracks or irregularities are observed. In Chapter 5, it is shown that diffusion out of the droplet follows the relationship $r \sim t^{1/2}$ where r is the effective spherical radius of the droplet and t is time. This relationship is also exhibited by the droplets containing silica suspensions. However, a closer look at Fig. 6.5e-f shows that the droplet undergoes a second drying regime where there appears to be a concentration gradient within the droplet.

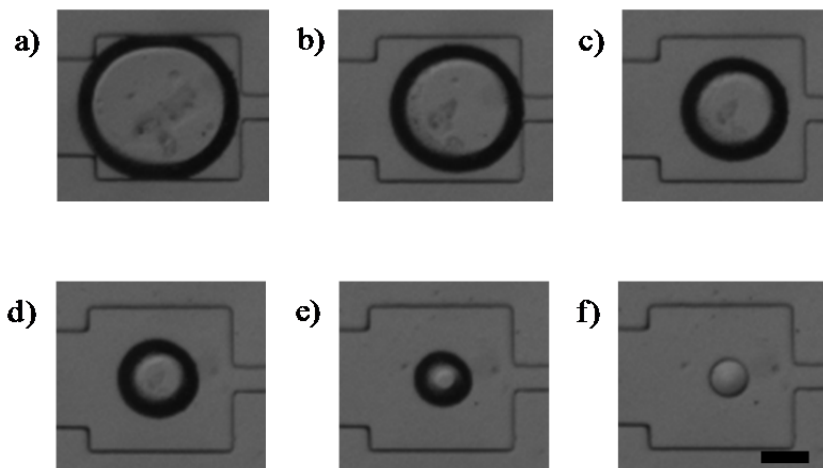


Figure 6.5. Dehydration of a trapped droplet containing a silica suspension ($2a = 22\text{nm}$, $\phi_i = 0.02$) over 10 hours. Two hours have elapsed between each image from a) to f). Scale bar is $100\ \mu\text{m}$.

Fig. 6.6 shows the formation of a “front” moving radially through the droplet, which occurs beginning at approximately 9.8 hours after the initial formation of the droplet array. In Fig 6.6a, the droplet still appears optically homogeneous. As seen in Fig. 6.6b, a refractive index difference is observed within the droplet approximately two minutes later. The dark line corresponding to this visual change in the droplet properties is referred to as a “front”. Fig. 6.6c-e show that the front proceeds to shrink radially for another 15 minutes until it completely disappears. While the front is present within the droplet, there is no detectable change in the overall droplet volume.

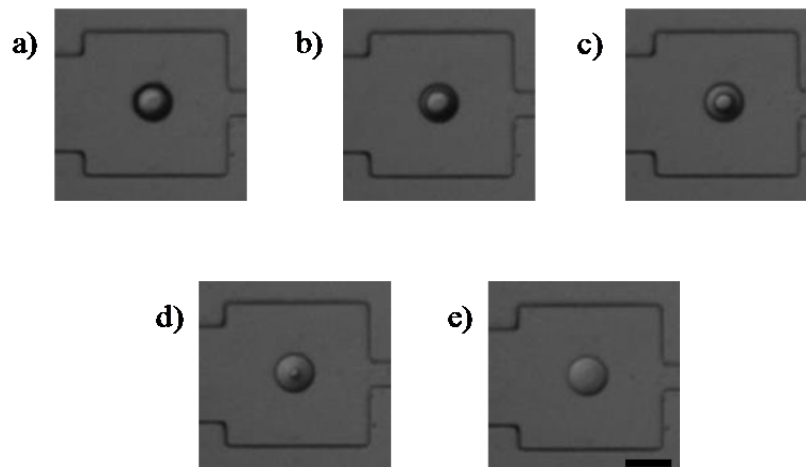


Figure 6.6. A "front" is observed to move radially from the outer edge of the droplet to the center in highly concentrated silica suspensions ($\phi_i = 0.02$). Approximately 20 minutes have elapsed between a) to e). Scale bar is 100 μm .

Fig. 6.7 plots the radius of the droplet front as a function of time with the initial time t_o set to one frame prior to the appearance of the front. Fig. 6.6 indicates that the front progresses from the outer edge of the droplet to the center in a spherically symmetrical manner, so the same protocol discussed in Chapter 5 to measure circular pancake droplet volumes is used to measure the progression of

the front. The low resolution of the images introduces a large amount of uncertainty due to image pixilation, so the resulting plot produces a rough estimate of the size of the front at each instant in time t . The radius of the front appears to decrease approximately linearly over a duration of approximately 20 minutes.

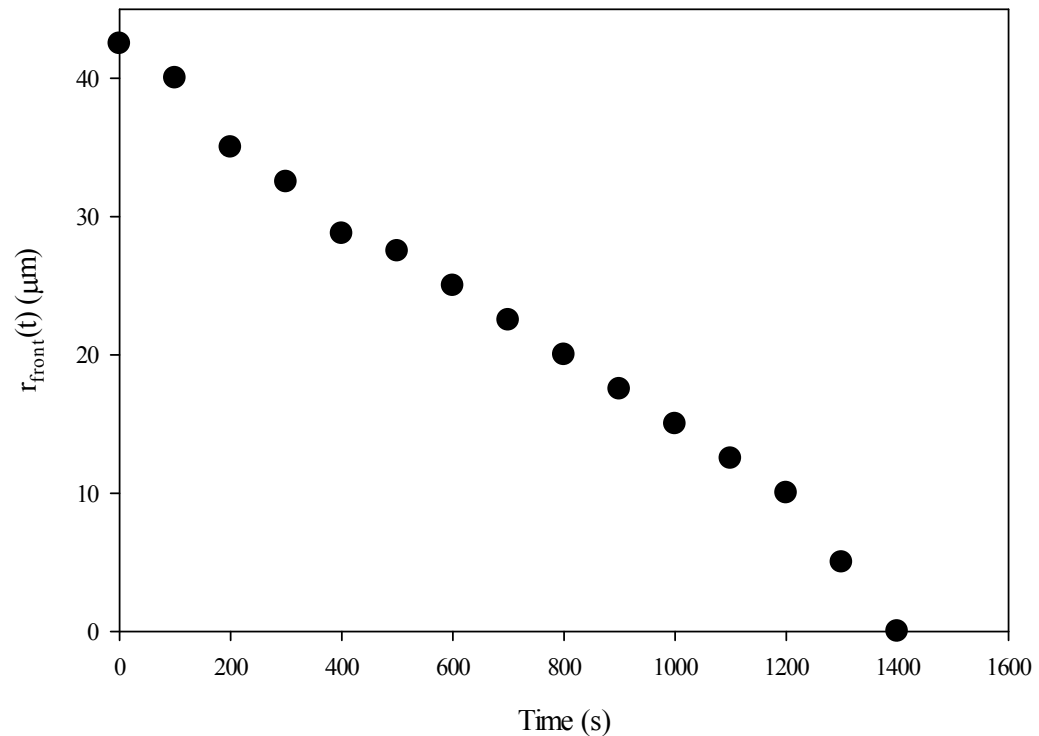


Figure 6.7. Decrease in radius of the “front” observed in the second stage of drying for a silica suspension. The initial silica concentration is $\phi_i = 0.02$ and the front appears at 9.8 hours, corresponding to a silica concentration of $\phi_f = 0.60$.

There is no volume decrease immediately prior to, during, or following the front propagation that is detected, to within the resolution of the camera. The silica concentration is assumed to be constant based on this result. However, previous studies have reported that water continues to diffuse through a suspension after it has formed a soft solid, although there is no concurrent

movement of the colloidal solid.^{9,12,16} It is therefore possible that the front is associated with an abrupt change in particle volume fraction in the bulk phase. The progression time of the front is relatively constant regardless of the relative humidity, suggesting that the ambient conditions affect only the primary mass removal from the droplet in the first stage of dehydration and do not affect the second drying stage. It should be noted that the crack formation and delamination observed in typical bulk film drying studies are not observed in the droplet dehydration studies carried out in the microfluidic platform. The droplets containing silica suspensions appear to dehydrate homogeneously within the microfluidic platform, which is difficult to achieve in macroscale studies.

The images shown in Figs. 6.5 and 6.6 for the dehydration of a pure silica droplet are also representative the dehydration of a droplet with < 5 mM added NaCl. Fig 6.8a shows the concentration of silica (\bullet) and Na^+ (\square) over time for a droplet that contains an initial silica concentration $\phi_i = 0.02$ and initial salt concentration $[\text{Na}^+]_i = 3$ mM. The vertical dashed line indicates the time at which the front is first observed, which is approximately 12 hours. Note that the recorded time at which the front is first observed varies across droplets within the device from 10 to 12 hours at 5% relative humidity, but it is also subject to the image sampling frequency. Images are acquired every two minutes for the experiment shown in Fig. 6.6, while images are acquired once an hour for the experiment shown in Fig. 6.8, leading to a larger uncertainty in the time at which the front is first observed. Fig 6.8a shows that the concentrations of both the solutes increase over time. The final silica concentration $\phi_f = 0.52 \pm 0.06$, while

the final concentration of salt is $[\text{Na}^+]_f = 150 \pm 20$ mM. The salt concentration therefore remains low for the duration of the experiment. In comparison, Fig. 6.8a shows the concentration of silica and salt over time for a droplet that initially contained $\phi_i = 0.02$ and $[\text{Na}^+]_i = 102$ mM. The silica and salt concentrations increase over time, but the final concentrations of the components are significantly different from the lower salt case: the final silica concentration $\phi_f = 0.29 \pm 0.03$ and the final concentration of salt is $[\text{Na}^+]_f = 1.9 \pm 0.2$ M. The appearance of the front occurs at approximately the same time (~ 12 hours) and is marked in Fig. 6.8b with a vertical dashed line.

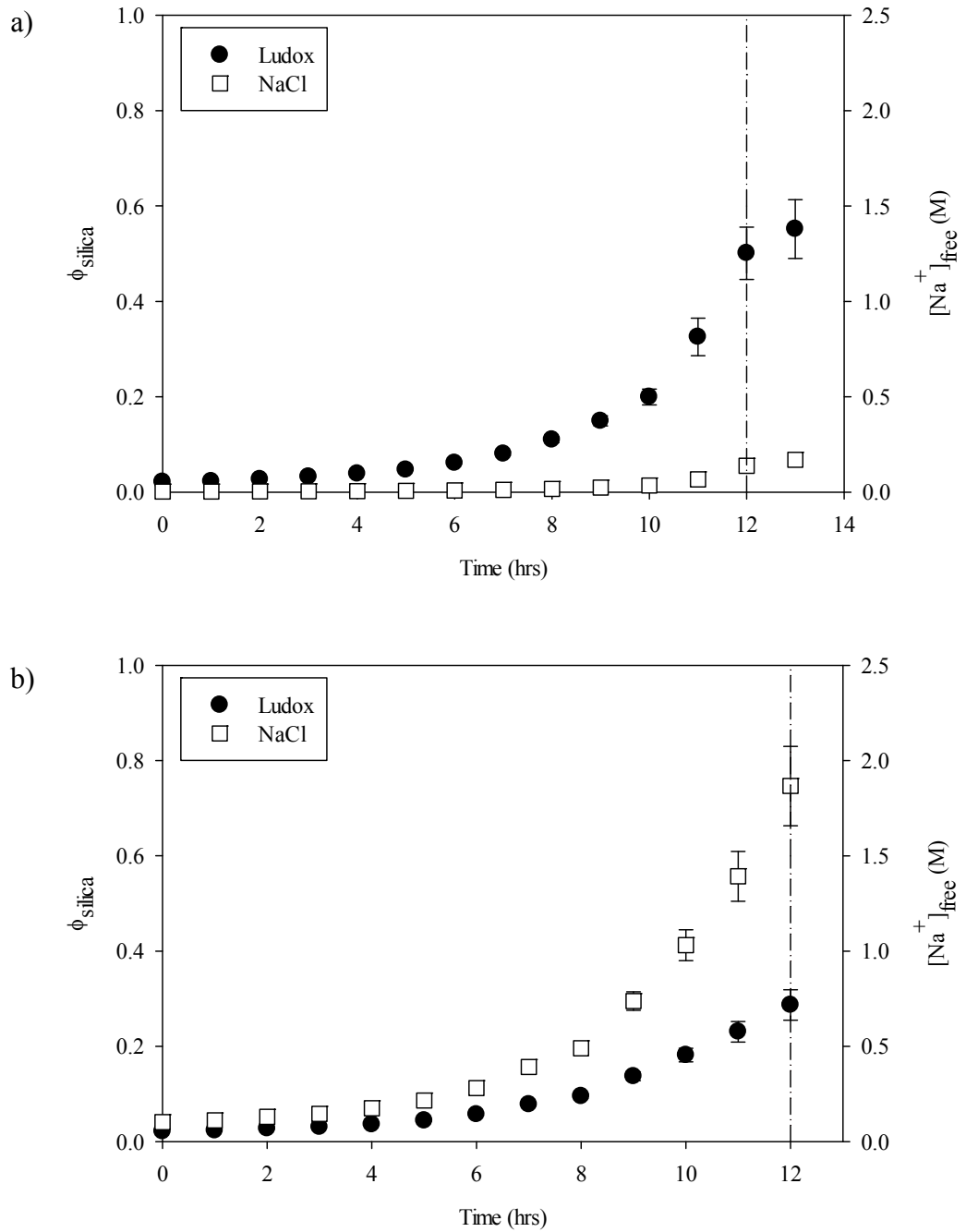


Figure 6.8. Concentration of silica and Na^+ as functions of time within a single droplet with a) $\phi_i = 0.02$ and $[\text{Na}^+]_i = 3 \text{ mM}$, and b) $\phi_i = 0.02$ and $[\text{Na}^+]_i = 102 \text{ mM}$. The front appears at approximately 12 hours for this particular drop. The dehydration occurs at 5% relative humidity.

Visually, the droplets containing higher initial concentrations of NaCl deviate from the low salt case in the second drying stage. As shown in Fig. 6.9a,

the onset of the second stage is marked by the appearance of a front within the drop. The droplet is also slightly larger ($\sim 100\ \mu\text{m}$) than the final droplet size for a droplet containing less salt ($\sim 85\ \mu\text{m}$), corresponding to the lower final concentration indicated in Fig. 6.8. The front progresses radially toward the center of the droplet (Fig. 6.9b), and eventually a darker mass forms within the droplet. Fig. 6.9c shows the formation of a darker material within the drop, and in subsequent images the droplet itself breaks apart while the front is still present. Completed front propagation is shown in Fig. 6.9d.

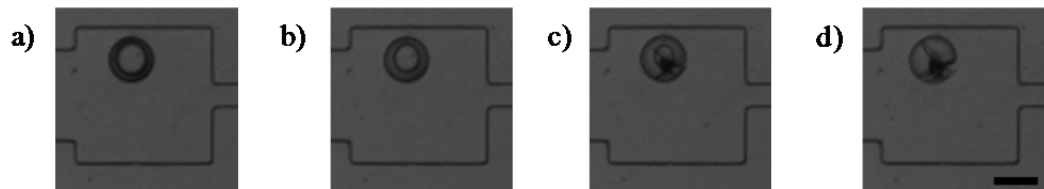


Figure 6.9. Similar to the case with no salt, a "front" is observed in highly concentrated silica and NaCl suspensions, but a second phase appears soon after the front appears. In this particular set of images, $\phi_i = 0.021$ and $[\text{NaCl}]_i = 100\ \text{mM}$. Approximately 8 minutes have elapsed between each image. Scale bar is $100\ \mu\text{m}$.

The appearance of the darker material within the droplet varies throughout the array and can be categorized into the three qualitative categories. Representative images of each category are shown in Fig. 6.10. In the first category of behaviors, the droplet remains intact and the second mass is completely encased within the final droplet (Fig. 6.10a). In the second category of behaviors, an intact droplet is observed with the second mass extruding from the droplet (Fig. 6.10b). The third category of structures involves the failure of the droplet at about the same time that the second mass appears (Figs. 6.9d and 6.10c). The extruded and exploded states are the most common final structures observed in these experiments, and comprise $>80\%$ of the final silica droplets.

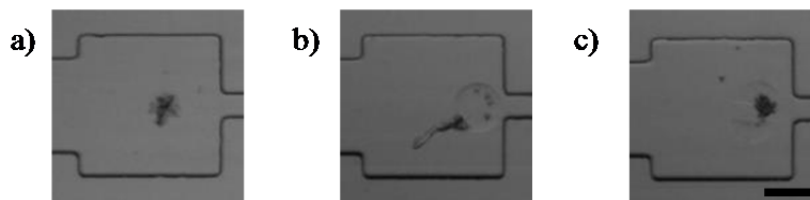


Figure 6.10. Final structures of dehydrated droplets containing silica and NaCl: a) encased, b) extruded, c) exploded. The final composition just prior to the appearance of the second phase is $\phi \sim 0.3$ and $[\text{NaCl}] \sim 2 \text{ M}$. Scale bar is $100 \mu\text{m}$.

Fig. 6.11 shows the evolution of the droplet size as a function of time for the protocol used in the stability suspension tests. The droplets are loaded at low concentrations of silica ($\phi_i = 0.02$) and salt ($< 400 \text{ mM}$) where flocculation is not expected to affect the droplet formation process in the microfluidic array. As seen in Fig 6.11 at $t = 2$ hours, the droplet has dehydrated to achieve a desired concentration of silica ($\phi \sim 0.03$) and salt. The device is submerged in a water bath immediately after this time point, and the droplet continues to dehydrate for a short time (~ 1 hour) after submersion. Once the system has equilibrated ($t = 4$ hours in Fig. 6.11), the droplet remains at a constant volume for at least two weeks; the first three days are shown in Fig. 6.11. Changes in fluid properties after the droplet volume has become constant are assumed to be attributed to changes in suspension stability rather than the dehydration/concentration process. The validity of this assumption will be discussed later.

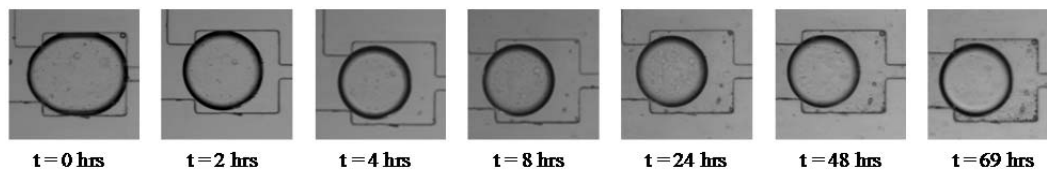


Figure 6.11. Long term storage of droplets containing a silica suspension that was submerged in a water bath at $t = 2$ hours. In these images, $\phi_i = 0.02$ and $[\text{NaCl}]_i = 100 \text{ mM}$, and $\phi_f = 0.03$ and $[\text{NaCl}]_f = 170 \text{ mM}$.

The stability of the silica suspension against flocculation has been extensively studied as a function of salt concentration. Silica nanoparticles flocculate over time when destabilized with salt, and the suspension eventually becomes turbid.¹⁷ Eq. (6.1) shows that the time required for flocculation to occur strongly depends on salt concentration for low salt concentrations (less than about 300 mM) of salt. However, the experimental images shown in Fig. 6.11 show a system that has reached this critical salt concentration and yet no changes in turbidity are observed in the microscope. The optical path length through the droplet is equal to the depth of the microchannel ($h = 100 \mu\text{m}$), which is too short to be able to detect intensity changes from turbidity. This is in contrast to bulk samples where the sample thickness is of the order of millimeters or greater. Fig. 6.12 shows that in bulk samples at these compositions, turbidity is evident. Since turbidity cannot be detected within the droplet, changes in suspension stability are instead probed by tracking the motion of fluorescent tracer particles.

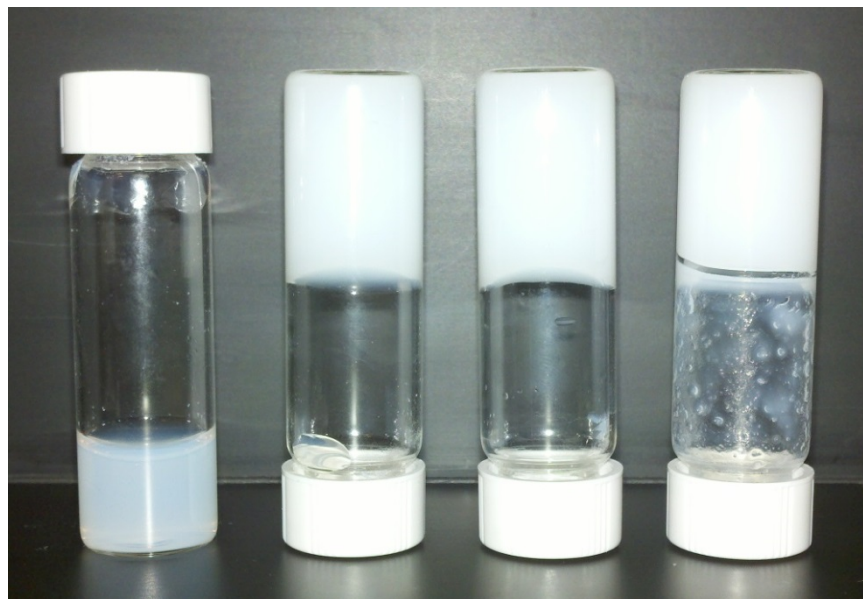


Figure 6.12. Turbidity is observed in bulk samples of silica suspensions containing salt at concentrations $[\text{NaCl}] = 170, 320, 430, \text{ and } 630 \text{ mM}$ from left to right.

The particle positions of fluorescent tracer particles within the droplets are recorded at regular intervals, and the mean square displacements of the particles are calculated from the particle trajectories. The fluid properties are sampled once every hour for the first 8 hours, and then once every six to 12 hours afterwards until a change in MSD is observed. The fluorescent tracer particle trajectories are then sampled more frequently to capture rapid changes in the fluid properties. Fig. 6.13 shows the evolution of the MSD within three droplets on separate devices corresponding to three different concentrations of NaCl including 170 mM (Fig. 6.13a), 320 mM (Fig. 6.13b), and 630 mM (Fig. 6.13c). The solid line indicates the expected trajectory calculated from Einstein's equation for the viscosity of a dilute spherical particle suspension. The slope of the MSD is initially equal to unity and similar to the predicted trajectory. Over time, the slope of the MSD curve decreases until the limit of the probe particle is reached ($\sim 3 \times 10^{-15} \text{ m}^2$). Trajectories plotted below this limit indicate that the tracer particles are able to probe the surrounding environment, but the displacement values are outside the detection limits of the current technique.

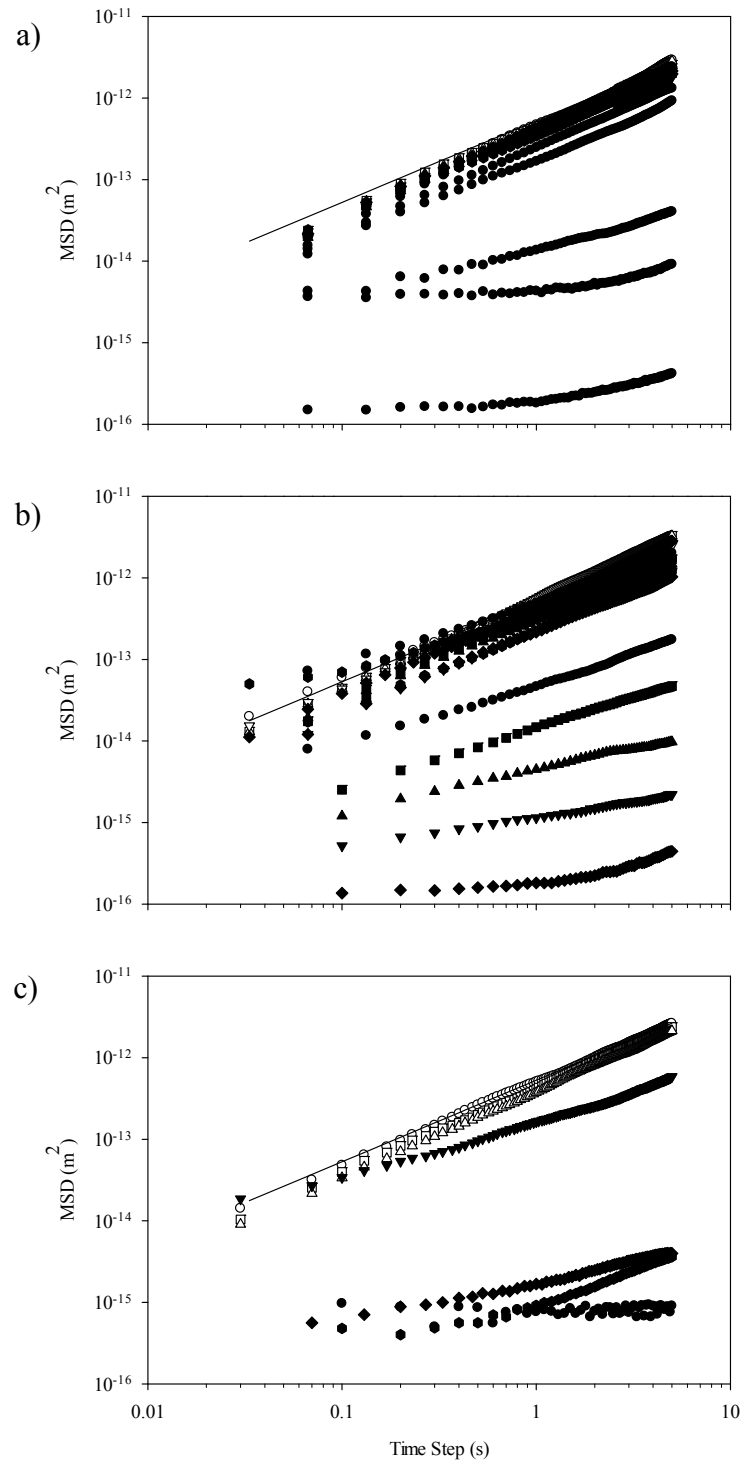


Figure 6.13. MSD for silica suspensions with concentrations of a) $\phi = 0.037$ and 170 mM NaCl, b) $\phi = 0.035$ and 320 mM NaCl, and c) $\phi = 0.033$ and 630 mM NaCl. Open symbols represent droplets that are dehydrating; filled symbols represent measurements taken after the device is submerged. The solid line is the effective viscosity of a dilute suspension of rigid spheres predicted by Einstein's formula. Time increases from top to bottom for each set of curves; the time elapsed is a) 286 hours, b) 117 hours and c) 10 hours.

The change in MSD observed in Fig. 6.13 is attributed to the flocculation of the silica particles. In Fig. 6.14, the effective viscosity η_{eff} of the droplet suspension is calculated from the MSD using Eq. (6.3) and plotted as a function of time for suspensions with a silica concentration of $\phi = 0.03$ and salt concentrations of 170 mM (●), 320 mM (■), 430 mM (▲), and 630 mM NaCl (◆). The droplet size is sampled along with the tracer particle movements at a given time to monitor the droplet composition corresponding to the fluid properties probed by the tracer particles. The initial time is taken to be the time at which the droplet has achieved a constant volume after dehydration. Because the initial silica concentration is kept constant and all experiments are carried out at the same relative humidity for the dehydration step, the start time for Fig 6.14 is taken to be one hour after the device is submerged in water. The effective viscosity η_{eff} exhibits a dramatic increase over a short time period. This time period depends on salt concentration, and Fig. 6.14 shows that an increase in the initial concentration of added salt leads to a faster rate of flocculation. The maximum effective viscosity is indicated by the dashed line in Fig. 6.14, which is calculated using $\tau = 5$ s to obtain $\eta_{max} = 0.95$ Pa·s. Any calculated viscosities that are plotted above this limit indicate that the probe particles are still able to diffuse through the flocculated suspension, but the measurement is beyond the accuracy of the operating conditions.

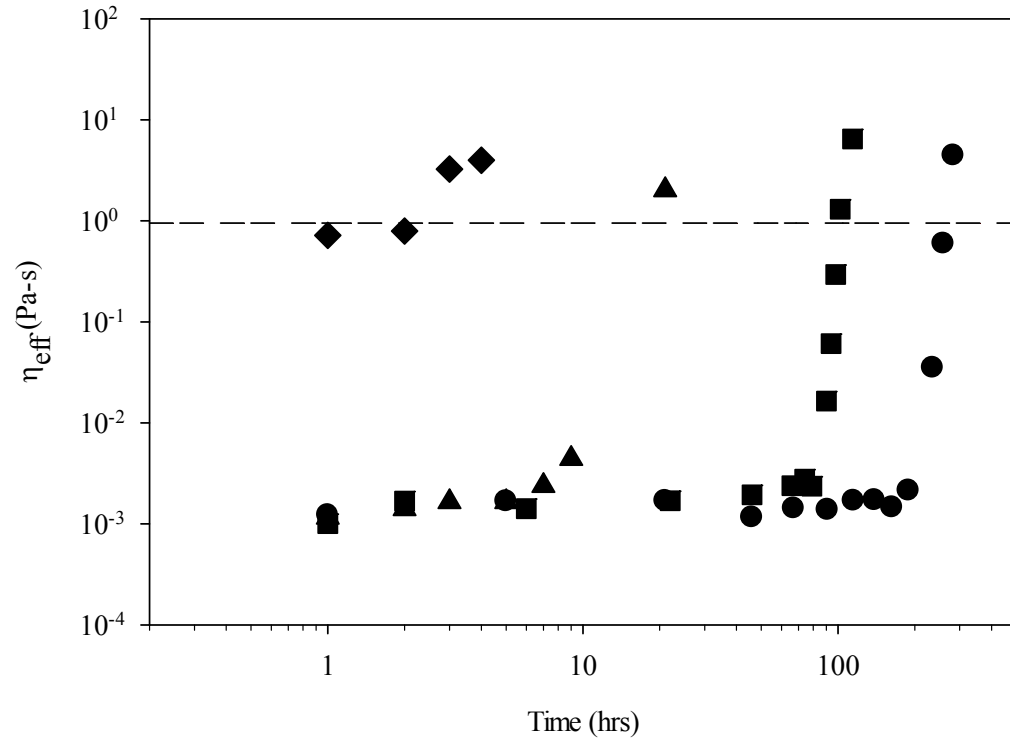


Figure 6.14. Effective viscosity of silica suspensions over time with salt concentrations of 170 mM (●), 320 mM (■), 430 mM (▲), and 630 mM (◆) NaCl. The dashed line indicates the maximum effective viscosity $\eta_{max} = 0.95$ Pa·s that can be probed with the current setup.

The reproducibility of the microfluidic platform to probe rapid changes in viscosity of a destabilized silica suspension is assessed by monitoring the tracer particle movement in several drops in different arrays at one particle suspension composition. Fig. 6.15 shows the calculated effective viscosity η_{eff} of the suspensions in five drops stored in two devices corresponding to an average droplet composition of $\phi = 0.03$ and $[\text{NaCl}] = 320$ mM. The plots show the same rapid increase in effective viscosity at approximately 90 hours for four out of five of the droplets. The droplet volume and fluid properties are probed either every 12 or 24 hours during this portion of the experiment until a change in the fluid properties is observed; the sample frequency increases to once every 4 hours

afterwards. One of the five droplets probed flocculates slightly earlier at $t_{\eta,crit} = 45$ hours, but otherwise particle flocculation appears to rapidly increase at a similar rate across different droplets and different devices.

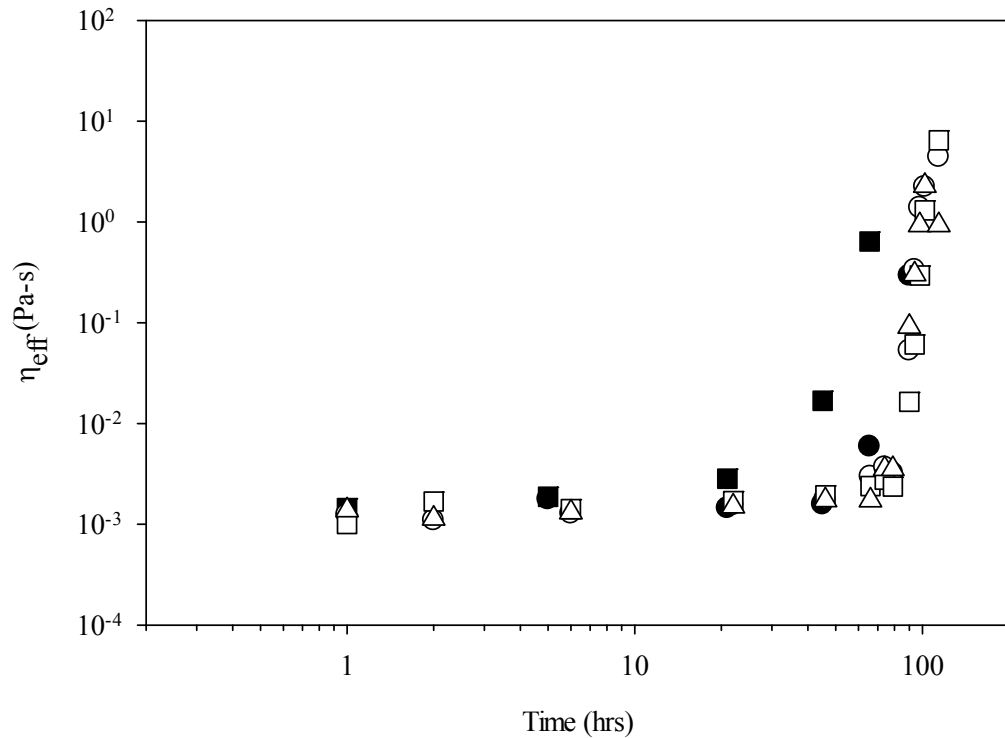


Figure 6.15. Effective viscosity of salted silica suspensions over time for several drops in different microfluidic devices at a single silica and NaCl concentration. The symbols correspond to the following systems: $\phi = 0.032 \pm 0.003$ and $[\text{NaCl}] = 310 \pm 30$ mM (\bullet); $\phi = 0.035 \pm 0.003$ and $[\text{NaCl}] = 330 \pm 30$ mM (\blacksquare); $\phi = 0.033 \pm 0.003$ and $[\text{NaCl}] = 310 \pm 30$ mM (\circ); $\phi = 0.032 \pm 0.003$ and $[\text{NaCl}] = 300 \pm 30$ mM (\square); and $\phi = 0.032 \pm 0.003$ and $[\text{NaCl}] = 310 \pm 30$ mM (Δ).

Bulk rheological measurements are carried out for comparison with the observations in the trapped droplets. Fig. 6.16 shows the complex modulus G^* of a sample containing silica with varying concentrations of salt over time. The applied frequency in these measurements is held fixed at 1 rad/s. The concentrations of the bulk samples are the same as the constant concentrations achieved in the microfluidic devices: the silica concentration is equal to $\phi = 0.03$,

and the salt concentrations are equal to 170 mM (\circ), 320 mM (\square), 430 mM (Δ), and 630 mM (\diamond). The start time for these experiments is defined as the time at which the salt is first added to the silica suspension. Fig. 6.16 shows a rapid increase in the complex modulus G^* with time as the suspensions destabilize and form a flocculated gel for the three salt concentrations corresponding to 320, 430, and 630 mM NaCl. A rapid increase in complex modulus is not observed at the lowest salt concentration $[\text{NaCl}] = 170$ mM, and fluctuates between 1-10 Pa, which is near the noise floor of the instrument (~ 1 Pa).

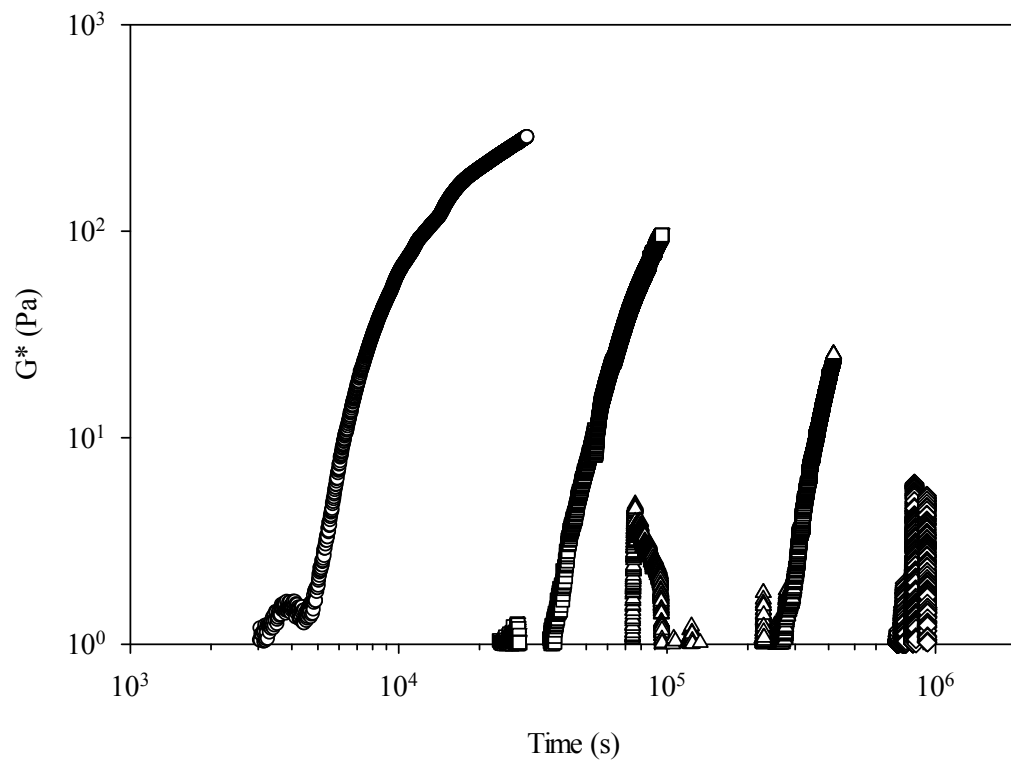


Figure 6.16. Complex modulus of the bulks samples of silica suspensions with added salt at an angular frequency of 1 rad/s. The silica concentration is equal to $\phi = 0.03$, and the salt concentrations are equal to 170 mM (\circ), 320 mM (\square), 430 mM (Δ), and 630 mM (\diamond).

A flocculation time can be extracted from both Figs. 6.14 and 6.16 to give an estimate of the dependence on salt concentration of the rate of flocculation. In

the measurements performed in the droplets, this time is equal to the time $t_{\eta,crit}$ at which the effective viscosity η_{eff} rises above 10^{-2} Pa·s. After this time, the viscosity increases rapidly on a log scale. The critical time for the bulk measurements is roughly estimated as the time at which the complex modulus $G^* > 10$ Pa, which is above the resolution of the measurement and any previously measured increases in the modulus. A plot of flocculation time versus salt concentration is shown in Fig. 6.17. The results obtained from particle tracking measurements are indicated with filled circles (\bullet), while the bulk rheological measurements are marked with open triangles (Δ). The flocculation times vary from one to 235 hours for final added salt concentrations corresponding to 630 to 170 mM NaCl. Fig. 6.17 shows that the flocculation time decreases as the concentration of salt increases. A dramatic increase in the complex modulus is not observed at the lowest salt concentration (170 mM NaCl), so no flocculation time is indicated for this case. The absence of a rapid viscosity increase in the bulk rheological measurement for the suspension containing 170 mM NaCl can be attributed to the different length scales sampled by the particle tracking technique and the rheometer. The tracer particles are able to sense the formation of small flocs that are present in the suspension, but if they have not formed a network spanning the entire sample, the rheometer will continue to sense a fluid exhibiting viscous behavior.

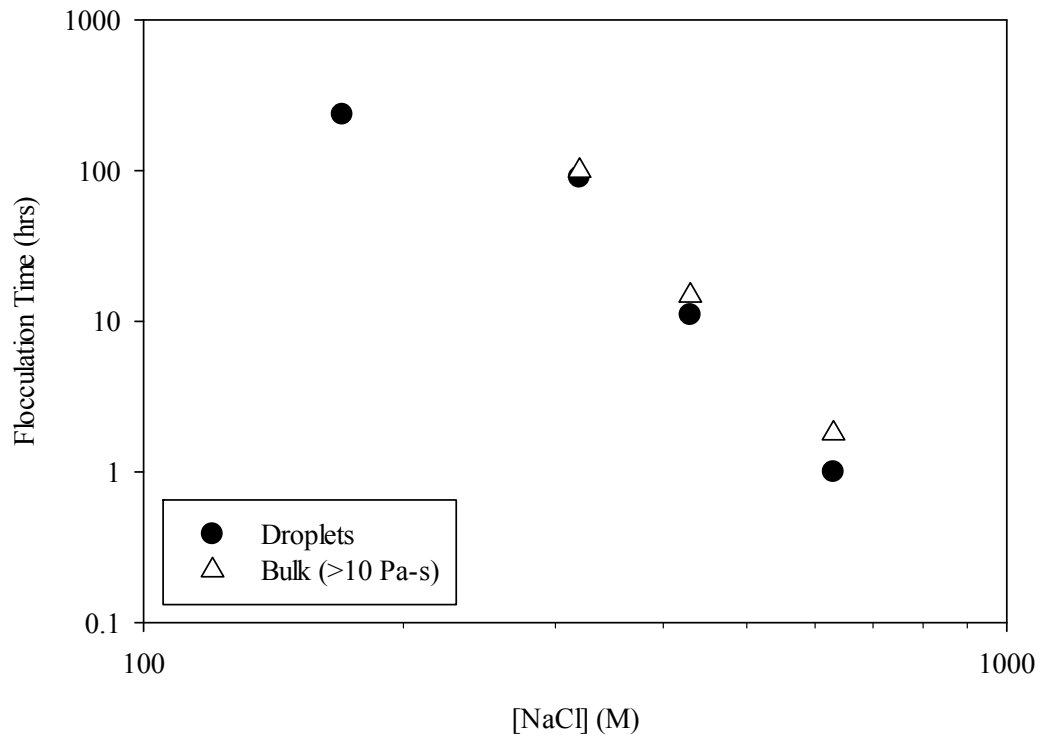


Figure 6.17. Effect of added salt concentration on flocculation time. The flocculation time in the droplets is defined as the time when $\eta_{eff} > 0.01$ Pa·s. The flocculation time in the bulk is defined as the time when $G^* > 10$ Pa.

The decrease in flocculation time with increasing salt concentration shown in Fig. 6.17 qualitatively agrees with the behavior of the stability ratio W , which is defined as the ratio of the rate of aggregation of dimers in the diffusion limit to the actual aggregation rate.¹⁷ A stable suspension exhibits a slow actual aggregation rate, which corresponds to a large stability ratio W . As salt concentration increases, the particles become increasingly electrostatically screened so the particles are able to move closer together. A smaller separation distance increases the aggregation rate of the particles and decreases the stability ratio W and the flocculation time as the salt concentration increases. The actual aggregation rate eventually approaches the diffusion-limited aggregation rate at a

critical salt concentration, which corresponds to the minimum stability ratio. At larger salt concentrations, the flocculation time is constant. The data shown in Fig 6.17 exhibits these general trends with salt concentration and indicates that there is good agreement between the two methods used to probe particle suspension stability for the suspensions with the three higher concentrations of salt (320, 430, and 630 mM). The agreement between the two types of measurements suggests that particle tracking in microfluidic devices can be used to provide a reasonable estimate of macroscale behavior and suspension stability.

The experiments presented thus far involve a model spherical nanoparticle with well-characterized suspension properties. For comparison, we also conducted preliminary dehydration experiments with suspensions composed of disk-shaped clay particles. The experimental end time for these particle suspensions is defined the same as for the silica suspensions and is the time at which the droplet has attained a constant droplet volume. Fig. 6.18 shows the experimental end time of drops containing clay suspensions (\blacktriangledown) as a function of relative humidity, plotted with the data previously shown for droplets containing water and salt solutions. The experimental end time increases with relative humidity as expected, but the clay suspensions dehydrate much more slowly than previously observed for pure water and NaCl droplets at higher humidities. The time required to dehydrate a 1 wt. % clay droplet in 50% humidity was over ten hours longer than that recorded for the other systems studied, and the dehydration time for a clay droplet held at 75% humidity was greater than 72 hours. No data point is included in

Fig. 6.18 because the experiment was removed from the humid environment prior to the complete dehydration of the drop.

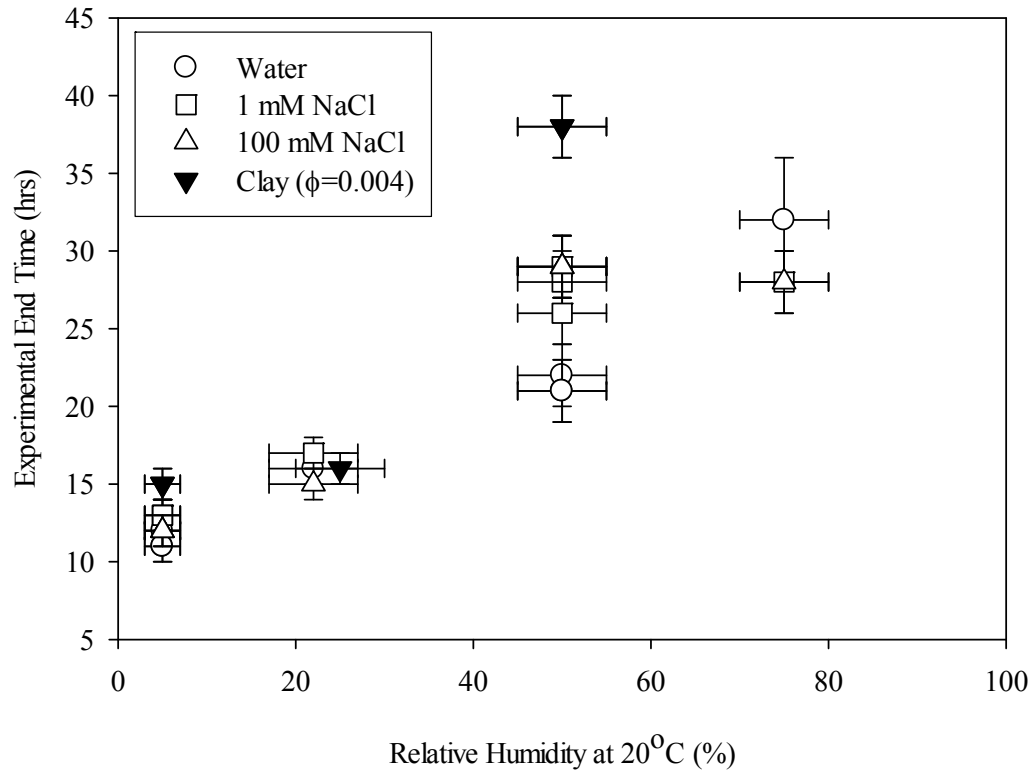


Figure 6.18. Time for 75% of the droplets sampled within an array to reach the final state (water – complete dehydration of droplet, NaCl – crystallization or no volume change, clay – no volume change). All concentrations given refer to the initial concentration of particles in the droplet.

The droplets containing clay suspensions also undergo a two stage dehydration process, and as shown in Fig. 6.19, exhibit the characteristic movement of the front in the second stage at a constant droplet volume. Fig. 6.19a shows a droplet containing a clay suspension dehydrating homogeneously until a front appears within the droplet (Fig. 6.19b); progresses through the droplet; and eventually disappears (Fig 6.19c). In the droplets containing silica suspension, the second stage of drying occurs in approximately 20 minutes for all experiments,

and the rate at which the front progresses through the droplet is independent of relative humidity. The second stage of drying in the clay suspension droplets, in contrast, depends on relative humidity, and the total time that is required for the front to progress through the droplet increases with an increase in humidity. At humidities below 25%, the internal dehydration time is about one hour. The time increases to 17 hours for 50% humidity, and is greater than 30 hours when the device is held at 75% humidity.

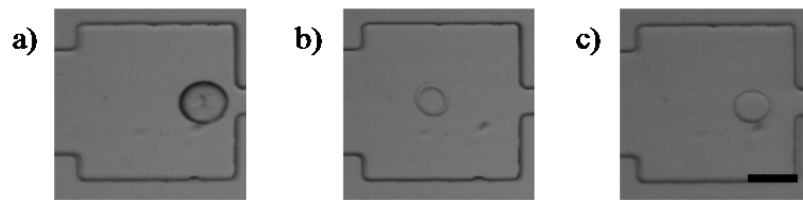


Figure 6.19. A "front" is observed in highly concentrated clay suspensions. In these images, $\phi_i = 0.004$, and the droplet was dehydrated at 5% relative humidity, however, the time required for the front to move through the drop varies with humidity. Scale bar is 100 μm .

Droplet volume analysis is less accurate with the clay suspensions. The diameter of the final droplet is smaller than the depth of the channel, which would normally indicate that the droplet has become spherical by the end of the dehydration time. However, the droplets containing suspensions of clay have instead retained the pancake shape attained from the earlier confinement in the channel (Fig. 6.20). The fully dehydrated drop with an initial concentration of $\phi_i = 0.004$ shown in Fig. 6.20 has a final drop diameter of 61 μm and a thickness of 27 μm . As a result, droplet volume measurements conducted between the initial and final volumes are only estimates, since the height of the droplet during the dehydration process cannot be measured systematically.

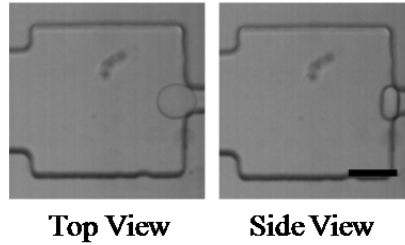


Figure 6.20. Top and side views of a dehydrated clay drop. The drop diameter is equal to $61\ \mu\text{m}$ and has a thickness of $27\ \mu\text{m}$. The depth of the channel is $h = 100\ \mu\text{m}$. Scale bar is $100\ \mu\text{m}$.

Fig. 6.21 shows the final concentration of clay particles as a function of relative humidity. Two sets of experiments are compared corresponding to pure clay suspensions with $\phi_i = 0.004$ (\bullet) and clay with salt at an initial concentration $[\text{NaCl}]_i = 1\ \text{mM}$ (\circ). The final concentration is independent of dehydration rate and is on average equal to $\phi_f = 0.40 \pm 0.04$. This value is significantly higher than previously reported (up to 6 wt. % or $\phi = 0.02$).³⁵⁻³⁷ Taking into the account the final droplet shape, the drop volume analysis shows that 99% of the volume is lost during the course of the experiment. Preliminary experiments show that additional salt has no significant effect on the dehydration of and the final concentration and appearance of the droplets containing clay suspensions (Fig. 6.21).

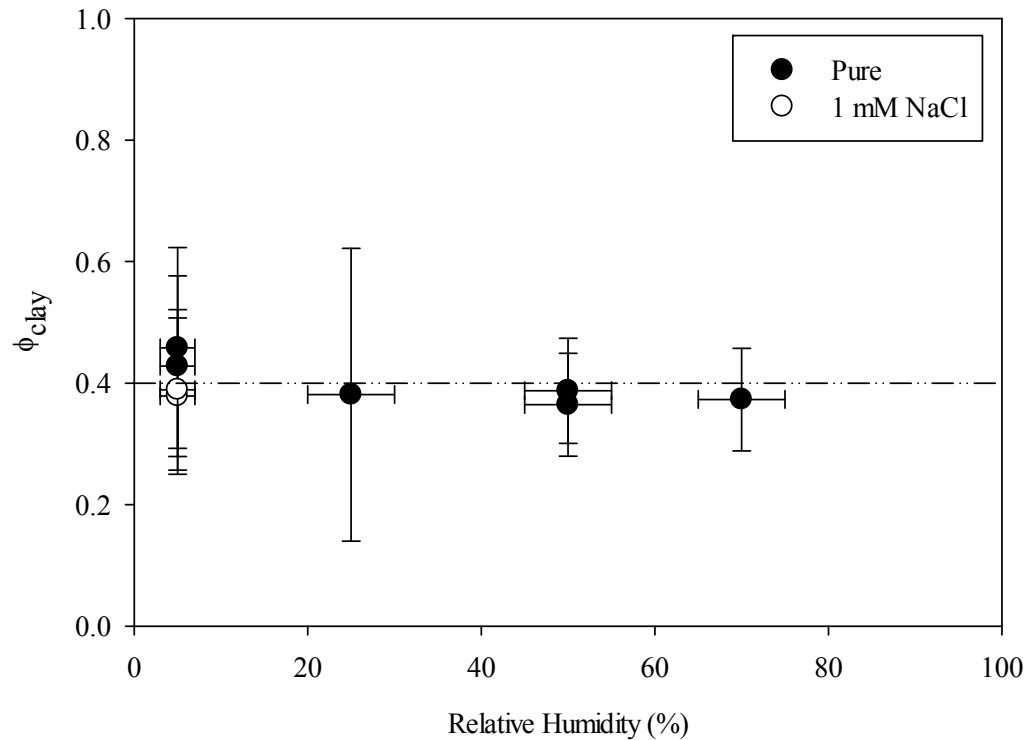


Figure 6.21. Final clay concentration in drops containing clay suspensions as a function of relative humidity, with (●) and without (○) added salt. The initial clay concentration for all experiments is $\phi_i = 0.004$.

6.4. Discussion

The full dehydration of silica suspensions with varying amounts of salt will achieve a concentration at which the suspension becomes unstable since the concentration of the suspension is driven through composition transitions by mass transfer of water out of the droplet. The flocculation strongly depends on salt concentration and the dehydration rate of the droplet may be comparable to or greater than the flocculation rate of the particles due to added salt. At low initial concentrations of salt ($[\text{Na}^+]_i < 7 \text{ mM}$), the final concentration of salt is $[\text{Na}^+]_f < 310 \text{ mM}$. Fig. 6.17 suggests that a suspension with this salt concentration should require several days to flocculate. The flocculation time also depends on

particle concentration which is also increasing with time. The flocculation time is expected to decrease with increasing particle concentration. By comparison, the dehydration of the suspensions with higher concentrations of added salt leads to final salt concentrations of almost 2.0 M, as shown in Fig. 6.8b. Compared with the highest salt concentration studied in Fig. 6.17, the flocculation of a silica suspension with 2.0 M salt should be significantly less than an hour. These results taken together suggest that the droplet contents of the suspension shown in Fig. 6.8b most likely destabilize first and then continue to dehydrate to completion.

The formation of the dark material observed in Fig. 6.9 for suspensions containing high salt concentrations may result from the decrease of water in the droplet during the second drying stage. Up until the appearance of the front shown in Figs. 6.6 and 6.9, the amount of water in the droplet is calculated as $1-\phi$, where ϕ is the volume fraction of silica. Water then continues to diffuse out of the droplet while the colloidal solid remains stationary.^{9,16} The latter leads to a constant calculated volume fraction of particles in the droplet, but indicates that the amount of water remaining in the droplet to solvate the salt continues to decrease. The salt concentration in the free solvent would then be higher than the concentration calculated from the silica volume fraction, and may contribute the formation of the second material that does not appear at lower salt concentrations ($[\text{Na}^+]_f < 310 \text{ mM}$).

In these experiments, there are a few operational limits that should be considered. The formation of the silica droplets in the droplet array requires

slightly lower flow rates to fill the device robustly compared with the formation of the droplets using water or salt solutions, but filling the device is otherwise straightforward at low concentrations of silica in mineral oil containing Span 80. Above 2% (v/v) of silica, the formation of droplets in mineral oil with surfactant is unsuccessful. The failure of the droplet formation process occurs in the step where the dispersed phase fills the trap (Fig. 5.2b). The dispersed phase slug is prevented from growing due to the high resistance introduced by the restriction for water or salt solutions, which keeps the slug in place until the tail end of the dispersed phase reaches the junction of the trap and bypass to pinch off a droplet. For silica suspensions with high concentrations $\phi_i > 0.02$, the resistance in the restriction is below the critical resistance needed, and the restriction acts similarly to a microfluidic nozzle for droplet generation. The dispersed phase slug enters the restriction and breaks into smaller droplets. These small droplets significantly influence the channel network of the subsequent trap and bypass units, and results in very few trapped droplets in the array.

Because droplet formation in the traps is a balance between viscous and capillary forces,³⁸ there are a few operational parameters that can be tuned to successfully form drops. Generally, a decrease in the flow rates of both the droplet and oil phases during droplet generation can mitigate most issues. However, at high silica concentrations, the capillary forces are too low such that even at low flow rates ($< 0.5 \mu\text{L}/\text{min}$), droplets are unable to form. This indicates that an increase the interfacial tension between the droplet and oil phase is necessary, and can be achieved by lowering the concentration of surfactant in the

mineral oil. However, for concentrations below 1 wt. % Span 80 in mineral oil, the droplet phase has been observed to wet the PDMS channels instead of the oil. Silicone oil can be substituted for mineral oil in the dehydration experiments involving more concentrated silica suspensions (Fig. 6.4), which resolves both wetting and droplet formation issues. It should be noted that mineral oil with surfactant is used for the majority of the droplet formation experiments because it yields more reproducible arrays with aqueous droplets.

The results plotted in Fig. 6.16 show that current microfluidic setup provides a basic test to determine the stability of a particle suspension. Extended droplet storage is possible over the course of several weeks, but the techniques probing suspension properties within this platform introduce a few limitations. As seen in Fig. 6.13, the change in mean square displacement over time indicates that the 3 μm tracer particles are able to sense local changes in the droplets up to $\text{MSD} < 3 \times 10^{-15} \text{ m}^2$. In theory, tracking the probe particles for a longer period of time decreases the minimum displacement that can be measured, but Eqs. (6.4) and (6.5) show that a decrease in probe particle size and an increase in magnification would be more effective for decreasing this limit for future studies.

There is also a lower limit on the suspension flocculation time that can be feasibly measured within the system. It is important to note that once the devices are submerged in water, the system takes about an hour to equilibrate and achieve a constant droplet volume. The equilibration time is relatively small compared with the flocculation time for the suspensions containing 430 mM NaCl (viscosity rise ~ 10 -11 hours), 270 mM (90 hours), and 170 mM (235 hours). In these cases,

the concentration is held constant for longer than it takes to dehydrate the drops. However, in the 630 mM NaCl case, the viscosity rise occurs 1-2 hours after the droplet has completely stopped shrinking, which is not a significant separation of timescales for dehydration and flocculation. The rheology data shows a G^* increase in about 1.5 hours for the bulk sample of the 630 mM NaCl system, so the behavior observed in the droplets with the same composition is consistent with the bulk sample. As a result, the lower limit of the flocculation times that can be probed in the microfluidic platform is about one hour for a particle suspension with added salt.

6.5. Conclusions

A microfluidic platform involving the trapping and storage of droplets containing colloidal suspensions is useful for probing suspension stability. In pure silica suspensions, the time required for a particle suspension to reach its final concentration increases with increasing humidity, but the final particle concentration is independent of dehydration rate. Unlike sessile drops drying in air, droplets of particle suspensions dehydrate homogeneously within the device. The final concentration of the silica suspensions is approximately $\phi \approx 0.6$, which corresponds to previously published values for either a glassy or ordered solid. Preliminary dehydration experiments with a model disk-shaped nanoparticle exhibited final particle concentrations significantly higher than previously reported for a clay suspension.

In addition to the dehydration studies of droplets of particle suspensions over tens of hours, time-dependent flocculation of particle suspensions with added salt is probed at constant composition using the trap-and-store microfluidic platform. The temporal variation of suspension viscosity as a function of the added salt concentration is monitored by tracking the motion of fluorescent particles within the droplets containing particle suspensions as a function of time. A dramatic increase in the suspension viscosity is observed with an increase in salt concentration, and agrees with results obtained from rheology measurements performed on bulk samples, as well as with previously published behavior for salted silica suspension.

It is worth noting that the droplet trap array used in the present experiments generates a 10x25 array of 8 nL droplets. The large sample size allows us to obtain statistically relevant and reproducible results regarding suspension behavior with a relatively small sample volume. Overall, the studies with silica and clay suspensions described here show proof of concept that the microfluidic platform described in Chapter 5 can be used to study the dehydration and stability of particle suspensions.

6.6. References

1. Cao, X. J.; Cummins, H. Z.; Morris, J. F. Structural and rheological evolution of silica nanoparticle gels. *Soft Matter*. **2010**, *6*, 5425-5433.
2. Sen, D.; Bahadur, J.; Mazumder, S.; Santoro, G.; Yu, S.; Roth, S. V. Probing evaporation induced assembly across a drying colloidal droplet using in situ small-angle X-ray scattering at the synchrotron source. *Soft Matter*. **2014**, *10*, 1621-1627.
3. Cousin, F.; Cabuil, V.; Levitz, P. Magnetic Colloidal Particles as Probes for the Determination of the Structure of Laponite Suspensions. *Langmuir*. **2002**, *18*, 1466-1473.
4. Di Giuseppe, E.; Davaille, A.; Mittelstaedt, E.; Francois, M. Rheological and mechanical properties of silica colloids: from Newtonian liquid to brittle behaviour. *Rheologica Acta*. **2012**, *51*, 451-465.
5. Haw, M. D.; Gillie, M.; Poon, W. C. K. Effects of Phase Behavior on the Drying of Colloidal Suspensions. *Langmuir*. **2002**, *18*, 1626-1633.
6. Peixinho, J.; Lefevre, G.; Coudert, F. X.; Hurisse, O. Water evaporation in silica colloidal deposits. *Journal of Colloid and Interface Science*. **2013**, *408*, 206-211.
7. Lebedev-Stepanov, P.; Vlasov, K. Simulation of self-assembly in an evaporating droplet of colloidal solution by dissipative particle dynamics. *Colloids and Surfaces A: Physicochemical and Engineering Aspects*. **2013**, *432*, 132-138.
8. Routh, A. F.; Russel, W. B. Horizontal drying fronts during solvent evaporation from latex films. *AIChE J*. **1998**, *44*, 2088-2098.
9. Dufresne, E. R.; Corwin, E. I.; Greenblatt, N. A.; Ashmore, J.; Wang, D. Y.; Dinsmore, A. D.; Cheng, J. X.; Xie, X. S.; Hutchinson, J. W.; Weitz, D. A. Flow and Fracture in Drying Nanoparticle Suspensions. *Physical Review Letters*. **2003**, *91*, 224501.
10. Allain, C.; Limat, L. Regular Patterns of Cracks Formed by Directional Drying of a Colloidal Suspension. *Physical Review Letters*. **1995**, *74*, 2981-2984.
11. Merlin, A.; Salmon, J. B.; Leng, J. Microfluidic-assisted growth of colloidal crystals. *Soft Matter*. **2012**, *8*, 3526-3537.
12. Wallenstein, K. J.; Russel, W. B. The theory of delamination during drying of confined colloidal suspensions. *Journal of Physics: Condensed Matter*. **2011**, *23*, 194104.
13. Inasawa, S.; Yamaguchi, Y. Self-organized pattern formation of cracks perpendicular to the drying direction of a colloidal suspension. *Soft Matter*. **2012**, *8*, 2416-2422.
14. Krieger, I. M.; Dougherty, T. J. A Mechanism for Non-Newtonian Flow in Suspensions of Rigid Spheres. *Transactions of the Society of Rheology*. **1959**, *3*, 137-152.

15. Baranau, V.; Tallarek, U. Random-close packing limits for monodisperse and polydisperse hard spheres. *Soft Matter*. **2014**, *10*, 3826-3841.
16. Lidon, P.; Salmon, J.-B. Dynamics of unidirectional drying of colloidal dispersions. *Soft Matter*. **2014**,
17. Russel, W. B.; Saville, D. A.; Schowalter, W. R. *Colloidal Dispersions*, Cambridge University Press, 1989,
18. Trappe, V.; Sandkuhler, P. Colloidal gels - low-density disordered solid-like states. *Current Opinion in Colloid & Interface Science*. **2004**, *8*, 494-500.
19. Prieve, D. C.; Ruckenstein, E. Role of surface chemistry in primary and secondary coagulation and heterocoagulation. *Journal of Colloid and Interface Science*. **1980**, *73*, 539-555.
20. So, J. H.; Yang, S. M.; Kim, C.; Hyun, J. C. Microstructure and rheological behaviour of electrosterically stabilized silica particle suspensions. *Colloids and Surfaces A: Physicochemical and Engineering Aspects*. **2001**, *190*, 89-98.
21. Schindler, M.; Ajdari, A. Modeling phase behavior for quantifying micro-pervaporation experiments. *The European Physical Journal E*. **2009**, *28*, 27-45.
22. Shirk, K.; Steiner, C.; Kim, J. W.; Marquez, M.; Martinez, C. J. Assembly of Colloidal Silica Crystals Inside Double Emulsion Drops. *Langmuir*. **2013**, *29*, 11849-11857.
23. Mason, T. G.; Ganesan, K.; van Zanten, J. H.; Wirtz, D.; Kuo, S. C. Particle Tracking Microrheology of Complex Fluids. *Physical Review Letters* **1997**, *79*, 3282-3285.
24. Schultz, K. M.; Furst, E. M. High-throughput rheology in a microfluidic device. *Lab on a Chip*. **2011**, *11*, 3802-3809.
25. Breedveld, V.; Pine, D. J. Microrheology as a tool for high-throughput screening. *Journal of Materials Science*. **2003**, *38*, 4461-4470.
26. Wereley, S. T.; Meinhart, C. D. Recent Advances in Micro-Particle Image Velocimetry. *Annual Review of Fluid Mechanics*. **2010**, *42*, 557-576.
27. Williams, S.; Park, C.; Wereley, S. Advances and applications on microfluidic velocimetry techniques. *Microfluidics and Nanofluidics*. **2010**, *8*, 709-726.
28. Zantow, M.; Dendere, R.; Douglas, T. S. Image-based analysis of droplets in microfluidics. *Engineering in Medicine and Biology Society (EMBC), 2013 35th Annual International Conference of the IEEE*. **2013**, 1776-1779.
29. Squires, T. M.; Mason, T. G. Fluid Mechanics of Microrheology. *Annual Review of Fluid Mechanics*. **2010**, *42*, 413-438.
30. Crocker, J. C.; Grier, D. G. Methods of Digital Video Microscopy for Colloidal Studies. *Journal of Colloid and Interface Science*. **1996**, *179*, 298-310.
31. Sbalzarini, I. F.; Koumoutsakos, P. Feature point tracking and trajectory analysis for video imaging in cell biology. *Journal of Structural Biology*. **2005**, *151*, 182-195.

32. Michalet, X. Mean square displacement analysis of single-particle trajectories with localization error: Brownian motion in an isotropic medium. *Phys. Rev. E* **2010**, *82*, 041914.
33. Wirtz, D. Particle-Tracking Microrheology of Living Cells: Principles and Applications. *Annual Review of Biophysics*. **2009**, *38*, 301-326.
34. Cheng, N. S. Formula for the Viscosity of a Glycerol-Water Mixture. *Industrial & Engineering Chemistry Research*. **2008**, *47*, 3285-3288.
35. Cummins, H. Z. Liquid, glass, gel: The phases of colloidal Laponite. *Journal of Non-Crystalline Solids*. **2007**, *353*, 3891-3905.
36. Ruzicka, B.; Zaccarelli, E. A fresh look at the Laponite phase diagram. *Soft Matter*. **2011**, *7*, 1268-1286.
37. Ruzicka, B.; Zulian, L.; Ruocco, G. More on the Phase Diagram of Laponite. *Langmuir*. **2005**, *22*, 1106-1111.
38. Boukellal, H.; Selimovic, S.; Jia, Y.; Cristobal, G.; Fraden, S. Simple, robust storage of drops and fluids in a microfluidic device. *Lab on a Chip*. **2009**, *9*, 331-338.

Chapter 7. Nucleation and Crystal Growth Studies in a Microfluidic Platform

7.1.Introduction

Crystallization is a phase transition that occurs when a solution exceeds the saturation concentration of the solute, and the solute nucleates and grows into a crystal. The nucleation and growth process depends on temperature, degree of supersaturation, initial concentration, the solute and solvent pair, and other additives or impurities. Furthermore, these conditions dictate not only whether a crystal will form, but also what the crystal structure will be. Crystal structure is important to applicability and stability, which then has implications for the effectiveness of a material for a specific application. This is particularly true in pharmaceuticals, where two crystal forms of the same molecule may have vastly different properties and applications. Common techniques for inducing crystallization include dehydration, solvent exchange, freeze-drying, and temperature control.¹⁻⁴

Crystals are formed when molecules orient and form a unit cell that repeats, giving rise to long-range order. The type of unit cell falls into one of seven crystal systems: monoclinic, triclinic, orthorhombic, tetragonal, trigonal, hexagonal, and cubic. Molecules can exist in more than one crystal form, or polymorph, which leads to distinct differences in properties.⁵ Characterization techniques that distinguish between different polymorphs include differential scanning calorimetry (DSC), Fourier-transform infrared spectroscopy (FTIR),

Raman spectroscopy, and x-ray diffraction (XRD).¹ However, the polymorph does not fully determine the appearance of the crystal, and so crystals are also characterized by the habit, which describes the shape of the crystal in terms of its major axes, and its morphology, which describes the general appearance of the crystal. Differences in the rate of growth of the faces in a crystal habit lead to changes in the morphology.^{5,6}

Screening crystallization conditions for those that result in a polymorph with desired properties is a time- and cost-intensive process. Platforms are commercially available to facilitate this process and are typically comprised of multi-well plates that require microliters of crystallizing solution and milliliters of precipitant solution. Other systems generate drops of crystallizing solution and allow them to dehydrate in an air environment. Due to the water concentration gradient between the drop and reservoir or ambient environment, the solvent diffuses out of the drop and concentrates the contents within, which eventually leads to crystallization.⁷⁻⁹ In addition to large number of variables that may affect crystal formation, these crystallization studies are particularly sensitive to the presence of impurities and mechanical shocks. Both are difficult to completely eliminate and may induce heterogeneous nucleation, which may also influence the final crystal polymorph.

Microfluidic crystallization methods also exist and can utilize the formation of droplets of order of hundreds of microns in diameter, which range from picoliters to nanoliters in volume.¹⁰ Each droplet can be considered to be an individual microreactor, and the droplets may be trapped and stored in a

microfluidic device for ongoing observation. Microfluidic techniques have the advantage of performing a large number of crystallization experiments with a sample size that is orders of magnitude smaller than the milliliter-size multi-well platform described above. Due to the small volume of each individual droplet, the presence of impurity is low, and crystallization is more likely to be homogeneous when using a microfluidic system.¹¹⁻¹⁶

Crystallization experiments carried out in microfluidic droplet platforms typically use a microfluidic nozzle and/or one of the trapping techniques described in Chapter 5 to form and store drops for long-term observation.¹⁷⁻²¹ Microfluidic platforms can both rapidly screen crystal polymorph and be used to make quantitative measurements on the nucleation and growth of crystals. Nucleation rates are typically difficult to measure with statistical confidence due to the amount of sample required per experiment and the isolation required to ensure controlled crystallization. The probability $P(t)$ that a drop does not contain a crystal at time t is given by

$$P(t) = 1 - \exp(-Jt) \quad (7.1)$$

where J is the nucleation rate or number of nuclei produced per unit time and volume, and V is the droplet volume. In classic nucleation theory, the energy barrier to nucleation is defined assuming that the crystal nucleus is separated from the supersaturated bulk solution by an interface, and J is given by

$$J = AC \exp \left[-\frac{B}{[\ln(S+1)]^2} \right], \quad (7.2)$$

where A is a kinetic factor defined as

$$A = \frac{2\nu(kT\gamma)^{1/2}}{\hbar}, \quad (7.3)$$

C is the solute concentration, S is the supersaturation, and B is given by

$$B = \frac{-16\pi\gamma^3\nu^2\Delta G_a}{(kT)^4} \quad (7.4)$$

for a spherical nucleus. In Eqs. 7.3 and 7.4, ν is the molecular volume of the crystal, k is the Boltzmann constant, T is the temperature, γ is the interfacial tension between the nucleus and the solution, \hbar is Planck's constant, and ΔG_a is the activation energy.^{17,18} Other models used to fit experimental data have included nonhomogeneous Poisson process models and two-exponential models that take in to account both heterogeneous nucleation at early times and homogeneous nucleation at long times.^{19,22} In most platforms controlling crystallization, the probability of crystallization is difficult to measure in detail, but the nucleation time, or endpoint of the nucleation and growth process, is measured and nucleation statistical models such as the classic nucleation theory given by Eq. (7.2) are inferred from the measured characteristic timescales.

Crystal growth measurements provide insights into the mechanisms that govern variations in crystal polymorph as a result of variations in formulation or environment. Once a stable crystal nucleus has formed, additional molecules must diffuse to the nucleus and orient themselves properly on the nucleus interface in order for the crystal to grow. Either of these steps can limit the rate of crystal growth. In the case of interface-limited growth, the growth of a single face or in a single direction r has the relationship $r \sim t$; for diffusion-limited growth, the relationship is $r \sim t^{1/2}$. Crystal growth measurements are straightforward, and are

easily performed in microfluidic experiments where a microscope is available to image the droplets. Existing crystallization studies in microfluidic devices indicate that microfluidic techniques are uniquely suited to probe crystallization from solution and can generate substantial sample sizes for examining statistics.⁴ We use the droplet trap-and-store platform characterized in Chapter 5 to show that droplet dehydration can be used to study the mechanisms governing crystallization of a system.

The crystallization studies presented here use the amino acid glycine, which has been extensively studied in the literature due to its frequent application as an additive in food and pharmaceutical applications, as well as for its simplicity for computational studies. Glycine has several polymorphs that are present at standard temperature and pressure. At room temperature, glycine typically crystallizes into one of two stable polymorphs, α or γ . The first is the kinetically favored polymorph, while γ -glycine is more thermodynamically stable. In the presence of an alcohol or during freeze-drying, the unstable β polymorph can be formed.²³⁻²⁶ Each of these polymorphs tends to have a distinctive shape: α -glycine typically looks like a prism with pyramidal endcaps, β -glycine is needle-like, and γ -glycine appears as a spheroid with no defining features.

The effect of salt, pH, alcohols and solvents, surfactants, temperature, dehydration rate, and continuous phase oil are a few of the many parameters that have been tuned in order to control the polymorph of glycine.²⁶⁻²⁹ For example, it is now known that the formation of γ -glycine over the α polymorph is encouraged in the presence of sodium chloride; for pH values below 3 or above 10; with the

addition of anionic surfactants; and with slow dehydration rates. The postulated reason for this polymorph preference is a self-poisoning mechanism, where the formation of α -glycine, the polymorph that grows the fastest, is inhibited or suppressed by an additive such that the γ -polymorph can grow instead.²⁷⁻³⁰ Han *et al.* have shown that this is not completely supported for pH adjustments by growing crystals of a single polymorph in acidic and basic environments and measuring the linear growth rate of each face. They find that the growth rate of both α - and γ -glycine are increased below a pH of 3 or above a pH 10, showing that the assumed decrease in growth rate of the α polymorph is incorrect, and proposed that the rate of nucleation of a given polymorph is also important in polymorph control.^{28,29} These studies demonstrate the importance of both polymorphic characterization and measurements of crystal nucleation and growth rates in crystallization studies.

Glycine has been observed to crystallize spherically when formed using microfluidic crystallization techniques. These spherulite crystals grow radially from the nucleus and usually have a polycrystalline structure that consists of tiny needles or lamellae that give the overall appearance of a spherical crystal. Spherical crystallization is typically carried out in a surfactant-stabilized emulsion and can occur in either the interface-limited or diffusion-limited growth regime.^{31,32} Spherulites are advantageous in pharmaceutical applications since they are easier to process downstream due to their uniform shape, flow properties, and compressibility.³³ A comprehensive overview of the formation of spherulites can be found elsewhere.³² Previous groups that have studied the spherical

crystallization of glycine liken the process to that of a crystallizing melt and find that crystal growth occurs at a constant rate. Once the glycine crystals are formed, they can “age” and rearrange into a cluster composed of smaller crystals. The final product typically contains mostly α -glycine, with trace amounts of β - and γ -glycine.^{22,34}

This chapter addresses the use of a microfluidic droplet-based technique to study the crystallization of glycine. Experiments are carried out to compare the dehydration of glycine drops to the dehydration in the systems studied in previous chapters. Nucleation statistics and growth of spherical glycine crystals are also monitored as a function of glycine concentration and additive. The crystals are harvested and characterized off-chip.

7.2. Materials and Methods

We crystallize glycine using the microfluidic platform described in Chapter 5 and systematically vary the conditions to be consistent with previous studies. The parameters that we consider include dehydration rate, initial concentration, and the presence of salt (NaCl) and colloidal particles (Ludox TM) as additives. For each experiment, we record droplet volume as a function of time; nucleation statistics for a large array of droplets containing a uniform composition of glycine solution; crystal growth rate in individual droplets; the visual appearance of the resulting crystal and any subsequent aging; and polymorph characterization through Raman spectroscopy and x-ray diffraction (XRD).

Sodium chloride (>99%, Fisher Scientific), glycine (>99%, Sigma-Aldrich), and Ludox TM-40 (Sigma-Aldrich) are obtained and used as received. A 2.0 M stock solution of NaCl, and 0.5, 1.0, and 2.0 M glycine solutions are prepared using deionized water (resistivity = 18.2 M Ω -cm, Thermo Scientific Barnstead EasyPure II). All solutions are filtered using a 0.2 μ m filter (Pall Acrodisc CR PTFE Syringe Filter) prior to use. The continuous phase liquid in the microfluidic experiments is light mineral oil (“MO”, Fisher Scientific) containing 3 or 5 wt. % Span 80 surfactant.

Droplets containing the crystallizing solution are formed using the same protocol described in Section 5.2 for generating droplet arrays in a polydimethylsiloxane (PDMS) microfluidic device. The humidity control chamber described in Section 5.2 is used for the experiments that involve the full dehydration of glycine solutions at relative humidities of 5, 25, 50, and 75% at 20°C. Droplet volume measurements are conducted following the protocol described in the previous chapters for dehydrating droplets.

To image larger sections of the array for nucleation statistics, an optical table (Richards Corporation Image Interpretation Systems HFO-4 with a Bausch and Lomb microscope) fitted with a CCD camera (Panasonic WV-CD22) records an image every 2 minutes until all droplets in the viewing window have crystallized; the total time for this experiment depends on the relative humidity. The section of droplets imaged is chosen to avoid the top and bottom rows and the first and last columns of traps, as slight differences in dehydration rates have been

observed on the edges of the array. The number of crystallization events in the array as a function of time is counted manually.

Crystal growth is monitored using a microscope (Nikon Ti-U) fitted with a 20X objective and a high speed camera (Vision Research Phantom v9.1). Videos are recorded at frames rates from 30 fps to 1000 fps, and adjusted to ensure sufficient temporal resolution such that the crystal increases in size by an area that is greater than the spatial resolution of the image without masking the growth rate behavior. Images are analyzed using ImageJ software (National Institutes of Health) to measure the crystal size based on the projected area in square pixels. Assuming spherical growth, an effective crystal radius is determined from the measured area. The effective radius is converted to microns using a conversion factor of 0.56 pixels/ μm , which was previously determined using the protocol described in Chapter 3.

Once the entire array has crystallized, the crystals are harvested by reversing the flow of the outer phase oil in the array of traps. The crystals are carried out along with the oil and can be collected in a centrifuge tube. The crystals typically sediment to the bottom of the tube without additional processing, but they can also be centrifuged (VWR Galaxy Mini Microcentrifuge) to facilitate sedimentation. The collection of the crystals simplifies the sample preparation required for spectroscopic characterization.

A small drop of oil containing the crystals is pipetted onto a microscope slide or glass sample holder. Excess oil is carefully removed, leaving a thin layer of oil covering the crystals. The Raman spectra of ten crystals are obtained using

a Raman microscope (Horiba LabRAM HR); each crystal is scanned twice in two locations. XRD scans of a sample of ~50-100 crystals are acquired using a Panalytical X'Pert Pro MPD X-Ray Diffractometer. Tables 7.1 and 7.2 show the expected peaks for each glycine polymorph obtained from Raman spectroscopy and x-ray diffraction, respectively.

α -glycine (cm ⁻¹)	γ -glycine (cm ⁻¹)
	41
52	
74	
	91
110	
	154
163	
180	
198	
356	358
491	

Table 7.1. Expected wavenumbers (cm⁻¹) of glycine peaks from Raman spectroscopy. Many peaks above 500 cm⁻¹ are similar for both polymorphs and cannot be used to definitively distinguish between the two polymorphs.^{35,36}

α -glycine	γ -glycine
14.8°	14.6°
19.0°	21.8°
20.1°	<i>25.4°</i>
23.9°	29.4°
28.5°	<i>35.9°</i>
29.2°	39.1°
<i>29.9°</i>	44.6°
31.0°	<i>56.4°</i>
36.6°	

Table 7.2. Expected values of 2 θ (°) for glycine from x-ray diffraction. The major peaks (those with relative intensities above 70%) are bolded and italicized. There are a significant number of minor peaks in both of these spectra, but only a few are listed that are used to identify the polymorph from XRD spectra.^{6,37}

7.3.Results

Fig. 7.1 shows the progression over 12 hours of a droplet initially containing 1.0 M glycine surrounded by mineral oil and stored in a microfluidic

device in ambient conditions at 5% relative humidity. Droplet formation follows the same protocol described in Chapter 5 without any modifications. Fig. 7.1a shows the droplet immediately after formation, which has deformed to fit into the confines of the trap and has attained a slug shape. Figs. 7.1b-e show the expected droplet shape transitions as the droplet dehydrates. In Fig. 7.1f, the droplet achieves the glycine concentration at which the refractive index of the droplet equals that of the mineral oil phase and the edge of the droplet is no longer visible in the image. The droplet crystallizes within a couple of hours after this observation, and the final crystal is shown in Fig. 7.1g with a spherulite morphology.

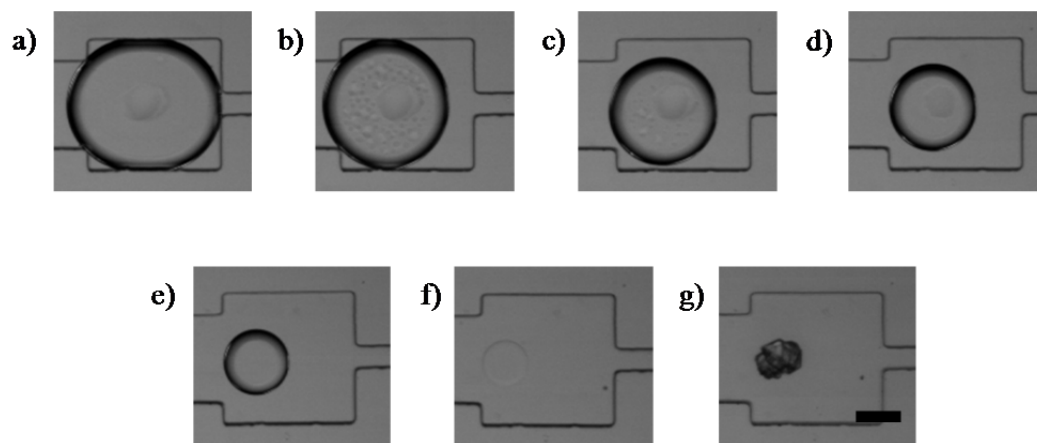


Figure 7.1. Dehydration of a trapped droplet containing a glycine solution ($C_i = 1.0$ M) in mineral oil over 12 hours at 5% relative humidity. Two hours have elapsed between each image from left to right. Scale bar is 100 μm .

We use the equations for droplet volumes presented in Chapter 5 to calculate the solute concentration within the droplets as a function of time. Using Eq. (5.2) for the volume of a slug-shaped droplet, the initial volume is approximately 8 nL, which is the same as the initial volume obtained for the

systems studied in Chapters 5 and 6. The droplet and mineral oil refractive indices are equal ($n = 1.46$) approximately 10 hours after initial droplet formation (Fig. 7.1f), which corresponds to a glycine concentration in the droplet of 10.5 M for this image sequence. Immediately before crystal formation, the glycine concentration of the droplet is 12.6 M in this image sequence. The saturation concentration of glycine at 20°C is 2.6 M, so the supersaturation ratio just prior to glycine crystallization in this case is 4.8.

Table 7.3 summarizes the solute compositions used in addition to relative humidity control to demonstrate that a dehydration-based microfluidic platform can be used to study crystallization. The initial concentrations and the final concentrations of the components immediately prior to crystallization are given. The corresponding supersaturations of glycine are also reported and show that in all cases, the glycine concentration is four to five times the saturation concentration immediately prior to crystallization.

$[\text{Glycine}]_i$ (M)	$[\text{Glycine}]_f$ (M)	$[\text{Gly}]_f$ / $[\text{Gly}]_s$	$[\text{NaCl}]_i$ (M)	$[\text{NaCl}]_f$ (M)	$\phi_{i, \text{silica}}$	$\phi_{f, \text{silica}}$
0.5	12.0 ± 0.2	4.6				
1.0	12.6 ± 0.2	4.8				
2.0	12.4 ± 0.2	4.8				
1.0	12.4 ± 0.3	4.8	0.10	1.2 ± 0.06		
1.0	12.1 ± 0.1	4.7	0.40	4.9 ± 0.02		
1.0	11.4 ± 0.3	4.4			1.1×10^{-9}	$(1.2 \pm 0.03) \times 10^{-8}$
1.0	10.4 ± 0.3	4.0			0.0021	0.024 ± 0.001

Table 7.3. Initial and final concentrations prior to crystallization of glycine and additives for systems studied at 5-10% relative humidity. The glycine supersaturation $[\text{Gly}]_f / [\text{Gly}]_s$ is also listed, where the saturation concentration of glycine at 20°C $[\text{Gly}]_s = 2.6$ M.

Fig. 7.2 plots the experimental time required to fully dehydrate a glycine droplet as a function of relative humidity. The experimental end time for glycine droplets is defined as the time at which 75% of the droplets imaged have achieved

their final state; i.e., a crystal has appeared or the droplet volume has reached a constant value). The measured end times for droplets that have an initial glycine concentration of 1.0 M are shown in Fig. 7.2 (◆), along with the experimental end times for droplets containing pure water (●), 1 mM NaCl (■), and 100 mM NaCl (▲), which are included from Fig. 5.12 for comparison.

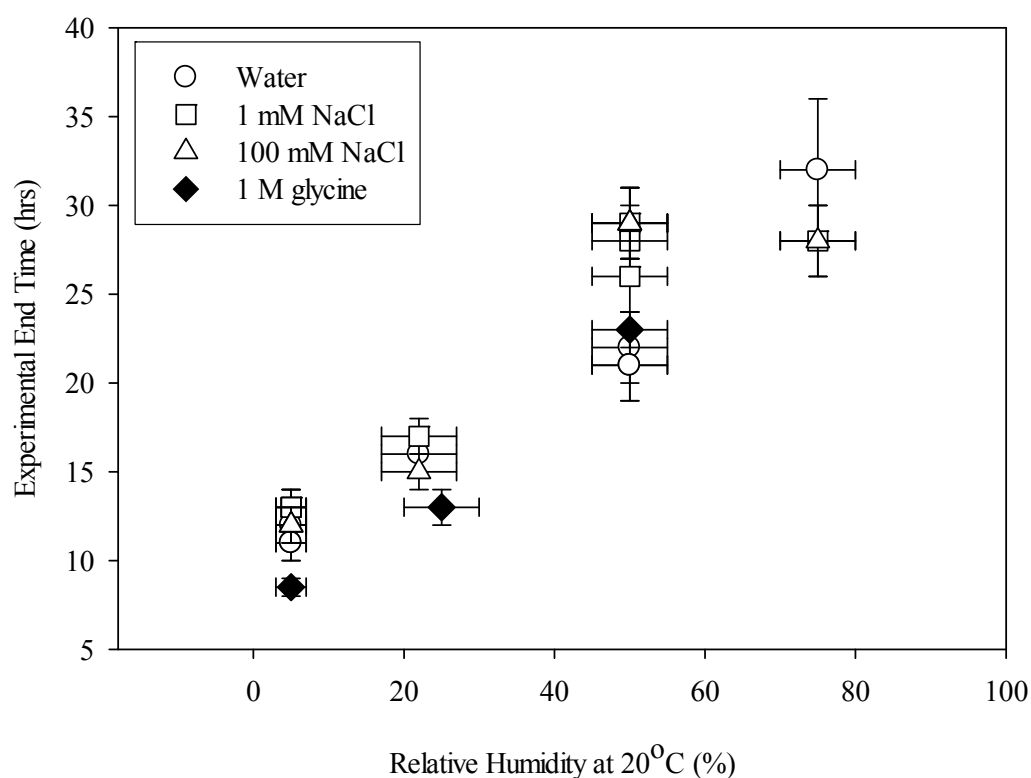


Figure 7.2. Time for 75% of the droplets sampled within an array to reach the final state (water (○) – complete dehydration of droplet, NaCl (□ and △) and glycine (◆) – crystallization or constant droplet volume). All concentrations given refer to the initial concentration of the solute within the droplet.

The data points plotted in Fig. 7.2 lie along the same trajectory, and show that as the relative humidity of the ambient environment increases, the experimental end time increases. Dehydration of droplets of glycine solutions follows the same behavior observed for pure water and salt droplets, and the

glycine readily crystallizes at low humidities ($< 50\%$). There is no data point corresponding to glycine solutions dehydrated at 75% relative humidity since the glycine droplets begin to severely wet the PDMS channel walls after 48 hours in this case. Wetting distorts the shape of the droplet, so the droplet volume cannot be estimated using the droplet shape estimates described earlier. In addition, the PDMS surface may act as a nucleation site, and which influences the measured experimental end time.

Fig. 7.3 plots the fraction of droplets, or probability P , that have *not* crystallized within the sampled section of the droplet array as a function time t . The probability P is equal to unity prior to the first crystallization event. All droplets that fill the traps during the formation of the array are considered; empty traps or partially filled traps with small drops are ignored. The time between stable nucleus formation and growth of a crystal to a visible size is neglected for the present studies, an assumption that is also made in previous studies.³⁸ The initial time t_o for Fig. 7.3 is defined as the time t_{sat} at which the droplets have reached the saturation concentration for glycine $C_s = 2.6$ M after dehydrating. The saturation time is determined from the analysis of the dehydration of individual droplets and occurs at $t_{sat} = 5.25 \pm 0.25$ hours from the formation of the array of droplets at a relative humidity of 10% for a droplet initially containing 1.0 M glycine. For 0.5 M glycine, the time to saturation is $t_{sat} = 7.75 \pm 0.25$ hours; for 2.0 M glycine, $t_{sat} = 2.00 \pm 0.25$ hours. Experiments corresponding to three initial glycine concentrations of 0.5 M (●), 1.0 M (■), and 2.0 M (▲) are plotted in

Fig. 7.3. As time increases, the probability that a droplet has not crystallized decreases. The relative humidity is held constant at 10% for all three experiments.

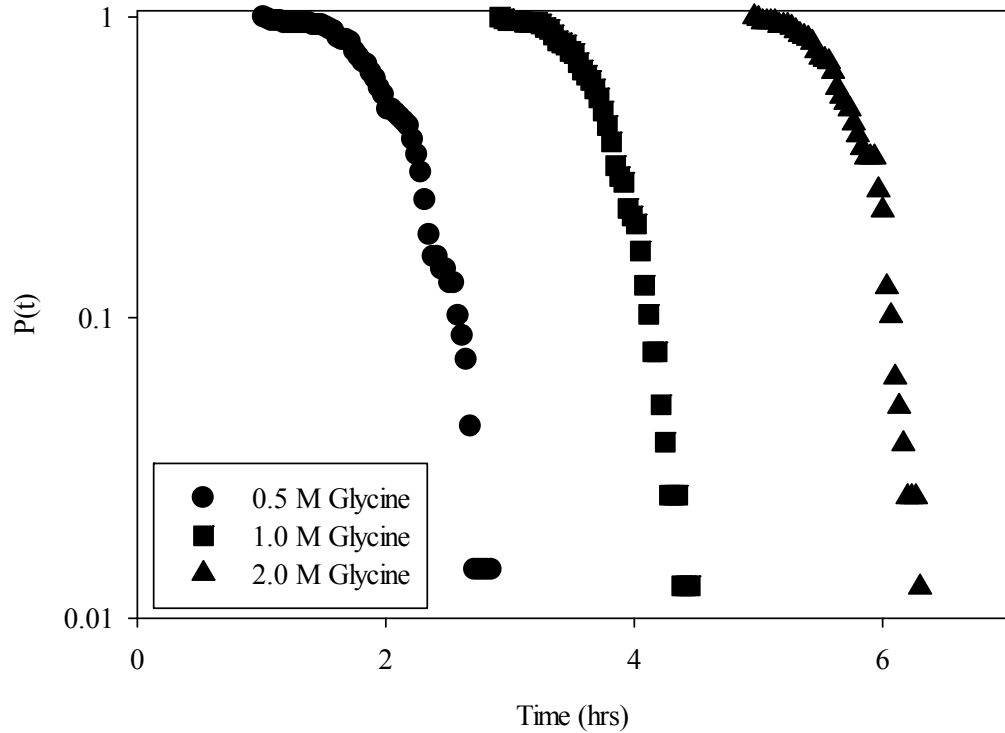


Figure 7.3. The probability that a droplet has not nucleated and crystallized at a given time for a glycine solution at the following initial concentrations: 0.5 M (●), 1.0 M (■), 2.0 M (▲). Experiment is carried out at 10% relative humidity.

The data shown in Fig. 7.3 are adjusted such that the initial time corresponds to the saturation time of the droplets, thus only includes the times at which all the droplets are above the saturation concentration of glycine. Fig. 7.3 shows that an increase in initial glycine concentration leads to an increase in the time required to achieve a fully crystallized array of droplets. As discussed later, the time for a droplet to become fully crystallized is significantly shorter than the time between droplets crystallizing within an array. The error associated with the time for each data point therefore depends on the image sampling rate, which is

equal to one image acquired every two minutes. The average nucleation time for each initial concentration is given in Table 7.4 along with the standard deviation and number of droplets that are sampled. Overall, the total experimental time from array formation to full crystallization is 9-11 hours for pure glycine droplets.

	Average Time to Crystallization for a Single Droplet (hours)	Sample Size
Pure – 0.5 M	2.06 ± 0.40	69
Pure – 1.0 M	3.74 ± 0.32	78
Pure – 2.0 M	5.73 ± 0.31	79
1.0 M + 100 mM NaCl	4.34 ± 0.41	79
1.0 M+ 400 mM NaCl	8.01 ± 5.20	80
1.0 M + 0.2% (v/v) Ludox TM	4.14 ± 0.27	79

Table 7.4. Average time and standard deviation to crystallization once a glycine droplet has reached saturation concentration; time required for the entire droplet array to crystallize at 10% relative humidity; and number of drops sampled in each array.

Nucleation measurements are also performed with the addition of salt or colloidal silica particles. Fig. 7.4 shows the probability P that crystallization has not occurred as a function time t for a 1.0 M glycine solution with two concentrations of added salt, 100 mM (∇) and 400 mM (\diamond), and 0.2% (v/v) silica nanoparticles (open hexagon). The data shown in Fig. 7.3 for a 1.0 M glycine solution (\blacksquare) is also included in Fig. 7.4 for comparison. All experiments are carried out at 10% relative humidity and the presence of additives at 10% relative humidity does not significantly alter the time at which the droplets achieve the saturation concentration of glycine. The start time t_o used in the nucleation measurements plotted in Fig. 7.4 is 5.25 hours after the formation of the droplet arrays. The probability P that a droplet has not crystallized decreases as time elapses. As seen in Fig. 7.4b, the probability dramatically decreases over time

until all the drops in the array have crystallized for the droplets containing pure glycine; glycine with 100 mM NaCl; and glycine with 0.2% silica particles. For the array of droplets initially containing glycine with 400 mM NaCl, the probability of observing no crystal quickly decreases at early times. At later times, a significant fraction of uncrystallized droplets are observed to remain at a constant volume without crystallization for an extended period of time. These stable droplets eventually crystallize, as indicated by the slow decreases in the probability curve at long times until all droplets have crystallized. The slow crystallization period includes a significant number of droplets in the array. For this sample of 80 droplets, at 10 hours there are 14 uncrystallized droplets that slowly crystallize over the next 35 hours. The crystallization of individual droplets can be seen in the discretization of the probability curve into step-like changes during this late time period.

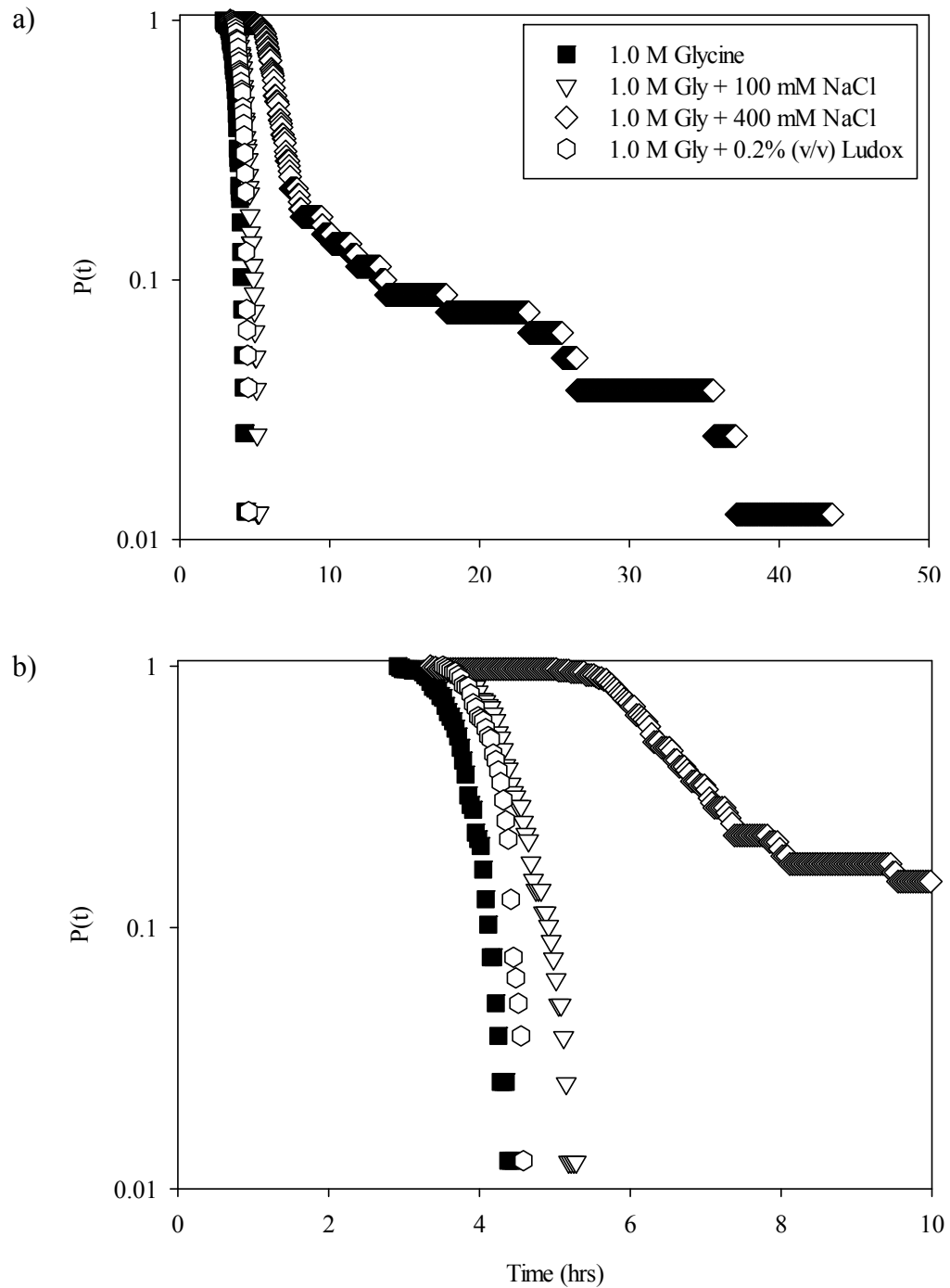


Figure 7.4. The probability that a droplet has not crystallized at a given time for a pure 1.0 M glycine solution (\blacksquare) and a 1.0 M glycine solution with added salt ($[\text{NaCl}]_i = 100\text{mM}$ (∇) and 400 mM (\diamond) or with 0.2% (v/v) silica nanoparticles (open hexagons). Experiments are carried out at 10% relative humidity. a) Full nucleation probability curves for all droplet compositions, with an expanded view of the first 10 hours shown in b).

The addition of 100 mM salt to the initial glycine solution increases the average time to crystallization from 3.74 to 4.34 hours (Table 7.4). The addition of 400 mM NaCl has a more dramatic effect on the nucleation rate of glycine crystals and increases the average time to nucleation to over 8 hours, due to the slow crystallization period described above. There is also a slight increase in the average time to crystallization with the addition of silica nanoparticles.

The rate at which a crystal grows subsequent to nucleation also depends on the mechanisms governing crystallization. Fig. 7.5 shows the growth of a spherical crystal formed within a droplet of glycine solution stored within a microfluidic trap. In Fig. 7.5a, the concentration of the glycine solution within the droplet is $C > 12$ M. The start time t_o is defined as the frame recorded immediately before the formation of the crystal is detected. For droplets containing pure glycine, glycine with 100 mM NaCl, and glycine with silica, this time step is 2 milliseconds prior to nucleation; for glycine with 400 mM NaCl, this time step is 1 second prior to nucleation due to the slower frame rate used to record growth. At time $t = 0.01$ seconds, a small dark mass is observed in the lower left area of the droplet in Fig. 7.5b, indicating that nucleation has occurred and the crystal has grown to a visible size. Nucleation is not observed to consistently occur at a specific site on the droplet and appears to occur either at the interface or in the middle of the droplet. Fig. 7.5c shows that the crystal interface grows radially and rapidly advances from the nucleus. Within about a tenth of a second, crystal growth is stopped by the droplet boundary, and the entire droplet has crystallized (Fig. 7.5d). Soon after the droplet crystallizes, the

crystal mass shifts in appearance and ages as shown in Fig. 7.5e, forming an agglomerate comprised of many smaller crystals within about 30 seconds. Any remaining water continues to dehydrate until only the solid phase remains.

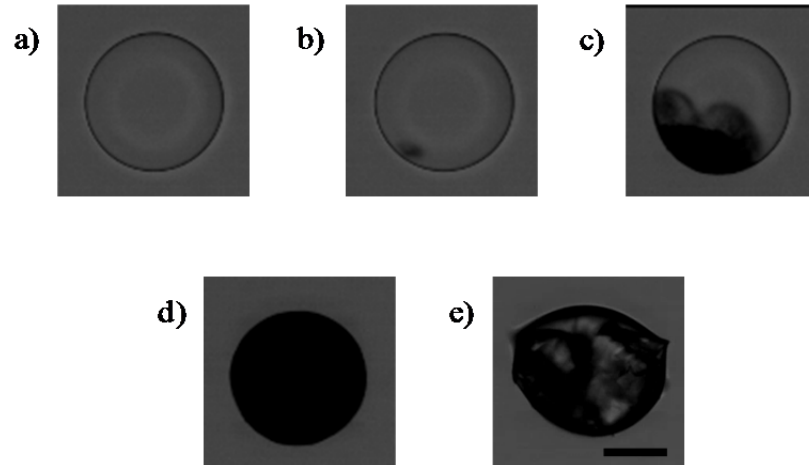


Figure 7.5. Spherical crystallization of glycine ($C_i = 1.0$ M) in a dehydrating microfluidic droplet at 10% relative humidity at 20°C. Time t on each image is equal to a) 0, b) 0.01, c) 0.06, and d) 0.11 seconds. Within a few seconds, e) the crystallized droplet begins to “age.” The scale bar is 50 μm .

Fig. 7.6 is a plot of the effective crystal radius as a function of time for the growth of a crystal formed within a droplet of supersaturated glycine solution. The effective crystal radius $R_{\text{eff},\text{crystal}}$ is scaled by the radius of the droplet R_{droplet} prior to the onset of crystallization, and the time t is scaled by the total time required for the entire drop to crystallize t_{final} . This normalization of the coordinates ensures that all experiments lie below unity on both axes. Five experiments are shown, corresponding to droplets initially containing 1.0 M glycine (■); 1.0 M glycine with 100 mM NaCl (◇); 1.0 M glycine with 400 mM NaCl (▽); 1.0 M glycine with 0.0002% (v/v) (dilute) silica (open star); and 1.0 M glycine with 0.2% silica (open hexagon). All five experiments are carried out at 10% relative humidity. Using the same start time t_o described above, a crystal has

not yet formed, so the effective crystal radius r is equal to zero. It should be noted that the image resolution of crystal growth at early times is not high enough to properly measure the crystal size, so there are no values reported for crystal growth for very early times. At intermediate times at which the crystal can be robustly measured, the effective crystal radius increases and levels off once the crystal size reaches the droplet interface.

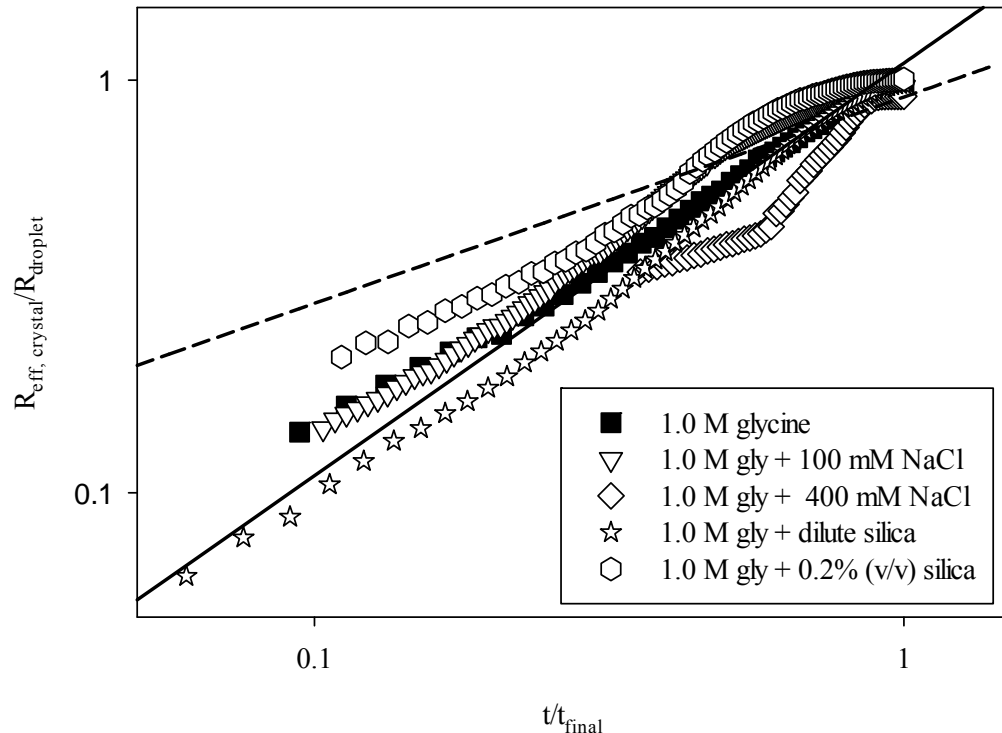


Figure 7.6. Growth of the effective radius of the glycine crystal for 1.0 M glycine (■); 1.0 M glycine with added salt (100 mM NaCl (∇) and 400 mM (◇)); and glycine with added silica (dilute (open star) and 0.2% (v/v) (open hexagon)). Measurements are carried out only when a clear image of the growing crystal is observed and can be reasonably measured. Experiments are carried out at 10% relative humidity at 20°C.

Each of the data sets shown in Fig. 7.6 appears to exhibit at least two different slopes during crystal growth. For most cases, the initial crystal growth is roughly linear with time, as shown by comparison with the solid line depicting

$r \sim t$. At later times, the growth rate slows down for all cases as the size of the crystal approaches the size of the encompassing droplet. The slope of the growth at late times approaches $r \sim t^{1/2}$ for a short time prior to the completion of crystallization, indicating the likely approach to diffusion limited growth as the thinning liquid shell surrounding the growing crystal becomes depleted of solute. In the case of crystal growth for a droplet containing glycine with 400 mM NaCl, the effective radius increases as $r \sim t^{1/2}$ at early times, indicating the possibility of diffusion limited growth. At later times, there is a distinct change in crystal growth behavior during which the slope is greater than unity, followed by the same late-time slowing observed in the other four cases.

The scaling of the axes collapses the crystal growth curves such that droplets of varying size and growth rates can be compared for mechanistic changes in growth behavior. The parameters used in the scaling (the droplet radius $R_{droplet}$ and total crystal growth time t_{final}) for each case shown in Fig. 7.6 are summarized in Table 7.5. The rate of growth varies between experiments and a few trends are observed. For the pure glycine case, the time for a droplet to progress from Fig. 7.5a to 7.5d is $t_{final} = 0.11$ seconds. The addition of salt increases the total time t_{final} required for the drop to completely crystallize. For a droplet containing glycine with 100 mM NaCl, this time increases to $t_{final} = 0.40$ seconds; with 400 mM glycine, the time to achieve full crystallization is almost $t_{final} = 1.5$ minutes. There was a slight increase observed in the time required to crystallize a single droplet with the addition of silica to the glycine solution. The glycine solutions with dilute amounts of silica required $t_{final} = 0.13$

seconds, and the droplet with glycine and 0.2% silica crystallized in $t_{final} = 0.18$ seconds. It should be noted that while the total crystal growth time t_{final} is defined as the time when the surface of the growing crystal is observed to completely contact the droplet interface, spherulite growth can appear to continue as evidenced by a continued increase in pixel intensity within the droplet. This is due to the fact that crystal growth occurs in three dimensions, and the accuracy in the total time t_{final} therefore limited by both the frame rate and image resolution.

	$R_{droplet}$ (μm)	t_{final} (s)
Pure – 1.0 M	52.2	0.11
1.0 M + 100 mM NaCl	55.5	0.40
1.0 M + 400 mM NaCl	54.5	84
1.0 M + 0.0002% (v/v) silica	56.5	0.13
1.0 M + 0.2% (v/v) silica	58.0	0.18

Table 7.5. Radius of the droplet immediately prior to crystallization and the total time required for the entire drop to be crystallized at 10% relative humidity.

Fig. 7.5e shows that once the solid phase has grown and engulfed the droplet, the solid phase rearranges and forms a polycrystal with more distinct structures compared to the initial dark, uniform mass. The final appearance of the crystal exhibits one of the four textures shown in Fig. 7.7. In Fig. 7.7a, the crystal exhibits sharp facets and large continuous sections. Figs. 7.7b-c show spherulites that retain a more spherical shape, with smoother facets and smaller individual sections. In Fig. 7.7d, the crystal does not appear to significantly change and maintains the uniformly dark appearance of the initial spherical crystal. A closer look at the crystal shows that the surface looks similar to Fig. 7.7c, but the individual bumps are smaller, giving the overall appearance of a finer grain crystal surface.

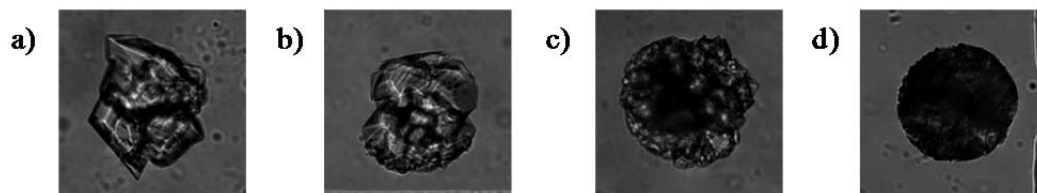


Figure 7.7. Images of typical glycine crystals obtained in a microfluidic device. Note that in these experiments, spherical crystallization of glycine is first observed, and then the crystals age to yield crystals with the appearance of one of the four textures.

The microfluidic platform generates a large number of glycine crystals formed from solution in an array, and the final morphology of the crystals can be quantified using the representative crystals defined in Fig. 7.7. Table 7.6 lists the fraction of each type of crystal obtained within a single array of crystals for different crystallization conditions. All experiments are carried out with droplets containing 1.0 M glycine initially. A pure 1.0 M glycine solution that is dehydrated at 5% relative humidity forms a mix of crystals that have larger individual grains with both sharp (Fig. 7.7a) and smooth (Figs. 7.7b and 7.7c) facets. An increase in the relative humidity to 50% increases the probability of obtaining a crystal with smooth facets, with the fraction of crystals of this type increasing from 40% to 86% of the total. The addition of salt for both initial concentrations studied here yields only crystals that have a fine grain texture (Fig. 7.7d). The presence of silica at both the concentrations considered produced crystals only with large, smooth individual grains.

Type (Fig. 7.10)	5% RH	50% RH	100 mM NaCl	400 mM NaCl	0.0002% silica	0.2% silica
<i>a</i>	0.52	0.04	-	-	-	-
<i>b or c</i>	0.40	0.86	-	-	1	1
<i>d</i>	0.08	-	1	1	-	-

Table 7.6. Fraction of crystals out of 50 crystals sampled that had a particular type of morphology shown in Fig. 7.7. All experiments are performed with an initial glycine concentration $C_i = 1.0$ M. Relative humidity is 5%, unless otherwise stated.

A visual shift in morphology of a crystal can indicate that there is a change in the molecular structure of the crystal, which can be probed using various spectroscopic techniques. Fig. 7.8 shows representative Raman spectra from the glycine crystals harvested from the microfluidic platform, plotted as intensity versus wavenumber. There are six curves shown in Fig. 7.8, each of which corresponds to a single crystal obtained from each of the conditions probed. The peaks in intensity at a given wavenumber are associated with the specific type of molecular bond present within the crystal structure. The exact intensity values are a result of the level of focus on the crystal surface and are not important in the basic crystal structure analysis carried out here. For the crystals formed from 1.0 M glycine dehydrated at 5% relative humidity (thick black line in Fig. 7.8), the spectrum shows peaks located at 74, 85, 110, 164, 179, 358, and 491 cm^{-1} . All of these peaks are also present in the remaining five spectra, and no additional peaks are observed.

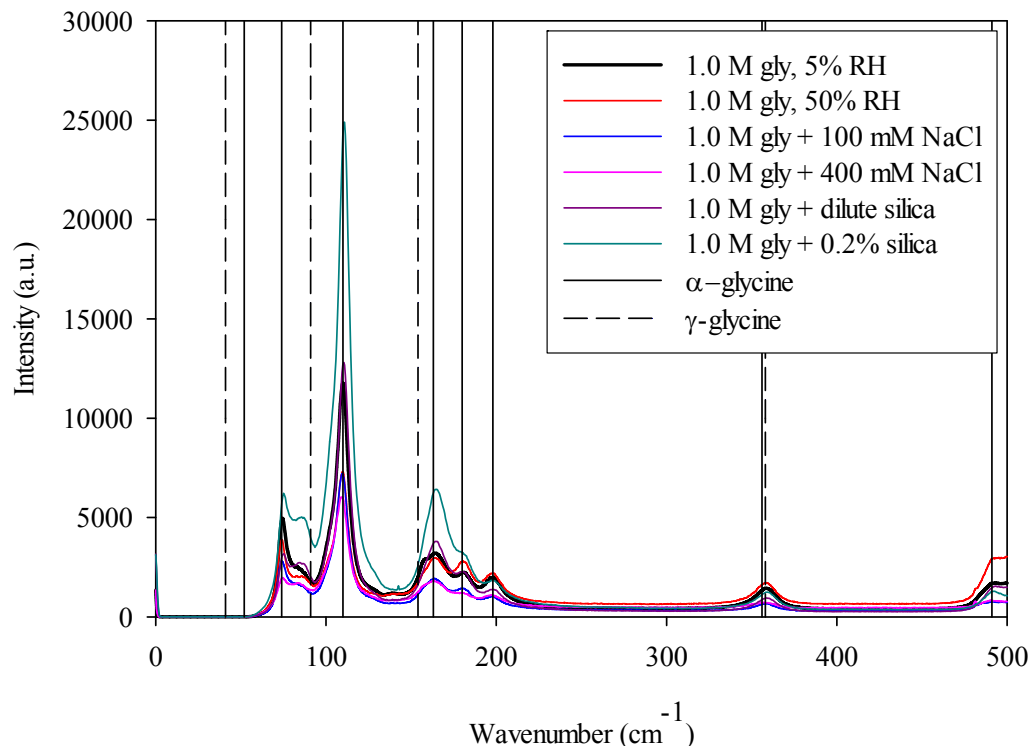


Figure 7.8. Raman spectra of glycine crystals generated from the following conditions and formulations: 1.0 M glycine dehydrated at 5% and 50% relative humidity; 1.0 M glycine with 100 mM NaCl and 400 mM NaCl; and glycine with dilute amounts of silica and 0.2% silica particles. All experiments are carried out at 5% relative humidity unless otherwise stated. The expected location of the peaks for α -glycine (solid lines) and γ -glycine (dashed lines) are also included for comparison. Note that at least 10 crystals were scanned, but these are representative spectra from individual crystals.

The expected locations of the peaks listed in Table 7.1 for α -glycine (solid lines) and γ -glycine (dashed lines) are marked on Fig. 7.11 for comparison, and show that all but one of the experimental Raman spectrum peaks corresponds to α -glycine. The peak at 85 cm^{-1} is not listed in the reference given for the values listed in Table 7.1, but has been observed in other Raman spectroscopy studies to correspond to α -glycine.³⁶ No peaks are present at the three wavenumbers listed for γ -glycine in this spectrum, nor are there any differences in the peak positions between the spectra obtained from the 10 crystals scanned in this array. This indicates that α -glycine is the most prevalent polymorph obtained for glycine

crystals formed in the microfluidic platform at 5% relative humidity. The peak positions do not change with an increase in humidity; the addition of salt; or the addition of silica, so the modifications to the crystallization process used here do not appear to affect the polymorph of glycine.

The molecular structure of a compound can also be probed using x-ray diffraction on a larger sample containing 100-250 crystals. Fig. 7.9 shows a plot of the intensity of the glycine crystals versus the angle between the incident x-ray and the detector. Samples from two humidities (5% and 50%) and two initial concentrations of NaCl (100 mM and 400 mM) are scanned, each sample containing approximately 100 crystals. There is some noise in the spectra due to the size of the crystals (~100 μm in diameter) and the size of the sample itself. The detector slit is widened to increase the detected signal from the small sample, and introduces the large bump observed at low angles. For a sample of glycine crystals formed from 1.0 M glycine in 5% relative humidity (thick black line in Fig. 7.9), the major peak is located at 29.9° ; several minor peaks at 19.0 , 20.1 , 23.9 , and 36.6° are also observed. The spectrum associated with 1.0 M glycine dehydrated at 50% humidity shows the same peaks. Very few peaks are observed in the cases where the crystals are obtained from droplets initially containing 1.0 M glycine and 100 mM NaCl or 400 mM NaCl. There is an additional peak in crystals formed with the higher concentrations of salt at 31.6° .

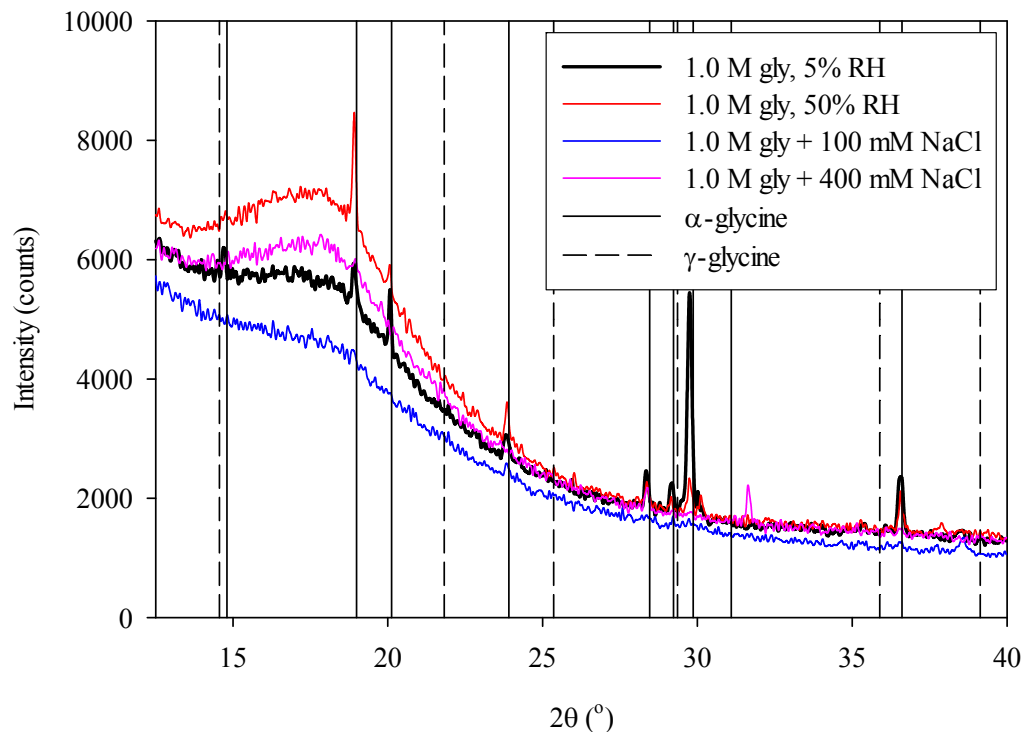


Figure 7.9. XRD spectra of 1.0 M glycine dehydrated at 5% and 50% relative humidity; 1.0 M glycine with 100 mM NaCl and 400 mM NaCl. ~100 crystals are loaded onto the sample holder for these scans. Unless otherwise noted, experiments are carried out at 5% relative humidity.

The locations of the expected peaks for glycine listed in Table 7.2 are shown on Fig. 7.9 for comparison. The prevalent peaks in Fig. 7.9 for the 1.0 M glycine spectrum all correspond to the angles associated with the α polymorph listed in Table 7.2; none of the peaks indicative of the γ polymorph are observed. It is possible to estimate the ratio of polymorphs present in a sample from the intensity values of the major peaks in an XRD spectrum. However, the spectrum for crystals formed from a 1.0 M glycine solution does not appear to include any peaks except the ones corresponding to α -glycine, so the crystals formed in the microfluidic platform generate only α -glycine crystals. A comparison of the spectra of the crystals collected after dehydrating the glycine solutions at 5% and

50% relative humidity shows no distinct changes and indicates that the increase in humidity does not affect the polymorph of the crystals obtained. The XRD scan on the crystals formed with an initial concentration of 400 mM NaCl reveals a peak that is not observed in the pure glycine case at 31.6° , and does not correspond to any of the known peaks for glycine. All other peaks are the same as the pure glycine crystals, so the change in humidity and the presence of salt do not appear to affect the polymorph of the crystals.

7.4. Discussion

Nucleation statistics, crystal growth, visual appearance, and spectroscopic characterization together provide a comprehensive characterization of the glycine crystallization process. For these experiments, the base case is an array of droplets containing a 1.0 M solution of glycine dehydrated at 5-10% relative humidity. The effect of parameters such as environmental conditions, initial concentration, and the presence of additives are captured in changes compared with the base glycine case.

The microfluidic platform generates an array of droplets where the number of droplets can be tuned to provide large sample sizes for statistics pertaining to nucleation rates. Sample sizes averaging ~ 75 drops are used here to demonstrate this platform can be used to study crystal nucleation, but it should be noted that these types of studies typically occur at constant droplet volume and solute concentration. By contrast, the experiments conducted in the present study involve a continuous variation of the concentration with time, forcing

crystallization to occur as the droplet dehydrates to a highly concentrated state. If the nucleation statistics follow classic nucleation theory for a droplet at constant volume and concentration, then the probability P that crystallization has not occurred is expected to exhibit a single exponential decay with time constant JV . However, the data shown in Fig.7.3 cannot be fit with a simple one-parameter exponential fit. Instead, the probability that a droplet has not crystallized decreases dramatically as a function of time, exhibiting a rate of decay that continuously increases as a function of time. This observation can be attributed in part to the changing volume and concentration as functions of time.

Examining Eqs. (7.1) and (7.2) reveals that the decay rate is given by $K = J(t)V(t)$. In the experiments involving dehydrating droplets, the volume of the droplet is a function of time, as well as the concentration C and the supersaturation ratio S appearing in the classic nucleation rate $J(t)$ in Eq. (7.2). In the decay rate JV , the product CV appears. For the droplet dehydration experiments considered here, concentration is inversely proportional to volume and the product CV is a constant equal to the initial mass of glycine inside the droplet. The time-varying supersaturation ratio appears in the natural log term of Eq. (7.2), and therefore the decay rate K must vary with time in a highly nonlinear way during the course of a dehydration experiment. Eqs. (7.1) and (7.2) show that as S increases during the dehydration experiment, the value of J increases leading to a steadily increasing decay rate K , consistent with experiments. Furthermore, increasing the initial glycine concentration for a fixed initial droplet volume and constant final glycine concentration leads to a larger droplet volume prior to

crystallization and a smaller overall rate of nucleation. This is consistent with the observations of Fig. 7.3 and Table 7.3 in which the time to achieve a fully crystallized array is longer for the higher initial glycine concentrations. These qualitative considerations suggest that the time varying rates of nucleation observed in the microfluidic droplet arrays are completely consistent with the time varying concentrations occurring within the droplets, and that the rate of nucleation in this type of experiment is at least partially controlled by the mass transfer problem controlling droplet dehydration. While modeling nucleation statistics is not the focus of the present study, it is clear that the detailed observations of the mass transport and the nucleation statistics in the microfluidic droplet platforms will allow for more accurate model development and validation.

The effect of the presence of salt and salt concentration on glycine crystallization is studied, and it is clear that the concentration of salt added to the dehydrating glycine solutions significantly impacts both the probability of nucleation and the subsequent growth rate of the crystal without affecting the final concentration of glycine prior to crystallization (Table 7.3). These measurements agree with previously published results indicating that an increase in the salt concentration leads to a decrease in the nucleation rate of glycine, and at high molar ratios of NaCl to glycine (> 0.45), crystallization can be suppressed.^{27,39-41} This behavior cannot be explained by simply considering the time varying concentration during dehydration, and indicates that the salt is interacting with the glycine in a way that is not taken into account by simple nucleation models.

The decreases in nucleation and growth rates, however, do not have an effect on the polymorph, and it appears that α -glycine is the only polymorph obtained using the microfluidic platform. This observation is in contrast with the numerous studies that show that the presence of NaCl promotes the growth of γ -glycine over α -glycine, leading to an increase in the formation of γ -glycine. The polymorph preference is attributed to the salt ions inhibiting the growth of the specific crystal faces associated with α -glycine, which would otherwise be the faster growing polymorph. This theoretically allows the crystal faces associated with γ -glycine to grow instead, which proceeds at a slower rate.^{27,39,40} A direct measure of the crystal growth rate along with a spectroscopic scan for the polymorph could be used to correlate changes in growth rate with polymorph change. Combined studies like these have not been carried out previously.

The lack of observed γ -glycine in these experiments may be a result of the aging of the crystal immediately after formation of the spherulite. In addition, the protocol used to harvest the crystals for off-chip spectroscopic characterization may also impact the crystal polymorph and may induce changes. These possibilities should be examined in greater detail for future studies. Nevertheless, these observations taken together demonstrate that the microfluidic platform is a useful tool for gaining insight into the crystal nucleation and growth mechanisms that are affected by the presence of additives and other crystallization conditions.

The addition of silica to the glycine solutions nominally introduces controlled nucleation sites into the dehydrating droplets. Table 7.3 shows that addition of silica decreases the final concentration of glycine just prior to

crystallization and results in a larger final droplet volume. The calculated average nucleation time and overall growth times are slightly longer than the base case of pure glycine. The increased nucleation and growth times are consistent with the decrease in final glycine concentration before crystallization. A decrease in supersaturation increases the energy barrier that must be overcome in order for crystallization to occur, which decreases the nucleation rate (Eq. (7.2)).

A solid surface also affects the nucleation of crystals, and more recent studies have shown that tuning the functionality of a solid surface can be used to control the crystal polymorph. Badruddoz *et al.* report that functionalized silica nanoparticles can be used to tune the glycine polymorph and that the addition of bare silica nanoparticles ($2a = 250$ nm) or those with amino and carboxyl surface groups leads to an increase in the β -polymorph of glycine. The Raman spectra plotted in Fig. 7.11 for the droplets containing glycine with silica nanoparticles do not show a polymorph change. The Raman spectrum for β -glycine looks very similar to α -glycine, but does not include the peaks prior to 110 cm^{-1} or after 160 cm^{-1} and includes an additional peak at $\sim 150\text{ cm}^{-1}$.³⁶ The lack of a polymorph change could be due to the type of silica nanoparticles used in the experiments carried out in the microfluidic platform. Ludox TM has a diameter $2a = 22$ nm and is purchased from the manufacturer as an aqueous suspension stabilized with sodium sulfate. The sodium sulfate may act similar to sodium chloride as an additive and induce crystallization of α -glycine. A polymorph transformation may also result from post-processing the crystals for off-chip characterization.

7.5.Conclusions

The microfluidic platform presented can efficiently examine the details of several aspects of crystallization with a relatively small sample volume. Many high-throughput crystallization methods focus on polymorph screening, whereas the potential of the present microfluidic platform lies in its ability to provide directly measurements of nucleation statistics and crystal growth rates as a function of crystallization conditions. Glycine is used to demonstrate proof of concept that the microfluidic platform yields statistically relevant information on the mechanisms that govern crystallization as function of concentration changes, additives, and impurities on crystallization from aqueous solutions. The crystals are collected off-chip for further characterization using Raman spectroscopy and x-ray diffraction, which show that the dominant polymorph of glycine is unaffected by the addition of various impurities.

7.6. References

1. Nagy, Z. K.; Braatz, R. D. Advances and New Directions in Crystallization Control. *Annual Review of Chemical and Biomolecular Engineering*. **2012**, *3*, 55-75.
2. Leng, J.; Salmon, J.-B. Microfluidic crystallization. *Lab on a Chip*. **2009**, *9*, 24-34.
3. van der Woerd, M.; Ferree, D.; Pusey, M. The promise of macromolecular crystallization in microfluidic chips. *Journal of Structural Biology*. **2003**, *142*, 180-187.
4. Davey, R. J.; Allen, K.; Blagden, N.; Cross, W. I.; Lieberman, H. F.; Quayle, M. J.; Righini, S.; Seton, L.; Tiddy, G. J. T. Crystal engineering - nucleation, the key step. *CrystEngComm*. **2002**, *4*, 257-264.
5. Smith, W. F.; Hashemi, J. *Foundations of Materials Science and Engineering*, McGraw-Hill, 2003,
6. Iitaka, Y. The crystal structure of γ -glycine. *Acta Crystallographica*. **1961**, *14*, 1-10.
7. Rhodes, G. *Crystallography Made Crystal Clear: A Guide for Users of Macromolecular Models*, Elsevier Science, 2010,
8. Cudney, R.; Patel, S.; Weisgraber, K.; Newhouse, Y.; McPherson, A. Screening and optimization strategies for macromolecular crystal growth. *Acta Crystallographica Section D: Biological Crystallography*. **1994**, *50*, 414-423.
9. McRee, D. E. *Practical Protein Crystallography*, 2nd, Academic Press, 1999, 477.
10. Vuong, S. M.; Anna, S. L. Tuning bubbly structures in microchannels. *Biomicrofluidics*. **2012**, *6*, 022004.
11. Gong, T.; Shen, J.; Hu, Z.; Marquez, M.; Cheng, Z. Nucleation Rate Measurement of Colloidal Crystallization Using Microfluidic Emulsion Droplets. *Langmuir*. **2007**, *23*, 2919-2923.
12. Moschou, P.; de Croon, M. H.; van der Schaaf, J.; Schouten, J. C. Advances in continuous crystallization: toward microfluidic systems. *Reviews in Chemical Engineering*. **2012**,
13. Li, L.; Ismagilov, R. F. Protein Crystallization Using Microfluidic Technologies Based on Valves, Droplets, and SlipChip. *Annual Review of Biophysics*. **2010**, *39*, 139-158.
14. Yamaguchi, H.; Maeki, M.; Yamashita, K.; Nakamura, H.; Miyazaki, M.; Maeda, H. Controlling one protein crystal growth by droplet-based microfluidic system. *Journal of Biochemistry*. **2013**,
15. Kang, L.; Chung, B. G.; Langer, R.; Khademhosseini, A. Microfluidics for drug discovery and development: From target selection to product lifecycle management. *Drug Discovery Today*. **2008**, *13*, 1-13.

16. Thorson, M. R.; Goyal, S.; Gong, Y.; Zhang, G. G. Z.; Kenis, P. J. A. Microfluidic approach to polymorph screening through antisolvent crystallization. *CrystEngComm*. **2012**, *14*, 2404-2412.
17. Laval, P.; Salmon, J.-B.; Joanicot, M. A microfluidic device for investigating crystal nucleation kinetics. *Journal of Crystal Growth*. **2007**, *303*, 622-628.
18. Laval, P.; Giroux, C. I.; Leng, J.; Salmon, J.-B. Microfluidic screening of potassium nitrate polymorphism. *Journal of Crystal Growth*. **2008**, *310*, 3121-3124.
19. Laval, P.; Crombez, A.; Salmon, J.-B. Microfluidic Droplet Method for Nucleation Kinetics Measurements. *Langmuir*. **2009**, *25*, 1836-1841.
20. Li, L.; Fu, Q.; Kors, C.; Stewart, L.; Nollert, P.; Laible, P.; Ismagilov, R. A plug-based microfluidic system for dispensing lipidic cubic phase (LCP) material validated by crystallizing membrane proteins in lipidic mesophases. *Microfluidics and Nanofluidics*. **2010**, *8*, 789-798 LA - English.
21. Shim, J.-u.; Cristobal, G.; Link, D. R.; Thorsen, T.; Fraden, S. Using Microfluidics to Decouple Nucleation and Growth of Protein Crystals. *Crystal Growth & Design*. **2007**, *7*, 2192-2194.
22. Toldy, A. I.; Badruddoza, A. Z. M.; Zheng, L.; Hatton, T. A.; Gunawan, R.; Rajagopalan, R.; Khan, S. A. Spherical Crystallization of Glycine from Monodisperse Microfluidic Emulsions. *Crystal Growth & Design*. **2012**, *12*, 3977-3982.
23. Iitaka, Y. The crystal structure of β -glycine. *Acta Crystallographica*. **1960**, *13*, 35-45.
24. Drebushchak, V. A.; Boldyreva, E. V.; Drebushchak, T. N.; Shutova, E. S. Synthesis and calorimetric investigation of unstable β -glycine. *Journal of Crystal Growth*. **2002**, *241*, 266-268.
25. Torbeev, V. Y.; Shavit, E.; Weissbuch, I.; Leiserowitz, L.; Lahav, M. Control of Crystal Polymorphism by Tuning the Structure of Auxiliary Molecules as Nucleation Inhibitors. The β -Polymorph of Glycine Grown in Aqueous Solutions. *Crystal Growth & Design*. **2005**, *5*, 2190-2196.
26. Weissbuch, I.; Torbeev, V. Y.; Leiserowitz, L.; Lahav, M. Solvent Effect on Crystal Polymorphism: Why Addition of Methanol or Ethanol to Aqueous Solutions Induces the Precipitation of the Least Stable β Form of Glycine. *Angewandte Chemie International Edition*. **2005**, *44*, 3226-3229.
27. Yang, X.; Lu, J.; Wang, X.-J.; Ching, C.-B. Effect of sodium chloride on the nucleation and polymorphic transformation of glycine. *Journal of Crystal Growth*. **2008**, *310*, 604-611.
28. Han, G.; Thirunahari, S.; Shan Chow, P.; Tan, R. B. H. Resolving the longstanding riddle of pH-dependent outcome of glycine polymorphic nucleation. *CrystEngComm*. **2013**, *15*, 1218-1224.
29. Han, G.; Chow, P. S.; Tan, R. B. H. Direct Comparison of α - and γ -Glycine Growth Rates in Acidic and Basic Solutions: New Insights into Glycine Polymorphism. *Crystal Growth & Design*. **2012**, *12*, 2213-2220.

30. Towler, C. S.; Davey, R. J.; Lancaster, R. W.; Price, C. J. Impact of Molecular Speciation on Crystal Nucleation in Polymorphic Systems: The Conundrum of γ Glycine and Molecular 'Self Poisoning'. *Journal of the American Chemical Society*. **2004**, *126*, 13347-13353.
31. Teychene, S.; Sicre, N.; Biscans, B. Is spherical crystallization without additives possible? *Chemical Engineering Research and Design*. **2010**, *88*, 1631-1638.
32. Shtukenberg, A. G.; Punin, Y. O.; Gunn, E.; Kahr, B. Spherulites. *Chemical reviews*. **2011**, *112*, 1805-1838.
33. Kovacic, B.; Vrečer, F.; Planinsek, O. Spherical crystallization of drugs. *Acta pharmaceutica*. **2012**, *62*, 1-14.
34. Badruddoza, A. Z. M.; Toldy, A. I.; Hatton, T. A.; Khan, S. A. Functionalized Silica Nanoparticles as Additives for Polymorphic Control in Emulsion-Based Crystallization of Glycine. *Crystal Growth & Design*. **2013**, *13*, 2455-2461.
35. Shi, Y.; Wang, L. Collective vibrational spectra of α - and γ -glycine studied by terahertz and Raman spectroscopy. *Journal of Physics D: Applied Physics*. **2005**, *38*, 3741.
36. Surovtsev, N. V.; Adichtchev, S. V.; Malinovsky, V. K.; Ogienko, A. G.; Drebuschak, V. A.; Manakov, A. Y.; Ancharov, A. I.; Yunoshev, A. S.; Boldyreva, E. V. Glycine phases formed from frozen aqueous solutions: Revisited. *The Journal of Chemical Physics*. **2012**, *137*, -.
37. Iitaka, Y. The crystal structure of γ -glycine. *Acta Crystallographica*. **1958**, *11*, 225-226.
38. Goh, L.; Chen, K.; Bhamidi, V.; He, G.; Kee, N. C. S.; Kenis, P. J. A.; Zukoski, C. F.; Braatz, R. D. A Stochastic Model for Nucleation Kinetics Determination in Droplet-Based Microfluidic Systems. *Crystal Growth & Design*. **2010**, *10*, 2515-2521.
39. Akers, M. J.; Milton, N.; Byrn, S. R.; Nail, S. L. Glycine Crystallization During Freezing: The Effects of Salt Form, pH, and Ionic Strength. *Pharmaceutical Research*. **1995**, *12*, 1457-1461.
40. Hrkovac, M.; Prlic Kardum, J.; Schuster, A.; Ulrich, J. Influence of Additives on Glycine Crystal Characteristics. *Chem. Eng. Technol*. **2011**, *34*, 611-618.
41. Duff, N.; Dahal, Y. R.; Schmit, J. D.; Peters, B. Salting out the polar polymorph: Analysis by alchemical solvent transformation. *The Journal of Chemical Physics*. **2014**, *140*, 014501.

Chapter 8. Conclusions and Future Work

Small sample volumes and low fabrication costs characteristic of the field of microfluidics offer distinct advantages for applications in screening and analysis. The development of microfluidic techniques can be focused on fundamental components such as droplet formation, mixing, trapping, and storage, or it can be motivated by a specific application. The design of a microfluidic platform that addresses the needs of an given application requires additional understanding and tuning beyond what has been characterized for the basic components. The work presented in this thesis addresses both the individual components regarding droplet formation, storage, and dehydration (Chapters 4 and 5), as well as the specific applications that build upon adaptations of the basic platform to study two phase transitions (Chapters 6 and 7).

Monodisperse bubble and droplet formation has been extensively studied and characterized as function of gas pressure and flow rate, which has led to the development of an extensive knowledge base that can be used to control droplet formation. However, many of the controlling parameters in bubble and droplet formation are specific to a given nozzle type, channel geometry, and pair of phases. In Chapter 4, we describe a geometric model that can be used to predict the bubble shape and foam structure given the bubble volume, volume fraction of the dispersed phase, and the depth and width of a straight microchannel with a rectangular cross-section. Three shapes (sphere, pancake, slug) and five structures (dripping, slug, alternating foam, packed foam, and bamboo foam) are defined, and the critical volume and volume fractions at which the bubble and foam

structure transition to each shape and structure are described. These critical values are used to generate an operating diagram for a given set of channel dimensions. In addition, the model does not take into account fluid properties, and so droplet generation is also compared to the predicted operating regimes. Bubbles and droplets are generated using three microfluidic nozzles (T-junction, co-flow, and flow-focusing), and their downstream shape and structure are compared to the operating diagram. It is found that the geometric model agrees with what is observed experimentally for both bubbles and droplets, and provides a set of criteria that can be used to design and generate a desired foam or emulsion.

In this work, emulsions are used to probe particle suspension stability (Chapter 6) and crystal nucleation and growth (Chapter 7) by considering each droplet as an individual microreactor. For these applications, a large droplet spacing in the emulsion is desired to prevent droplet interactions, along with a method to store the emulsion for the tens of hours required for particle aggregation or crystallization to occur. Chapter 5 describes a microfluidic design that can be used to achieve and store the desired emulsion. The design is based on a trap design described previously by Bithi *et al.* and Boukellal *et al.* that is patterned in a square array to yield a desired droplet spacing, and is used to simultaneously form and store the droplets for extended observation.

Chapter 5 also focuses on the empirical control of dehydration through the microfluidic device material polydimethylsiloxane (PDMS). The dehydration of an array of droplets containing either water or salt solutions is carried out in the microfluidic devices stored in relative humidities varying from 5-75% at 20°C.

The total time to fully dehydrate the drops increases with relative humidity and ranges from ~10 to 40 hours. At high relative humidities ($> 50\%$), the crystallization of salt is suppressed, and the droplets achieve a constant droplet volume and concentration. Droplet dehydration is shown to be reasonably modeled by spherical diffusion and the droplet radius scales with time as $r \sim t^{1/2}$.

In most experimental microfluidic studies, the exact droplet shape is unknown and approximations are made to obtain an estimate on the droplet volume. Chapter 5 describes a method to indirectly measure the accuracy of the model droplet shape equations described in Chapter 4 used to calculate the droplet volume as the droplet dehydrates. The method uses the fact that the refractive index of a solution will increase as the droplet volume decreases and the solute concentration increases. The refractive index of the solution eventually equals the refractive index of the continuous phase oil at a volume controlled by the initial droplet volume and solute concentration. Sucrose solutions are used for this study, and the results show that the droplet volumes can be accurately predicted within error using the model droplet shape equations presented in Chapter 4.

The dehydration-based microfluidic platform is used to develop a tool that is capable of probing particle suspension stability. In Chapter 6, the effect of salt concentration on the stability of silica suspensions is studied. It is noted that the path length of the droplet is too short to observe changes in turbidity, and so the stability is monitored by changes in the fluid properties by tracking the particle motion of fluorescent tracer particles. The aggregation behavior is also measured on the bulk scale with a rheometer. The experiments performed in the

microfluidic platform show that as the salt concentration increases, the flocculation rate increases, and time to flocculation decreases. These results agree with both the flocculation times obtained from the bulk rheology experiments and with the trends reported in the literature. As a result, the microfluidic platform can be used to assess the stability of particle suspensions as a function time.

The full dehydration of droplets containing silica suspensions and clay suspensions are also carried out and described in Chapter 6. Dehydration experiments show that the rate at which the droplet shrinks depends on relative humidity, but the final concentration is independent of dehydration rate. The final concentration of silica suspensions is approximately $\phi \approx 0.6$, which agrees with the literature. Droplets containing clay suspensions are observed to exhibit a final particle concentration that is significantly higher than previously reported. The droplets appear to be homogenous after they have achieved a constant volume and do not show evidence of the cracks observed in bulk drying studies. These experiments show that homogeneous concentrated particle suspensions may be achieved by dehydration in the microfluidic platform.

The same microfluidic platform is used in a second application to study the nucleation and growth of crystals. Many crystallization studies focus on polymorph screening, and characterization experiments are carried out to determine the conditions required to empirically control crystallization. Fewer studies focus on the nucleation rate and growth of the crystal, which are difficult to measure in depth. Glycine crystallization is carried out in the microfluidic platform, and nucleation statistics and crystal growth rates are obtained using

conditions consistent with previous studies. The nucleation statistics obtained from the glycine experiments are consistent with classic nucleation theory, taking into account that the concentration within the droplets varies with time. Crystal growth rates are observed to follow the relationship $r \sim t$ at intermediate times, and approaches the diffusion-limited regime, exhibiting the relationship $r \sim t^{1/2}$ at late times. Crystals from each formulation are collected off-chip for characterization by Raman spectroscopy and x-ray diffraction, which show that only the α polymorph of glycine is achieved in these experiments, regardless of initial concentration, humidity, and the presence of additives. These studies demonstrate that the microfluidic platform can examine crystallization with a relatively small sample volume and provide direct measurements of the nucleation statistics and growth rates.

Future Work

The microfluidic platform presented here is used to study two model aqueous systems that undergo a phase transition as a function of time and concentration. The PDMS used to fabricate the microfluidic devices has a significant role in the droplet dehydration that is used to achieve these phase transitions, but it also presents a challenge in terms of system compatibility. Surface active molecules will adsorb on the PDMS surface and can cause the surfactant carrier phase to preferentially wet the naturally hydrophobic surface. This can become an issue when there is a surfactant present in the intended dispersed phase and can lead to failure of controlled, multiphase flow. A

surfactant can be added to the continuous phase to mitigate this, but as described in Chapter 6, this can lead to unexpected interactions between various contents dispersed within both phases and complications with droplet formation. Future studies would benefit from the development of a microfluidic platform fabricated from another material that is not PDMS and is compatible with variations in the continuous and dispersed phases. Materials such as glass, polymethylmethacrylate, polystyrene, and optical adhesives have been used successfully to fabricate device materials. Depending on the permeability of the new material, other parameters can be varied to drive dehydration and may include the use of multi-layer devices and changes in the continuous phase.

The tool developed to monitor suspensions stability can be improved to increase the range of fluid properties that can be probed within the device. As described in Chapter 6, the limiting factors in the protocol used are the size of the fluorescent tracer particles and the objective magnification. These are straightforward modifications to the microfluidic platform; the use of smaller tracer particles (1 μm) is not projected to affect droplet formation or extended storage, while a higher objective magnification would not lead to the loss of information, since single droplets are individually imaged for these studies. The future applications of the platform include the use of the platform to predict the shelf-life of products containing suspensions, and the further development of the platform to accommodate solutions containing organic suspensions. It is reported in Chapter 6 that the droplets are stored for at least two weeks without a significant change in the droplet volume, and storage for up to a month is tested.

The next step is to determine the potential limiting factors associated with extended storage in the microfluidic device and the impacts they would have regarding ability to probe the stability of suspensions stored for months or years. In the second direction, the platform would be adapted to study the stability of suspensions regardless of the solvent. This could also require the initial development of a non-PDMS device, but would expand the applicability of the platform as a viable analytical tool.

Crystallization studies carried out within the platform would also benefit from a device material that is less favorable for material adsorption. Protein crystallization is a common application of the analysis tools developed with microfluidic techniques; however, proteins may act as surfactants and can adsorb to PDMS, which can affect the crystallization of the protein. A modification to the microfluidic device material may also be beneficial for on-chip characterization of the resulting crystals. In Chapter 7, the PDMS signature is described to dominate the Raman spectra in preliminary attempts to carry out on-chip crystal characterization. This resulted in an additional processing step to remove the crystals and may have affected the final crystal polymorph. On-chip characterization would therefore eliminate this possibility and would provide a tool to directly study the nucleation and growth of crystals that result from modifications made to a given crystallization method.